

Magnetic States and Excitations of Complex Spin Systems

Sachith Erandaka Dissanayake
Colombo, Sri Lanka

B.Sc., University of Colombo, Sri Lanka, 2008

A Dissertation presented to the Graduate Faculty of the University
of Virginia in Candidacy for the Degree of Doctor of Philosophy

Department of Physics

University of Virginia

May, 2015

“Look deep into nature, and then you will understand everything better.”

Albert Einstein

Abstract

Doctor of Philosophy

Magnetic States and Excitations of Complex Spin Systems

by Sachith Erandaka Dissanayake

The interplay between spin, lattice, charge and orbital degree of freedom has been extensively studied in various transition-metal oxides. Upon cooling, in a typical magnetic system, long-range order appears below the Curie-Weiss temperature. However, the long-range order of spins, either fully or partially, can be suppressed due to the effects like the geometrical arrangement of spins, substitution of different ions, and low dimensionality. The correlation between different degrees of freedom sometimes drives the system to novel phases through a phase transition.

Neutron scattering is a very powerful technique to study the magnetic properties of such materials and the interplay between the different degrees of freedom. In this work, intriguing phases of two vanadates with exotic complex spin systems are studied by using elastic and inelastic neutron scattering techniques.

When the orbital degree of freedom is degenerate, the Jahn-Teller distortion can occur inducing a phase transition into an orbitally ordered state. The two vanadates which are the subjects of this study, $\text{BaV}_{10}\text{O}_{15}$ and CoV_2O_4 , both contain V^{3+} (t_{2g}^2) ions which are Jahn-Teller active.

$\text{BaV}_{10}\text{O}_{15}$ for instance is a highly frustrated magnet that shows fascinating physics with possible mixed valance ions with a $\text{V}^{3+}:\text{V}^{2+}$ ratio of 4:1. Although it is a frustrated complex spin system with 80 magnetic ions in the unit cell, prior studies suggest a trimer formation by 60% of V ions that is accompanied by a structural phase transition at 123 K and followed by long range order below 43 K. However, the magnetic ground state of the low temperature phase is unknown. To understand the nature of the magnetic ground state and the interplay between lattice, spin, charge and orbital degrees of freedom, we performed elastic and inelastic neutron scattering measurements on single crystal and polycrystalline samples of $\text{BaV}_{10}\text{O}_{15}$. The neutron scattering data show that the best model to explain the data is when the low temperature long range ordered phase contains only two ordered V ions (V1 and V2) which form pseudo-squares connected in the bc plane while the other three ions remain disordered in a spin singlet state, which agrees

with the previously reported trimer formation. We determined the Hamiltonian that can describe the magnetic excitation observed in this system and discussed the possible orbital ordering that can lead to this magnetic ground state. Evidence for singlet to triplet excitations from the trimer is also presented as higher energy excitations around 33 meV. The important results presented here for this system is a prime example how a complex spin system achieve a simple magnetic state through orbital ordering by relieving spin frustration.

The other vanadate system, spinel CoV_2O_4 , with V^{3+} ions located at vertices of a network of corner-sharing tetrahedra, also provides a good playground to investigate the effects of different degrees of freedom. Among the family of spinel vanadates, CoV_2O_4 lies near the boundary of itinerant electron limit making it difficult to probe the effects of spin, lattice and orbital degrees of freedom. Our polarized and unpolarized elastic neutron scattering measurements indicate that the Co and V ions order ferrimagnetically at 169 K and V spins start canting at $T = 90$ K. Also, the strain measurements performed by a collaboration study shows a second order type structural change in the order of 10^{-4} with a maximum distortion at ~ 100 K. These important results of combining the elastic neutron scattering and the strain data indicate that the system undergoes two phase transitions, first from paramagnetic to a collinear ferrimagnetic state and secondly to a noncollinear ferrimagnetic state and an orbital glassy state of V t_{2g} orbitals at ~ 90 K. The magnetic excitations of a single crystal CoV_2O_4 in the ordered phase is also reported and a spin Hamiltonian to describe the inelastic neutron scattering data is provided.

These neutron scattering studies on the magnetic states and the excitations of $\text{BaV}_{10}\text{O}_{15}$ and CoV_2O_4 provide important results to understand the interplay between different degrees of freedom in the two systems and similar materials.

Acknowledgements

It is with sincere pleasure I express my deeply felt gratitude to my advisor Prof. Seunghun Lee for his constant inspiration, guidance, invaluable feedback and suggestions I have received throughout my Ph.D. His encouraging words, unfailing assistance, timely advice and in-depth knowledge were vital to make this long term endeavor a success. His humbleness and the confidence he kept in me made me more than I could be and I owe him a deep debt of gratitude for being a wonderful advisor.

In addition to my advisor, I must express my deeply felt gratitude to the other members of my thesis committee, Prof. Despina Louca, Prof. Israel Klich and Prof. Avik Ghosh and my former research committee member Prof. Paul Fendley.

I owe a deep debt of gratitude to Prof. Nilanga Liyanage, who helped me start my life at University of Virginia and gave timely advice on diverse of situations throughout my Ph.D.

I would like to express my sincere gratitude to Dr. Masaaki Matsuda for all his support and collaboration in experiments performed in HFIR, ORNL, his stimulating discussions and all the encouragement, confidence and kindness he showed me in the admission process to ORNL. I must thank Dr. Jaime Fernandez-Baca for giving me the opportunity to further pursue my career in neutron scattering at ORNL.

I must express my sincere gratitude to Prof. Takuro Katsufuji of Waseda University, Japan for providing high quality samples, collaboration and stimulating discussions.

My sincere thanks go to all the instrument scientist collaborators at neutron facilities; Dr. Matthew Stone at ARCS, SNS, Dr. Yiming Qiu, Dr. Mark Green and Dr. John Copely at DCS, NIST, Dr. Qingzhen Huang at BT1, NIST, Dr. Manfred Reehuis at E5, HZB, Dr. Andreas Hoser at E6, HZB, Dr. Ovidiu Garlea at HB2A, HFIR, Dr. K. C. Rule and Dr. Bella Lake at V2, HZB. I am grateful to Dr. X. G. Zheng and Dr. M. Hagihala from Saga University, Japan for providing a sample for one of my projects. I would also like to thank Dr. Takatsugu Masuda and Dr. Minoru Soda from ISSP for the collaboration with powder neutron scattering experiments at ISIS. I must thank Dr. T. K. Ng at the Hong Kong University of Science and Technology, Dr. M.-H. Whangbo and Dr. H.-J. Koo at North Carolina State University for their collaboration and helpful discussions.

I must call my present and former fellow labmates to mind with gratitude, Anjana Samarakoon, Tianran Chen, Dr. Jooseop Lee, Dr. Kazuki Iida and Dr. Naoyuki Katayama for all the useful discussions, support, strength and all the fun we had together. My

heartfelt thanks go to Kapila Wijayaratne for all the useful discussions and support given on graphic software.

My sincere appreciation goes to Eric Magnuson who quickly and timely proofread the dissertation.

Last but not least, I would like to thank and dedicate this dissertation to my parents and family. The dreams of my parents, their love, care and pointing the right direction starting from the early childhood to now made me achieve this. I must also deeply grateful to my wife Anushika Athauda for patience, assistance, support, love and encouragement offered to me through out this endeavor. Without her this would have never been possible. I should very lovingly call my little daughter Sanuki to mind who brought love and comfort to my life and got my feet back on the ground at hard times, with just a cute smile and her favorite word "Thaththa".

Contents

Abstract	ii
Acknowledgements	iv
Contents	vi
List of Figures	viii
List of Tables	xi
Abbreviations	xii
Physical Constants	xiii
Symbols	xiv
1 Introduction	1
1.1 Introduction to frustrated magnets	1
1.2 Phase transitions and magnetic states	3
1.3 Orbital ordering	4
1.4 Exchange interactions	7
1.5 Brief introduction to the materials and methods	10
1.6 Outline of the Thesis	11
2 Introduction to Neutron Scattering	12
2.1 Theory of Neutron Scattering	12
2.1.1 Why Neutron?	12
2.1.2 Neutron scattering instruments	13
2.1.3 Scattering Diagram	17
2.2 Neutron Scattering Formula	18
2.2.1 Differential cross section	18
2.2.2 Elastic Neutron Scattering	21
2.2.2.1 Nuclear Elastic Scattering	21
2.2.2.2 Magnetic Elastic Scattering	22
2.2.2.3 Representational Analysis to find magnetic structure	23
2.2.3 Inelastic Neutron Scattering	24

2.2.3.1	Linear spinwave calculations	25
3	Orbital and magnetic states of frustrated magnet $\text{BaV}_{10}\text{O}_{15}$	32
3.1	Introduction	32
3.2	Methods	37
3.2.1	Experimental details	37
3.2.2	Calculation details	37
3.3	Bulk susceptibility and Elastic and inelastic neutron scattering data	38
3.3.1	Bulk susceptibility	38
3.3.2	Neutron diffraction and Crystal Structure	39
3.3.3	Inelastic neutron scattering data	43
3.4	Determination of magnetic states of $\text{BaV}_{10}\text{O}_{15}$	48
3.4.1	Complexity of the system	48
3.4.2	Systematic approach to find the magnetic state	50
3.4.3	Simulation of magnetic excitations : Linear spinwave calculations	60
3.4.4	Temperature dependence of higher energy magnetic excitation	65
3.5	Possible orbital ordering of $\text{BaV}_{10}\text{O}_{15}$	69
3.6	Summary and Conclusions	75
4	Orbital glass state and spin correlations of spinel CoV_2O_4	76
4.1	Introduction	76
4.1.1	Introduction to Spinel Vanadates	76
4.1.2	Crystal structure and bulk properties CoV_2O_4	78
4.1.3	Near metallic nature of CoV_2O_4	80
4.2	Methods	82
4.2.1	Experimental details	82
4.2.2	Calculation details	82
4.3	Crystal and magnetic structure	83
4.3.1	Neutron powder diffraction data	83
4.3.2	Magnetic structure refinement	87
4.4	Temperature dependence	91
4.4.1	Bulk susceptibility and Magnetorestriction data	91
4.4.2	Elastic single crystal data	96
4.4.3	Polarized neutron scattering results	100
4.4.4	Orbital glass state	102
4.5	Magnetic excitations	102
4.5.1	Inelastic neutron scattering data	102
4.5.2	Linear spinwave calculation	108
4.6	Summary and Conclusions	113
A	Linear Spin wave calculation of Kagome Antiferromagnet.	114
	Bibliography	125

List of Figures

1.1	Antiferromagnetically interacting spins in an arrangement of a (a) Square (b) Traingular (c) Tetrahedral	2
1.2	(a)Variation of magnetic susceptibility with temperature for paramagnetic, ferromagnetic and antiferromagnetic (from reference [11])(b)ZFC, FC and thermoremanent (TRM) measured on heating after cooling the Ag(Mn) spin glass to 20 K and then measuring on heating. [12]	4
1.3	(a) Shape of the different d orbitals [13] (b) Energy levels of d orbitals for different crystal fields [14]	5
1.4	(a) Shape of the different d orbitals (b) Energy levels of d orbitals for different crystal fields	7
1.5	Exchange interactions are responsible for magnetic ordering. (a) Direct exchange : between neighboring d atomic orbitals in a transition metal compound with edge sharing octahedra. (b) Superexchange : between d atomic orbitals via ligand p atomic orbitals in a transition metal compound with vertex-sharing octahedra. (From reference [18])	9
1.6	Double exchange mechanism between Mn^{3+} and Mn^{3+} ions	9
2.1	The schematic diagram of BT1 powder diffractometer	14
2.2	The schematic diagram of HB1 triple axis spectrometer	15
2.3	The schematic diagram of time of flight spectrometer DCS at NIST	16
2.4	Scattering triangle	17
2.5	Differential cross section	18
2.6	Physical picture of a spin wave.	26
2.7	Linear aniferromagnetic chain with two sublattice	29
2.8	Dispersion of spinwave mode for linear 1D aniferromagnet chain	31
3.1	Arrangement of V ions in $BaV_{10}O_{15}$	35
3.2	Figure from reference [50]. The arrangement of the V ions (circles) in $BaV_{10}O_{15}$ for $z=0$ and $z=1/4$	36
3.3	Figure and caption from reference [50]. Temperature dependence of resistivity and magnetic susceptibility for $BaV_{10}O_{15}$	36
3.4	Temperature dependence of magnetic susceptibility for $BaV_{10}O_{15}$	39
3.5	Neutron powder diffraction data of $BaV_{10}O_{15}$	41
3.6	Time of flight inelastic neutron scattering data of $BaV_{10}O_{15}$ single crystal	45
3.7	Time of flight inelastic neutron scattering data of $BaV_{10}O_{15}$ single crystal, high energy excitations	46
3.8	Time of flight inelastic neutron scattering data of $BaV_{10}O_{15}$ powder sample	47
3.9	Arrangement of V spins and different types of interactions in $BaV_{10}O_{15}$	49
3.10	Previous neutron diffraction data and refinement $BaV_{10}O_{15}$	51

3.11	Arrangement of V ions in the ab plane and edge sharing bonds BaV ₁₀ O ₁₅	52
3.12	Possible magnetic structures with only V1 and V2 ions ordered below T_N of BaV ₁₀ O ₁₅	54
3.13	Few examples of possible magnetic structures with only V2B, V3 and V3B ions ordered below T_N of BaV ₁₀ O ₁₅	55
3.14	Refinement of NPD data Possible magnetic structures with only V1 and V2 ions ordered below T_N of BaV ₁₀ O ₁₅	57
3.15	Refinement of NPD data of possible magnetic structures with only V2B, V3 and V3B ions ordered below T_N of BaV ₁₀ O ₁₅	58
3.16	Linear spinwave calculation for Model T1 as in Figure 3.13 of BaV ₁₀ O ₁₅	62
3.17	Linear spinwave calculation for Model M7 as in Figure 3.12 of BaV ₁₀ O ₁₅	63
3.18	Linear spinwave calculation for Model M8 as in Figure 3.12 of BaV ₁₀ O ₁₅	64
3.19	Temperature dependence 33 meV excitation measured using powder inelastic neutron scattering experiment of BaV ₁₀ O ₁₅ using MARI spectrometer at ISIS	68
3.20	Possible orbital configurations for V1 and V2 ions	72
3.21	Octahedral environment of V1 and V2 ions by oxygen	73
3.22	Corner sharing bonding of 120 ° in the octahedral environment of V1 and V2 ions by oxygen	74
4.1	Crystal structure of spinel AB ₂ O ₄	77
4.2	Co and V sites of CoV ₂ O ₄	79
4.3	X-ray Diffraction pattern for CoV ₂ O ₄ at room temperature	79
4.4	The temperature dependence of the magnetization, thermal conductivity, magnetic entropy change, and heat capacity for CoV ₂ O ₄	80
4.5	Activation energy, E and c/a ratio of AV ₂ O ₄ spinels as a function of V-V distance	81
4.6	Neutron powder diffraction data of CoV ₂ O ₄ measured at 5 K, 55 K and 100 K.	84
4.7	Temperature dependence of the (008) Bragg peak	85
4.8	Neutron powder diffraction data of CoV ₂ O ₄ measured at 5 K and the sketch of the magnetic structures for CoV ₂ O ₄	90
4.9	Reference [94], Temperature dependence of magnetization for a single crystal of CoV ₂ O ₄	93
4.10	Magnetic-field (H) dependence of strain ($\Delta L/L$) at various temperatures and Temperature dependence of magnetostriction at low- H	94
4.11	Reference [94], Temperature dependence of magnetostriction at low- H for different samples of CoV ₂ O ₄	95
4.12	Single Crystal refinement of CoV ₂ O ₄	98
4.13	Temperature dependence of the measured intensity of main magnetic Bragg peaks of a single crystal (#3) of CoV ₂ O ₄	99
4.14	Temperature dependence of the spin-flip intensity of (002) magnetic Bragg peak	101
4.15	Inelastic neutron scattering data measured using cold triple axis spectrometer CTAX at HFIR, ORNL of CoV ₂ O ₄ single crystal sample #2	104
4.16	Inelastic neutron scattering data measured using polarized triple axis spectrometer HB1 at HFIR, ORNL	105

4.18	Time of flight inelastic neutron scattering data of CoV_2O_4 single crystal sample #2 measured using ARCS spectrometer	107
4.19	Spin interactions of CoV_2O_4 spinel	109
4.20	Linear spin wave calculation to simulate the observed spinwave excitations of CoV_2O_4	110
4.21	Calculated spinwave dispersions of each spinwave model for CoV_2O_4 . . .	111

List of Tables

2.1	Properties of the neutron [22]	13
3.1	The crystal structural parameters of $\text{BaV}_{10}\text{O}_{15}$ by refining the data shown in Figure 3.5 using the program FULLPROF. B_{iso} is an isotropic thermal parameter expressed as $\exp(-B_{\text{iso}} \sin^2 \theta / \lambda^2)$, where θ is the scattering angle and λ is the wavelength of the neutron. R_{wp} and χ^2 correspond to the weighted R factor and chi-square. The space group symmetry is $Pbca$	42
3.2	Refined magnetic moments of V1 and V2 ions for the model M8.	56
3.3	Basis vectors (BV) of Irreducible Representations (IR) of $\text{BaV}_{10}\text{O}_{15}$ with $Pbca$ space group and $k = (0.5, 0, 0)$. Each V atom consist of 8 equivalent positions and the table summarize the basis vectors for Γ_1 and Γ_2 irreducible representations.	59
3.4	Exchange constants used for each spinwave model in figure 3.18 (model M8) for the Hamiltonian in equation 3.2	61
4.1	The crystal structural parameters of CoV_2O_4 by refining the data shown in Fig.4.6 using the program FULLPROF. B_{iso} is an isotropic thermal parameter expressed as $\exp(-B_{\text{iso}} \sin^2 \theta / \lambda^2)$, where θ is the scattering angle and λ is the wavelength of the neutron. R_{wp} and χ^2 correspond to the weighted R factor and chi-square. The space group symmetry is $Fd\bar{3}m$	86
4.2	Basis vectors for the space group $F d -3 m:2$ with $\mathbf{k}_{11} = (0, 0, 0)$. The decomposition of the magnetic representation for the Co site (.125, .125, .125) is $\Gamma_{Mag} = 1\Gamma_8^3 + 1\Gamma_9^3$. The atoms of the nonprimitive basis are defined according to 1: (.125, .125, .125), 2: (.875, .875, .875).	87
4.3	Basis vectors for the space group $F d -3 m:2$ with $\mathbf{k}_{11} = (0, 0, 0)$ for V site (.5, .5, .5). $\Gamma_{Mag} = 1\Gamma_3^1 + 1\Gamma_5^2 + 1\Gamma_7^3 + 2\Gamma_9^3$. Atoms, 1: (.5, .5, .5), 2: (.5, .25, .25), 3: (.25, .5, .25), 4: (.25, .25, .5).	88
4.4	Exchange constants and single ion anisotropy parameter used for each spinwave model in Figure 4.20 for the Hamiltonian in equation 4.2	108

Abbreviations

INS	I nelastic N eutron S cattering
AFM	A nti F erro M agnetism
LSW	L inear S pin W ave
NPD	N eutron P owder D iffraction

Physical Constants

Speed of Light	c	$=$	$2.997\,924\,58 \times 10^8 \text{ ms}^{-2}$	(exact)
Planck Constant	h	$=$	$6.62606957(29) \times 10^{-34} \text{ J s}$	
		$=$	$4.135667516(91) \times 10^{-15} \text{ eV s}$	
Reduced Planck Constant	\hbar	$=$	$1.054571726(47) \times 10^{-34} \text{ J s}$	
		$=$	$6.58211928(15) \times 10^{-16} \text{ eV s}$	
Mass of Electron	m_e	$=$	$9.10938215(45) \times 10^{-31} \text{ kg}$	(rest)
Mass of Neutron	m_n	$=$	$1.674927351(74) \times 10^{-27} \text{ kg}$	
Bohr Magneton	$\mu_B (= \frac{e\hbar}{2m_e})$	$=$	$9.27400968(20) \times 10^{-21} \text{ erg G}^{-1}$	
		$=$	$5.7883818066(38) \times 10^{-5} \text{ eV T}^{-1}$	
Boltzmann constant	k_B	$=$	$1.3806488(13) \times 10^{-23} \text{ J K}^{-1}$	
		$=$	$8.6173324(78) \times 10^{-5} \text{ eV K}^{-1}$	

Symbols

$E = \hbar\omega$	Energy transfer	meV
$\hbar\vec{Q}$	Momentum transfer	kg ms ⁻¹
Ω	Solid angle	sr (Steradian : dimensionless)
σ	Scattering cross section	b (1 barn = 10 ⁻²⁸ m ²)
$\frac{d^2\sigma}{d\Omega dE}$	Differential scattering cross section	$bsr^{-1}eV^{-1}$
$S(\vec{Q}, \omega)$	Scattering function	$b^{-1}sr^{-1}eV^{-1}$

Dedicated to my loving parents...

Chapter 1

Introduction

1.1 Introduction to frustrated magnets

Transition metal oxides provide a unique opportunity to study the novel phenomena of electronic and magnetic states emerging from the strong correlations of electrons: high temperature superconductors, ferromagnets, antiferromagnets, spin liquid and spin glass states, colossal magnetoresistance, Mott transition and charge ordering systems to name a few. The exotic magnetic states, particularly when different degrees of freedom are strongly correlated with each other are sometimes harder to explain. In simple metals, semiconductors or insulators, when a material has a open d electron shell, like vanadium or iron oxides, strong Coulombic repulsion is observed making them a strongly interacting system. The correlations between spin, orbital, charge and lattice are often highly pronounced in these systems, which lead to exotic phenomena. Each degree of freedom is coupled with each other and often it can be fine tuned by an external perturbation to achieve more interesting properties.

Frustrated magnets particularly attracted attention due to their possible novel quantum paramagnetic states [1, 2]. In 1973, P. W. Anderson [3] observed that in a two dimensional quantum antiferromagnet, the long range ordered state is not the only possible state, but he explained the possibility of having a superposition of short range spin singlet state, which he calls as "Resonating Valance Bond" (RVB) state. The field of frustrated magnetism has evolved greatly with numerous different studies, and still some concepts arising from the frustration have yet to be proven both experimentally and theoretically.

Frustration can be achieved in two forms, either through geometrical frustration or by competing interactions. When spins are arranged antiferromagnetically in a square

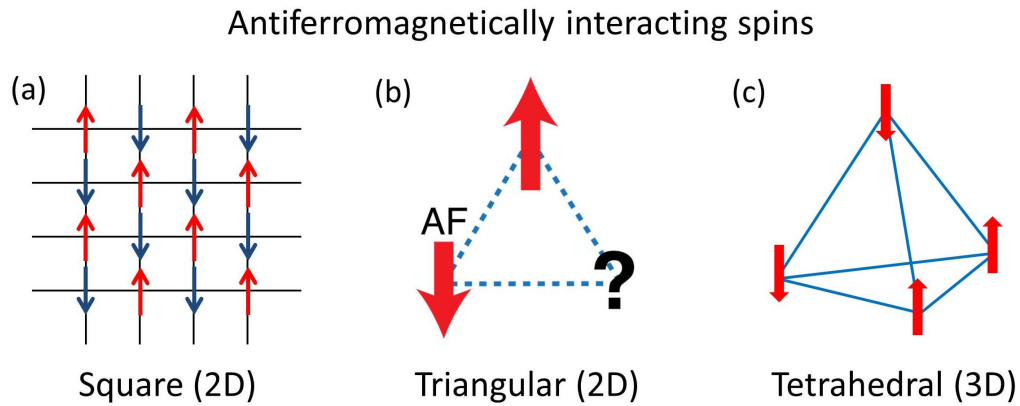


FIGURE 1.1: Antiferromagnetically interacting spins in an arrangement of a (a) Square (b) Triangular (c) Tetrahedral

lattice, it can satisfy all the exchange interactions by making all the spins anti-aligning with each other. The simplest example for geometrical frustration is when a set of spins is arranged in an antiferromagnetically coupled triangle. The geometrical property of the arrangement of triangles compete with the correlations set by the interactions between the spins, giving rise to frustration. It fails to satisfy all the antiferromagnetic magnetic interactions simultaneously with collinear arrangement of spins as shown in Fig. 1.1.

In two dimension, triangles can be arranged in a few different ways. When the triangles in 2D are sharing a common edge, they form the well known triangular lattice. Although this is a simple arrangement of spins and the 120° structure remains as the ground state for both classical and quantum spins, other various types of magnetic ordering are also found, which depend on the factors like lattice geometry, the magnitude of the spins, anisotropy, distances between magnetic ions, ligand field[4]. When the triangles share a common corner, spins are arranged in a kagome lattice. Examples for kagome lattice compound are found in Jarosite family like $\text{KFe}_3(\text{OH})_6(\text{SO}_4)_2$. $\text{ZnCu}_3(\text{OD})_6\text{Cl}_2$ in kagome lattice is another immensely studied material which can be a possible candidate for the quantum spin liquid [5–7].

In three dimension, a tetrahedron for an example, has an infinite number of spin configurations as its ground states due to two degrees of freedom related to angles θ and ϕ in 3D while maintaining a constant magnitude for the spin. The most frustrated arrangement in 3D is a network of corner sharing tetrahedra. Spinel AB_2O_4 and pyrochlores $\text{A}_2\text{B}_2\text{O}_7$ are examples for this type of arrangement of atoms. Due to its infinite degeneracy, these systems have shown various kinds of novel phases like cooperative paramagnetism (spin liquid) or when degeneracy is lifted, ferrimagnetism or antiferromagnetism or even a glassy orbital state.

An estimate about the amount of frustration of a system can be obtained from measuring bulk magnetic susceptibility. A system will follow Curie-Weiss Law $\chi(T) = C/(T - \Theta_{cw})$ at high temperatures. Θ_{cw} is positive for a ferromagnet, and it is negative for an antiferromagnet. When a frustrated magnet is cooled down, some perturbation with an energy scale of v can act to lift the degeneracy [1]. If the perturbation is strong enough to lift the degeneracy, then the system can long range order at a transition temperature T_C . The value of T_C is normally set by perturbation energy scale v . The Curie-Weiss temperature can be also expressed using the exchange interaction between the spins. That is, $\Theta_{cw} = zJS(S + 1)/3K_B$. If the magnetic system is ideal without any frustration then typically $\Theta_{cw} \simeq T_C$. But if the system is frustrated, the ordering occurs at much lower temperature. We can define frustration index as, $f = \Theta_{cw}/T_C$. In a frustrated magnet which long range orders, the frustration index is usually $\gg 1$ [8]. When the frustration index is high enough, $f \gg 100$, then the system fails to order even at the lowest possible temperature and will reside in a spin liquid state.

1.2 Phase transitions and magnetic states

Phase transitions in strongly correlated materials occur widely and sometimes lead to novel properties that can lead to technological advancement. Phase transitions that observed in magnetic systems can be either structural or magnetic. For some systems, those are correlated and structural phase transition drives the system into particular magnetic state. Phase transitions in nature can be either first or second order. A first order transition is when a system abruptly changes to a different state in a discontinuous way. In comparison, the second order transition is more gradual and changes smoothly with the order parameter.

Usually, structural phase transitions are first order transitions, where a discontinuous change in bulk properties like resistivity, heat capacity or susceptibility is observed. If the system contains magnetic ions with orbital degrees of freedom, then usually orbital ordering occurs before the structural transition changing the crystal structure by lowering the energy of the orbital state.

Magnetic phase transitions or magnetic states can be categorized as following. Upon cooling a spin system, coupling between the spins results in a phase transition to an ordered state. The thermal energy which randomizes the spins and the exchange energy which makes the spins order compete with each other. When the exchange energy wins, the system can order into mainly three different states; a ferromagnet, antiferromagnet or ferrimagnet. The change of susceptibility with the temperature for a paramagnetic, ferromagnetic and antiferromagnetic state is shown in Figure 1.2(a). The ferrimagnetic

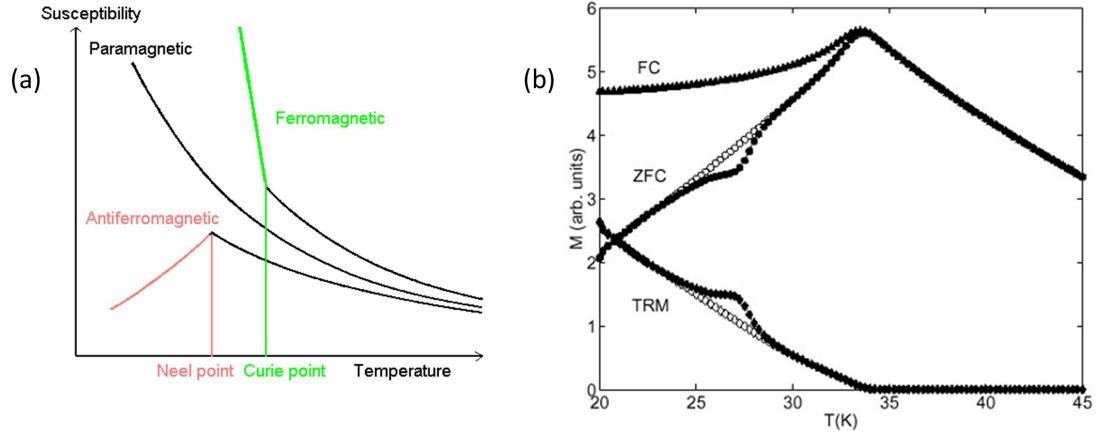


FIGURE 1.2: (a) Variation of magnetic susceptibility with temperature for paramagnetic, ferromagnetic and antiferromagnetic (from reference [11]) (b) ZFC, FC and thermoremanent (TRM) measured on heating after cooling the Ag(Mn) spin glass to 20 K and then measuring on heating. (from reference [12])

phase also follows a similar behavior as a ferromagnet. When the spins are parallel (antiparallel) to each other we have a ferromagnetic (antiferromagnetic) system and if the spins are parallel but with two different moments, then a ferrimagnetic phase appears. If the frustration is extremely large then the exchange energy is not sufficient for an ordered state to appear and system can remain in cooperative paramagnetic state or spin liquid state, where the spins change dynamically. These will not show any kind of magnetic ordering down to lowest temperature. But strong correlations will produce a spin singlet state between pairs of spins forming a dimer [9] three spins can bond with each other to make a trimer [10]. Some systems will have sufficiently large exchange energy to have a transition to a spin frozen state at low temperatures but with large number of accessible spin states. This form of ordering is known as a spin glass state. There are few characteristics that spin glass state shows. Between Zero field cooling and field cooling magnetic susceptibility χ , there will be a temperature T_c that χ diverge from each other. The broad maximum near T_c and the linear temperature dependence at low temperatures of heat capacity were also seen in spin glass states.

In this dissertation, we examine different kinds of magnetic states and various phase transitions.

1.3 Orbital ordering

Electronic orbital degrees of freedom play an important role in novel phases of strongly correlated materials. The exchange interactions between two spins greatly depend on

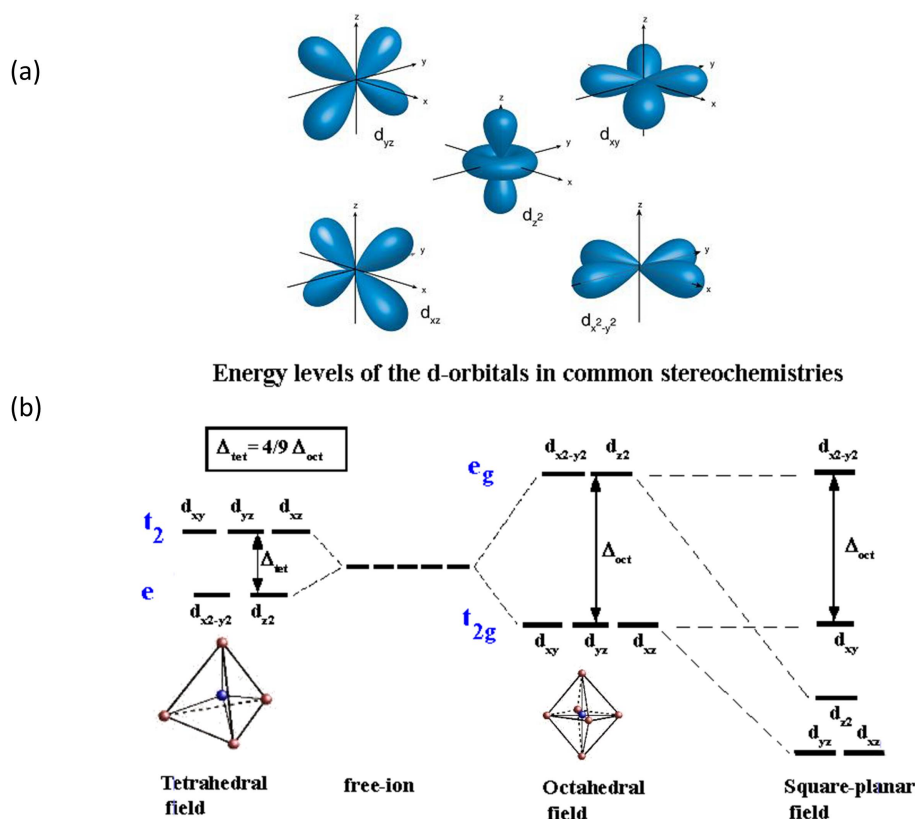


FIGURE 1.3: (a) Shape of the different d orbitals [13] (b) Energy levels of d orbitals for different crystal fields [14]

the orbital overlap between the occupied orbitals of the two ions.

There can be a different local ligand environment around a transition metal ion. According to the crystal field theory, there are two main crystal field environments that commonly observed.

An illustration of the shape of the d -orbitals, tetrahedral and octahedral crystal field environment and energy levels of d -orbitals are shown in Figure 1.3. In an octahedral crystal field, the ligand anions are along the main local axes, x , y and z . Since e_g orbitals of the cation metal are also along these directions, they feel more repulsion from the electrons in anion. Thus, in an octahedral crystal field, e_g orbitals have a higher energy than the t_{2g} orbitals. In contrast, in a tetrahedral crystal field, neither t_{2g} nor e_g orbitals lie directly along the ligand bond, but t_{2g} orbitals are much closer to the ligand. Thus, the energy of t_{2g} orbitals stays higher in the energy diagram.

The Jahn-Teller effect, published by Hermann Arthur Jahn and Edward Teller in 1937 says that "any non-linear molecular system in a degenerate electronic state will be

unstable and will undergo a distortion to form a system of lower symmetry and lower energy thereby removing the degeneracy” [15].

Let’s consider two situations of Jahn-Teller type distortions that can occur in octahedrally coordinated crystal field. If the crystal distortion is such that the local z axis undergoes a contraction, then the orbitals along the z axis will feel more repulsion than the others. Thus, d_{xy} orbital will have a lower energy compared to other two t_{2g} orbitals. Similarly, when z axis elongates, then orbitals along the z axis will feel less repulsion, and thus stay at a lower energy. These two situations are explained in Figure 1.4 (a).

Jahn Teller type crystal distortion may be driven by an orbital ordering of an orbitally active ions like V^{3+} . Three theoretical models of orbital ordering in a spinel vanadate are presented in reference [16] as shown in Figure 1.4 (b). When the crystal symmetry is changed such that $c < a$, then d_{xy} orbital will be always occupied. Depending on the other factors and the form of orbital ordering, the antiferro orbital state, the orbital-Peierls state or ferro orbital state can be occupied by the second t_{2g} electron.

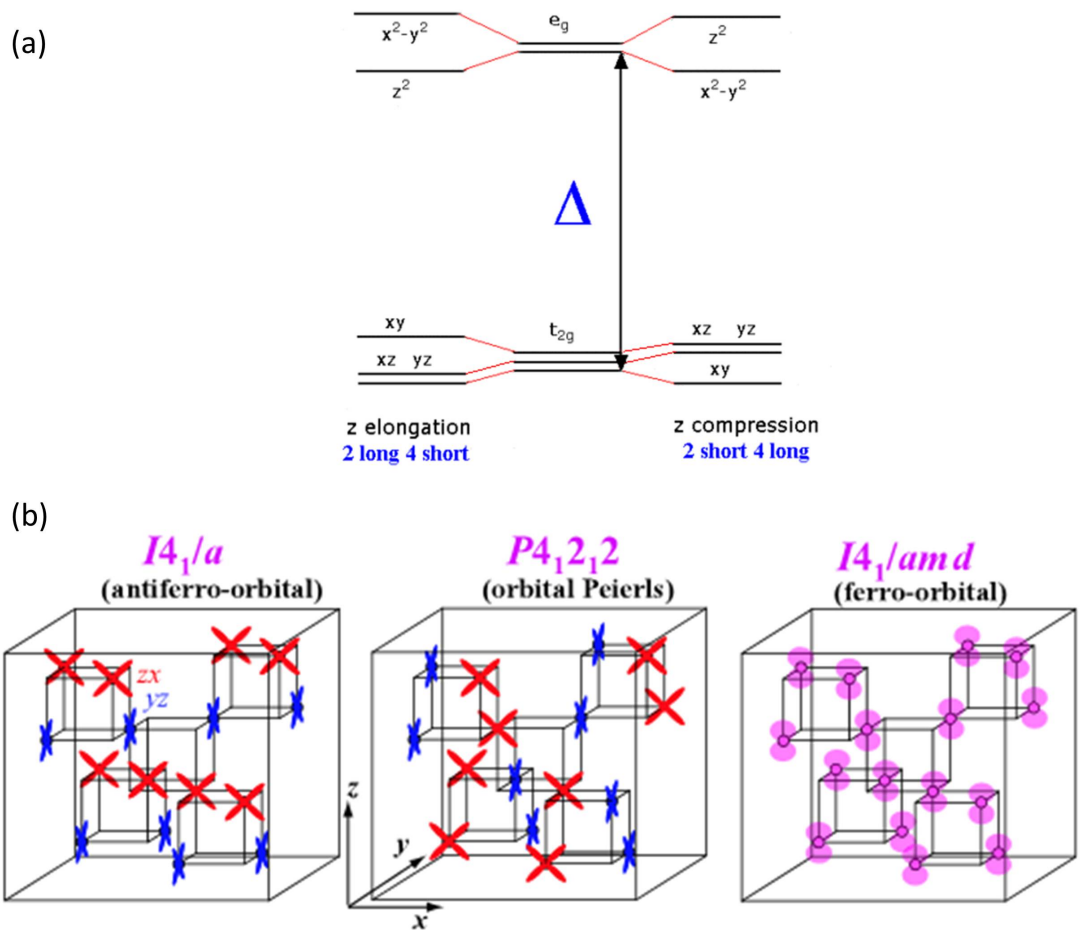


FIGURE 1.4: (a) Jahn-Teller effect for z elongation and z contraction in octahedral ligand field (From reference [17]) (b) Three theoretical models of orbital ordering in spinel vanadate. (From reference [16])

1.4 Exchange interactions

Exchange interaction is the most important coupling between the paramagnetic ions. There are three different kinds of exchange interactions: 1) direct cation - cation interaction 2) superexchange cation - anion - cation interaction 3) double exchange cation - anion - cation interaction. Magnetic exchange interactions can be ferromagnetic or antiferromagnetic. A set of rules, known as the Goodenough-Kanamori rules (Goodenough, 1955, 1958; Kanamori, 1959), is normally used to explain the magnetic properties of wide range of materials in a qualitative level.

The first kind, direct orbital coupling, requires overlapping of nearby orbitals. As shown in Figure 1.5 (a), direct cation - cation interaction occurs as a σ bond between two t_{2g} orbitals[18]. The amount of orbital overlap, and thus the strength of the interaction,

greatly depends on the distance between cations. There is a critical distance R_c where the interaction falls considerably. Direct cation - cation interactions can occur when a bond is formed by sharing either an edge or a face of the anion octahedron. These interactions are typically antiferromagnetic if there is a direct overlap between the orbitals.

Superexchange cation - anion - cation interaction occurs by mediating through an intermediate anion in between two cations. Either a σ or a π bond can occur between a cation and anion. Figure 1.5 (b) shows the two possibilities for 180° cation - anion - cation angle; $e_\sigma - p_\sigma - e_\sigma$ or $t_\pi - p_\pi - t_\pi$ [18]. Both give antiferromagnetic interactions between cations by interacting through the same kind of orbital on the anion. If a different kind of anion orbital interacts on either side with the cations, then a ferromagnetic interaction occurs which is mediated by the Coulomb exchange with the oxygen. This optimally occurs when cation - anion - cation angle is 90° . When the angle deviates from 90° towards 180° antiferromagnetic superexchange processes compete with the ferromagnetic interaction and it is sometimes difficult to predict the final nature of the interaction.

The double exchange occurs between cations by simultaneous transfer of an electron from cation to anion and anion to cation without change in the orientation of spin, which leads to ferromagnetic coupling [19, 20]. The electron has moved between the two cations and it is different from superexchange in that superexchange occurs normally between two cations with same valance, while double exchange occurs only when one cation has an extra electron compared to the other (mixed valance).

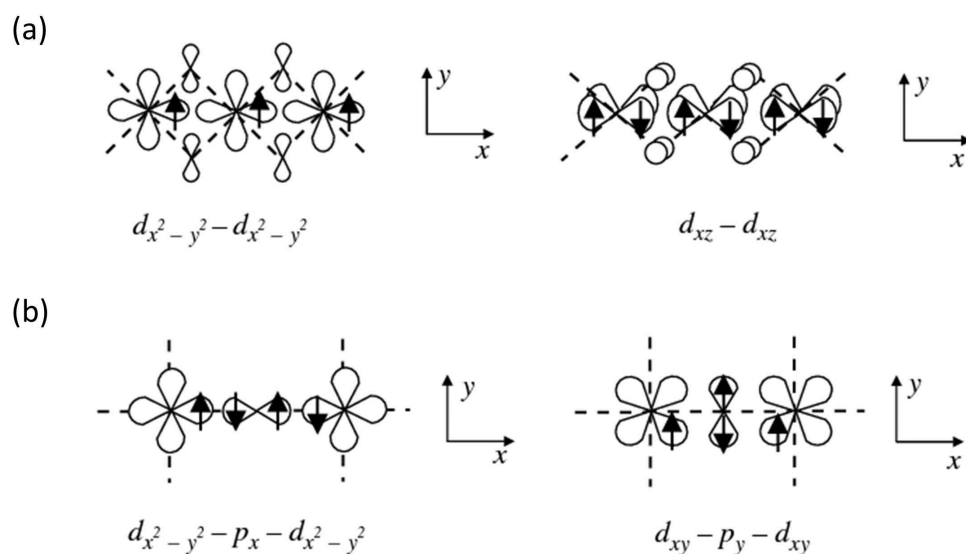


FIGURE 1.5: Exchange interactions are responsible for magnetic ordering. (a) Direct exchange : between neighboring d atomic orbitals in a transition metal compound with edge sharing octahedra. (b) Superexchange : between d atomic orbitals via ligand p atomic orbitals in a transition metal compound with vertex-sharing octahedra. (From reference [18])

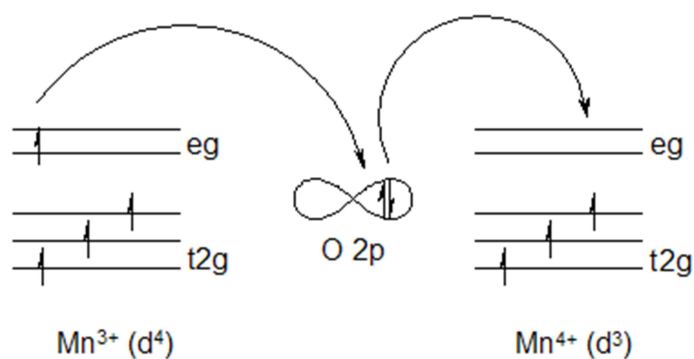


FIGURE 1.6: Double exchange mechanism between Mn^{3+} and Mn^{4+} ions (from reference [21])

1.5 Brief introduction to the materials and methods

The work done in this thesis is mainly focused on understanding the properties of magnetism in two different kinds of strongly correlated materials, the frustrated magnet $\text{BaV}_{10}\text{O}_{15}$ and the spinel CoV_2O_4 . The two vanadates, $\text{BaV}_{10}\text{O}_{15}$ and CoV_2O_4 have orbitally active V^{3+} ions which are strongly correlated with the spin, lattice and orbital degrees of freedom. Both materials show phase transitions that are either structural, electronic or magnetic.

$\text{BaV}_{10}\text{O}_{15}$ is a frustrated magnet with a frustration index of ~ 30 . It provides an excellent opportunity to study the interplay between various degrees of freedom. In addition to lattice, spin and orbital, charge degrees of freedom with mixed valance ions with a 4:1 ratio make the system more interesting. Even though there is a considerable amount of studies and interest to understand the possible trimer formation in this system, there aren't many studies to understand the ordered phase of the system.

CoV_2O_4 , which resides close to the itinerant electron limit, provides a unique situation compared to the other V spinels to study the magnetic, structural and orbital properties. The system does not show any observable structural transition from the diffraction measurements done so far but the interplay between spin, lattice and orbital degrees of freedom was found to be important for understanding the properties of this nearly metallic state.

Neutron scattering being the most versatile tool to investigate the magnetic properties of materials was used to investigate the magnetic and electronic properties of different phases in the above materials. Polarized and unpolarized elastic neutron scattering and inelastic neutron scattering, in addition to the bulk property measurements were used to study these materials. Spin excitations were observed in all these materials. Mostly the excitations are magnons and they are modeled using linear spin wave mechanisms. By using all these techniques together we provide findings that are important to understand the properties of the various phases these systems show.

First step of these studies is to understand the magnetic ground state of the system. Both materials are long range ordered. Thus, neutron diffraction measurements (powder and/or single crystal) were performed to identify the ordered magnetic state. In addition, the low temperature crystal structure was also studied. To understand the magnetic state, refinements of diffraction data were performed with Fullprof Software along with group theoretical analysis. Secondly, to understand the possible magnetic excitations of these systems, inelastic neutron scattering experiments were performed. Nature of the spin excitations were identified by analyzing the data, and magnon excitations are then modeled using Linear Spin Wave calculations. By matching the calculated spectrum

of magnon excitations with the data, a spin Hamiltonian for the system was proposed. Validity of the spin Hamiltonian was tested with possible orbital order of t_{2g} orbitals of magnetic ions and nature of the orbital order was discussed. For CoV_2O_4 system, neutron data were used along with the collaboration study about magnetostriction to find out the nature of the orbital state.

1.6 Outline of the Thesis

First, the basics of important topics such as frustrated magnetism, phase transitions and magnetic states, orbital ordering and exchange interactions are discussed. In the second chapter, fundamentals of neutron scattering, representational analysis and theory of linear spinwave calculations are presented.

The study of frustrated magnet $\text{BaV}_{10}\text{O}_{15}$, is presented in chapter 3. Using our elastic and inelastic neutron scattering data, a possible ground state for the long range ordered state was found with only two ions, V1 and V2 ordered. The spinwave simulations were also performed to model the Hamiltonian to reproduce the single crystal inelastic neutron scattering data. Possible orbital states for the system to describe the observed data and results are also discussed.

In chapter 4, neutron scattering results of spinel CoV_2O_4 is discussed. Polarized and unpolarized neutron scattering and inelastic neutron scattering results are presented. The analysis of magnetic structure, the detailed temperature dependence of the single crystal diffraction data and magnetostriction data are also discussed. Finally, linear spinwave calculations are performed to match with our inelastic neutron scattering data.

Chapter 2

Introduction to Neutron Scattering

2.1 Theory of Neutron Scattering

Neutron scattering is one of the most powerful techniques to study the properties of materials. Since the neutron was first discovered in 1932, neutron scattering has evolved in many aspects in condensed matter research and is now accepted as a one of the field's most versatile tools. In this Chapter, the theory of neutron scattering will be discussed.

2.1.1 Why Neutron?

In neutron scattering, an incident neutron beam is radiated into a sample of interest and the scattered neutrons are measured which can be used to determine how atoms are arranged and study the interactions between them. Neutrons, which are basic constituent of the matter, have it's unique properties that makes neutron scattering a powerful tool.

First, the mass of the neutron is comparable to that of the proton. Having this relatively large mass makes it easy to moderate the high energy neutrons produced by either fission or spallation of heavy nuclei. The final energy, which will be distributed as a maxwell distribution, will be determined by the temperature of the moderated medium such as water or liquid hydrogen. Neutrons after moderation have de Broglie wavelengths on the order of atomic distances in solids, which make them suitable to use in diffraction to study how the atoms are arranged in a solid. Also, the thermal neutrons produced with a near room temperature moderator medium will have energies range from 1 - 100 meV, which is the in the order of many dynamical properties observed in condensed matter such as phonon and magnon excitations.

TABLE 2.1: Properties of the neutron [22]

Spin	$\frac{1}{2}$
Rest mass, m_N	1.675×10^{-24} g
Magnetic moment	$-1.913 \mu_N$
Charge	0

The neutron has a zero net charge, which means that it can penetrate deeply into a sample. In a neutron scattering experiment different types of sample environments are used such as Cryostats, Vacuum and magnets. This property allows the neutron to easily transmit through the equipment in these sample environments. The most important consequence of having zero net charge is that it is not aware of the electronic charge cloud, thus interacting directly with the nucleus of the atom. As a result neutron scattering can probe bulk properties of materials than surface effects. In X-ray scattering the scattering length, which is a representative parameter for scattering strength, systematically increases with atomic number, however, neutron scattering length is random and falls within ~ 0.2 to 1×10^{-12} . This allows neutron scattering to see and index the light elements such as Hydrogen or Oxygen.

The neutron is made out of quarks and gluons which realize a non-zero magnetic moment for the neutron. The magnetic moment is 0.56 times the moment of a proton but directed opposite to its angular momentum. In a sample that we measure in a neutron scattering experiment there can be many atoms and some of them will carry unpaired electron spins which can interact with the magnetic moment of the incident neutrons via dipole-dipole interaction. The magnetic scattering length of an atom is comparable to the nuclear scattering length, giving a comparable scattered intensity from magnetic scattering to the nuclear scattering. Thus, the neutron is a powerful probe to measure magnetic properties of condensed matter. Since its discovery it has immensely contributed to the understanding of magnetism around us.

2.1.2 Neutron scattering instruments

In neutron scattering facilities there are several different types of equipment available. Here, four instruments that are mainly used for the collection of data in this thesis, namely, Neutron Powder Diffractometer, Triple Axis Spectrometer, Four-Circle Diffractometer and Time of Flight Spectrometer will be briefly discussed.

Neutron Powder Diffractometer (NPD), as shown in Figure 2.1 is used for structural characterization of materials in powder or microcrystalline samples with one or more phases. The obtained data are used in crystallographic analysis by the Rietveld method or other characterization purposes. The advantage of the Neutron Powder Diffractometer

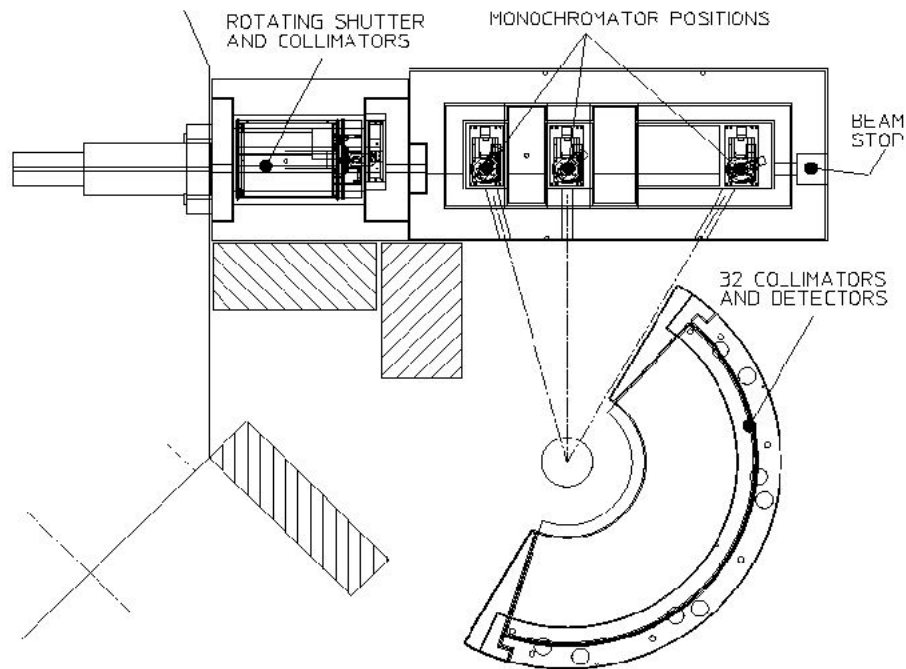


FIGURE 2.1: The schematic diagram of BT1 powder diffractometer at NIST Center for Neutron Research, National Institute of Standard and Technology [23]

compared to X ray diffractometer is it can detect any magnetic moment in a sample. If the magnetic moments have long range order, additional Bragg peaks or increases in intensity of Bragg peaks may be observed at temperatures below the ordering temperature, which can be analyzed to find the magnitude and orientation of the magnetic moments in a sample. As shown in the Figure 2.1, BT1 powder diffractometer has 32 detector instruments that can be used with three different monochromators and two different incident Soller collimators, allowing the instrument response to be tailored to the needs of the experiment [23]. Usually the neutron Powder Diffractometer can be used with furnaces, refrigerators and cryostats so that the data may be collected at wide range of temperatures spanning from 0.3 to 2000 K, and also with magnetic fields.

The triple axis spectrometer can access nearly any coordinate in energy and momentum space by controlling the axes of rotation of the monochromator, the sample and the analyzer. Figure 2.2 shows a schematic diagram of a triple axis spectrometer HB1 located at High Flux Isotope Reactor, Oak Ridge National Laboratory [24]. The first axis monochromator defines the direction and magnitude of the incident neutron beam. The second axis is at the sample where this angle selects which point in reciprocal space to be studied. The third axis corresponds to the rotation of the analyzer, where it analyzes the direction and magnitude of the scattered beam from the sample.

Powder samples do not provide adequate information to analyze complex crystals or

HB-1 Schematic Drawing

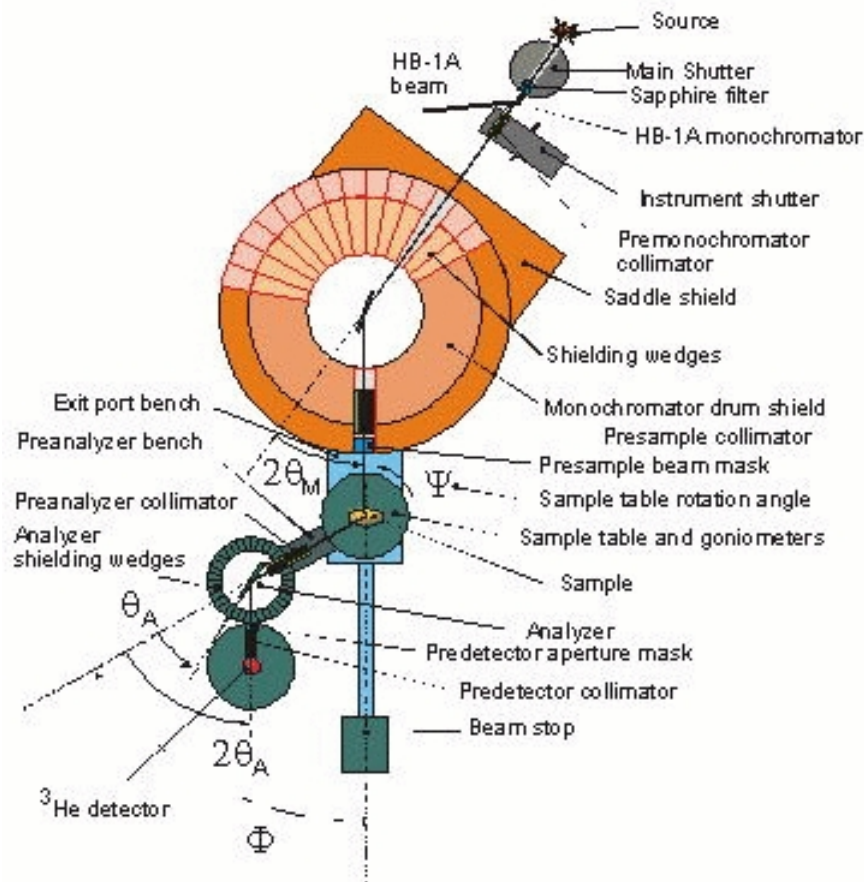


FIGURE 2.2: The schematic diagram of triple axis spectrometer at HB-1, High Flux Isotope Reactor, Oak Ridge National Laboratory.[24]

magnetic structures. They contain a number of tiny bits of crystals which are oriented in random directions and the measurements only provide a powder averaging value of scattering cross sections which is the sum of all cross sections with same wave vector magnitude. Therefore, measuring single crystals is important to study complex nuclear and magnetic structures. The four-circle diffractometer is a powerful instrument to study single crystals. It measures the integrated Bragg reflections on different lattice planes. The four variable angles; namely, Bragg angle, sample rotation angle, inclination angle and tilting angle adjust the q values of the positions in the sample and hence vary the lattice planes.

The time of flight (TOF) spectrometer [25] determines the information of microscopic motion (i.e. energy transfer) and microscopic structure of matter (i.e. momentum

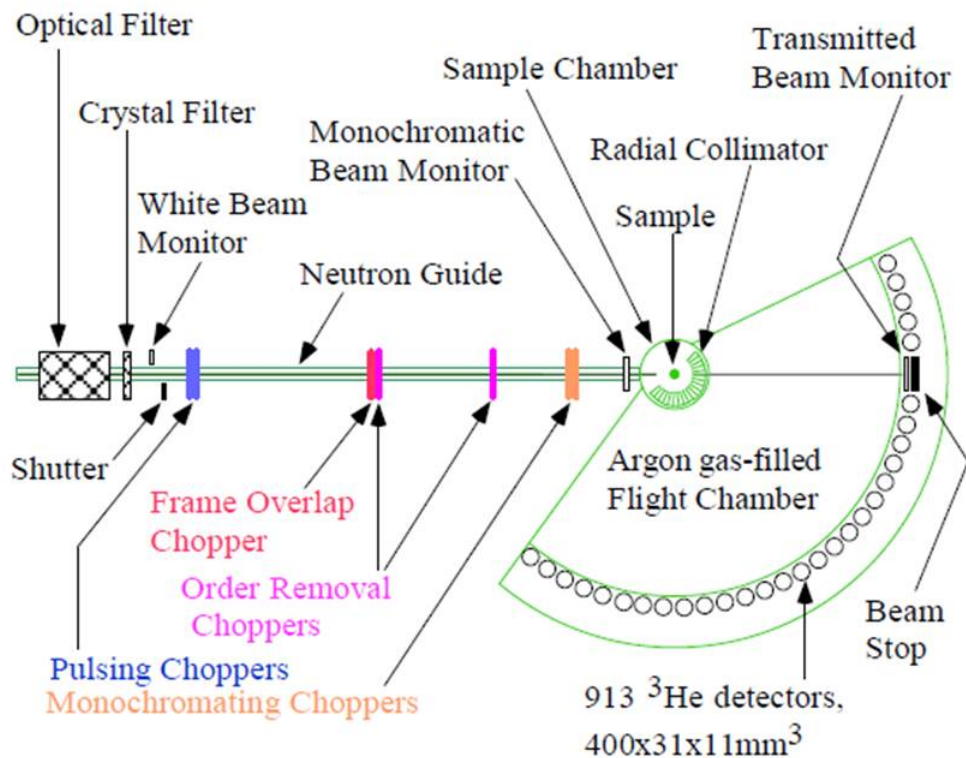


FIGURE 2.3: The schematic diagram of time of flight machine Disk Chopper Spectrometer at Nist Center for Neutron Research, National Institute of Standard and Technology [25]

transfer) by measuring the neutron time of flight, as the name implies. The initial energy is known, as the neutrons are monochromated by choppers which can be visualized as rotating discs with special openings that allow the neutrons of a particular velocity to pass. As the incident velocity of the neutrons and the distance between the source and sample are known, the time the neutron hits the sample can be calculated. As the distance between the sample and detector is known, and the neutrons time of flight between the sample and detector is measured, the scattered velocity and hence the scattered energy can be determined. The direction of the scattered neutrons and hence the direction of momentum transfer is calculated by the scattering angle corresponding to the position of the neutron detector. TOF spectrometers integrated with choppers can also be installed in steady-state reactors. The TOF is powerful as it has access to large volumes of reciprocal space simultaneously in one measurement.

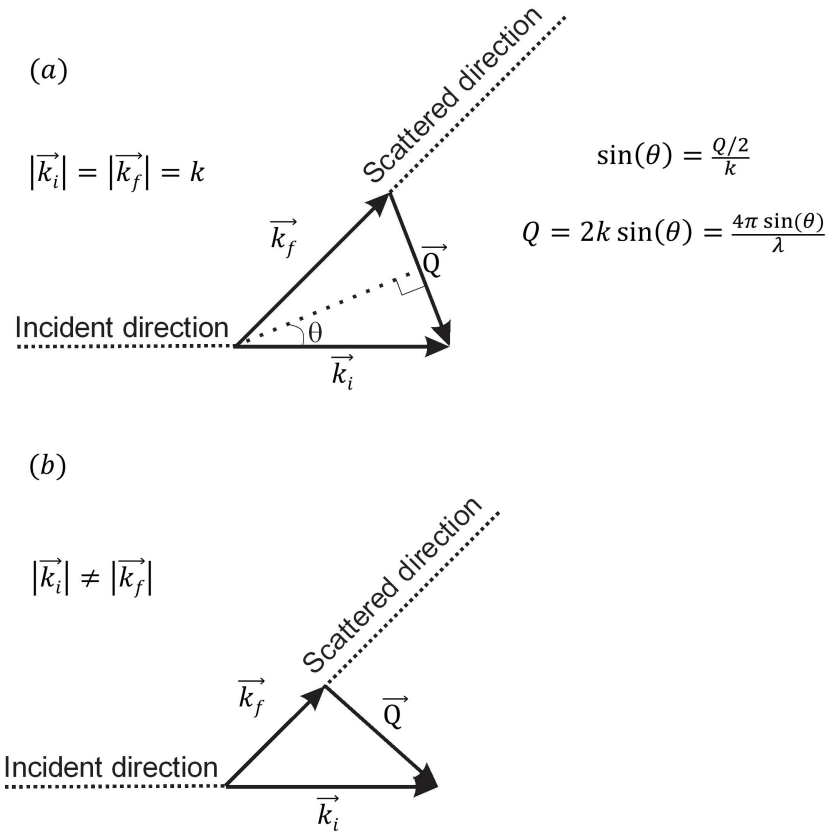


FIGURE 2.4: Scattering triangle indicated by incident wave vector \vec{k}_i , scattered wave vector \vec{k}_f and transferred wave vector $\vec{Q} = \vec{k}_i - \vec{k}_f$ a.) Elastic scattering b.) Inelastic scattering

2.1.3 Scattering Diagram

The well known scattering diagram governing the laws of momentum and energy transfer is valid for neutron scattering also.

$$\vec{Q} = \vec{k}_i - \vec{k}_f \quad (2.1)$$

$$\hbar\omega = E_i - E_f \quad (2.2)$$

where \vec{k} refers to the neutron wave vector and its magnitude $k = \frac{2\pi}{\lambda}$ where λ is the neutron wavelength. $\hbar\vec{Q}$ and $\hbar\omega$ are the momentum and energy transfer to the crystal respectively. Subscripts i and f refer to the incident and scattered/final neutron beam.

The relation between energy and momentum can be written as,

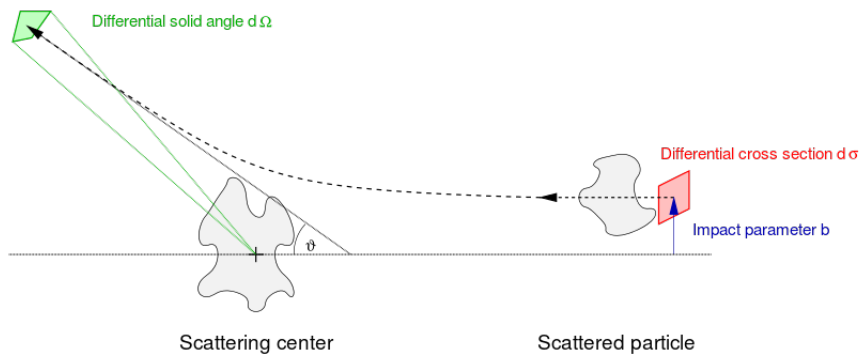


FIGURE 2.5: Differential scattering cross section [26]

$$E = \frac{\hbar^2 k^2}{2m_n} \quad (2.3)$$

where m_n is the mass of the neutron.

As shown in Fig. 2.4 (a), in elastic neutron scattering there is no energy transferred to the crystal and the initial and final magnitude of the momentum are equal. The magnitude of the momentum transfer to the crystal can be then written as a function of scattering angle θ and neutron wavelength λ as $Q = \frac{4\pi \sin(\theta)}{\lambda}$. In contrast, in inelastic neutron scattering, incident and final magnitudes of the momentum are not same leading to either energy loss or gain by the neutron.

2.2 Neutron Scattering Formula

2.2.1 Differential cross section

In a neutron scattering experiment if a sample is irradiated by a neutron beam with a wave vector \vec{k}_i and flux $\phi(k_i)$, the quantity of measurement that we are interested is the rate at which neutrons are scattered into a solid angle $d\Omega_f$, in the direction of the wave vector \vec{k}_f , with energy range of E_f and $E_f + dE_f$. This can be written as the product of $\phi(k_i)$ and the differential cross section $\frac{d^2\sigma}{d\Omega_f dE_f}$ [22]. Several basic definitions related to scattering cross section can be summarized in eq. 2.4-2.8.

$$\phi = \text{number of incident neutrons per cm}^2 \text{ per second} \quad (2.4)$$

$$\sigma = \text{total number of neutron scattered per second}/\phi \quad (2.5)$$

$$\frac{d\sigma}{d\Omega} = \frac{\text{number of neutrons scattered per second into } d\Omega}{\phi d\Omega} \quad (2.6)$$

$$\frac{d^2\sigma}{d\Omega dE} = \frac{\text{number of neutron scattered per second into } d\Omega \text{ \& } dE}{\phi d\Omega dE} \quad (2.8)$$

When a neutron hits a sample it can be considered as a very weak perturbation that does not change the nature of the sample's quantum state and scattering can cause a transition from a one quantum state to another. As a result differential scattering cross section can be written using well known Fermi's Golden Rule. If V represents the interaction operator for the neutron with the sample, then the differential cross section can be written as [22, 27]

$$\left. \frac{d^2\sigma}{d\Omega_f dE_f} \right|_{\lambda_i \rightarrow \lambda_f} = \frac{k_f}{k_i} \left(\frac{m_n}{2\pi\hbar^2} \right)^2 |\langle k_f \lambda_f | V | k_i \lambda_i \rangle|^2 \delta(\hbar\omega + E_i - E_f) \quad (2.9)$$

where initial and final states are labeled as λ_i and λ_f . Since the interaction between the sample and neutron is weak we can write the matrix element above treating incoming and outgoing neutron as plane waves.

$$\langle k_f \lambda_f | V | k_i \lambda_i \rangle = V(\vec{Q}) \langle \lambda_f | \sum_l e^{i\vec{Q} \cdot \vec{r}_l} | \lambda_i \rangle \quad (2.10)$$

$$V(\vec{Q}) = \int d\vec{r} V(\vec{r}) e^{i\vec{Q} \cdot \vec{r}} \quad (2.11)$$

where r_l are the coordinates of the scattering centers.

For a particular case of nuclear scattering the nuclear potential is just a delta function in \vec{r} . Thus, if b is the nuclear scattering length then,

$$V(\vec{Q}) = \int d\vec{r} V(\vec{r}) e^{i\vec{Q} \cdot \vec{r}} = \left(\frac{2\pi\hbar^2}{m_n} \right) b \quad (2.12)$$

If $P(\lambda_i)$ represents the statistical probability for the initial state $|\lambda_i\rangle$ by combining equation 2.9, 2.10 and 2.12, differential cross section can be written as,

$$\frac{d^2\sigma}{d\Omega_f dE_f} = \frac{k_f}{k_i} \sum_{\lambda_i, \lambda_f} P(\lambda_i) \left| \left\langle \lambda_f \left| b \sum_l e^{i\vec{Q}\cdot\vec{r}_l} \right| \lambda_i \right\rangle \right|^2 \delta(\hbar\omega + E_i - E_f) \quad (2.13)$$

After some mathematical techniques it can also be shown that [22],

$$\frac{d^2\sigma}{d\Omega_f dE_f} = N \frac{k_f}{k_i} \bar{b}^2 S(\vec{Q}, \omega) \quad (2.14)$$

where the scattering function $S(\vec{Q}, \omega)$ is defined as,

$$S(\vec{Q}, \omega) = \frac{1}{2\pi\hbar N} \sum_l \int_{-\infty}^{\infty} dt \left\langle e^{-i\vec{Q}\cdot\vec{r}_l(0)} e^{i\vec{Q}\cdot\vec{r}_l(t)} \right\rangle e^{-i\omega t} \quad (2.15)$$

Here N is the number of nuclei and t is time. The scattering function depends on only the momentum \vec{Q} and energy transfer $\hbar\omega$, not on the initial or final momentum or energy. In a neutron scattering experiment, goal is to determine the $S(\vec{Q}, \omega)$ which contains microscopic properties of the system.

Let's consider a monatomic sample to explain two different kinds of scattering that can present. Even in a monatomic sample scattering may contain nuclei with different scattering lengths. Having isotopes of the same element or relative orientation of nuclear or neutron spins may contribute to have different scattering length depending it's relative positions. Thus we can define an average scattering length \bar{b} which depends only on the collective scattering. Furthermore including the random fluctuations of scattering length of the sites the total scattering length squared is given by \bar{b}^2 . Thus we can rewrite equation 2.14 as,

$$\frac{d^2\sigma}{d\Omega_f dE_f} = N \frac{k_f}{k_i} \bar{b}^2 S(\vec{Q}, \omega) + N \frac{k_f}{k_i} (\bar{b}^2 - \bar{b}^2) S(\vec{Q}, \omega) \quad (2.16)$$

The first term in equation 2.16 is called the **coherent scattering**, while the second term is called the **incoherent scattering**. Coherent scattering cross section which

can be defined as $\sigma_{coh} = 4\pi\bar{b}^2$ describes cooperative phenomena among different atoms. Examples are Bragg scattering which can give us information about how the atoms are arranged in a crystal or information about dynamics of atoms and associated spins like phonons and magnons. On the other hand the incoherent cross section $\sigma_{inc} = 4\pi(\bar{b}^2 - \bar{b}^2)$ provides information about self-correlations such as diffusion. This thesis work is mainly focused on coherent neutron scattering.

2.2.2 Elastic Neutron Scattering

2.2.2.1 Nuclear Elastic Scattering

Elastic neutron scattering happens when the energy and momentum of the incident and scattered is conserved without any loss or gain. Thus we have $|\vec{k}_i| = |\vec{k}_f|$.

The well known Bragg condition is then,

$$\vec{Q} = \vec{\tau} = \vec{k}_i - \vec{k}_f \quad (2.17)$$

$$|\vec{Q}| = \frac{4\pi \sin(\theta)}{\lambda} \quad (2.18)$$

where $\vec{\tau}$ is a reciprocal lattice vector.

The scattering function mentioned above can be written in terms of the atomic density operator as the Fourier transform of the time-dependent pair-correlation function.

$$S(\vec{Q}, \omega) = \frac{1}{2\pi\hbar N} \int_{-\infty}^{\infty} dt e^{-i\omega t} \langle \rho_{\vec{Q}}(0) \rho_{-\vec{Q}}(t) \rangle \quad (2.19)$$

$$\rho_{\vec{Q}}(t) = \sum_l e^{i\vec{Q} \cdot \vec{r}_l(t)} \quad (2.20)$$

In the case of a perfectly rigid Bravais lattice, by taking the time average of the of the density operator, coherent elastic scattering function becomes

$$S(\vec{Q}, \omega) = \delta(\hbar\omega) \frac{(2\pi)^3}{v_0} \sum_{\vec{\tau}} \delta(\vec{Q} - \vec{\tau}) \quad (2.21)$$

where τ is a reciprocal lattice vector and v_0 is the unit cell volume.

When the lattice has more than one atom per unit cell, then the elastic scattering cross section can be generalized to [22, 27],

$$\left(\frac{d\sigma}{d\Omega}\right) = N \frac{(2\pi)^3}{v_0} \sum_{\vec{\tau}} \delta(\vec{Q} - \vec{\tau}) |F_N(\vec{\tau})|^2 \quad (2.22)$$

$$F_N(\vec{\tau}) = \sum_j \bar{b}_j e^{i\vec{\tau} \cdot \vec{d}_j} e^{-W_j} \quad (2.23)$$

$F_N(\vec{\tau})$ is the nuclear structure factor which contains the information about the positions of the atoms and the displacements of the atoms. In crystallography, one measures structure factors for a large number of Bragg reflections in the reciprocal space, and then those data can be fitted to find the best structure model.

2.2.2.2 Magnetic Elastic Scattering

Since the neutron has magnetic dipole moment which is equal to $-\gamma\mu_N\sigma$ (γ gyromagnetic ratio = 1.913, μ_N = nuclear magneton and σ = spin operator), it can interact and scatter from the magnetic moments of atoms via dipole dipole interactions [22]. For now, let's assume only the scattering from spin only. For an atom with the net spin magnitude of S , magnetic moment is gS in Bohr magnetons. The cross section of the magnetic elastic scattering when the magnetic Bragg condition, $\vec{\tau}_m = \vec{k}_i - \vec{k}_f$ ($\vec{\tau}_m$ reciprocal lattice vector in the magnetic unit cell) is satisfied is

$$\left(\frac{d\sigma}{d\Omega}\right) = N_M \frac{(2\pi)^3}{v_M} \sum_{\vec{\tau}_M} \delta(\vec{Q} - \vec{\tau}_M) |\vec{M}_\perp(\vec{Q})|^2 \quad (2.24)$$

where N_M is the number of atoms in the magnetic unit cell and v_M is the magnetic unit cell volume. $\vec{M}_\perp(\vec{Q})$ is the magnetic interaction vector which is defined as,

$$\vec{M}_\perp(\vec{Q}) = \hat{Q} \times F_M(\vec{Q}) \times \hat{Q} \quad (2.25)$$

$$= (F_M(\vec{Q}) - F_M(\vec{Q}) \cdot \hat{Q}) \hat{Q} \quad (2.26)$$

where the $F_M(\vec{Q})$ is the magnetic structure factor.

The measurements of magnetic structure factor is important to find the magnetic structures. It is defined as

$$F_M(\vec{Q}) = \sum_j \vec{S}_j f_j^M(\vec{Q}) e^{i\vec{Q} \cdot \vec{d}_j} e^{-W(\vec{Q})} \quad (2.27)$$

\vec{S}_j is the spin-component of the atoms j and the $f_j^M(\vec{Q})$ is the magnetic form factor.

The above equations express the fact that only the component of spin vector S perpendicular to the momentum transfer Q contributes to the scattering amplitude.

2.2.2.3 Representational Analysis to find magnetic structure

Magnetism involves spontaneous breaking of time-reversal symmetry and often translational and rotational symmetries are also broken. Magnetic structure means to define the direction and magnitude of the magnetic moment on each magnetic ion in the crystal. Usually in a magnetic diffraction experiment, noisy, overlapping peaks make it harder to find the magnetic structure by simply assigning a moment direction for each atom in the unit cell due to the large number of free parameters. One approach is to find symmetry operations which leave the magnetic structure invariant which leads to Magnetic or Shubnikov groups. The second most useful approach is to find the transformation properties of a magnetic structure under the classical symmetry operations of crystallographic space groups and then to assign irreducible representations of the actual space group to all known magnetic structures [28]. The Representation theory [28–35] is superior over symmetry invariance and we will briefly discuss the major aspects of that in this section.

Magnetic propagation vector \vec{k}_m defines the periodicity of the magnetic structure in terms of crystallographic unit cell. If all propagation vectors are rational fractions of crystallographic reciprocal lattice vector, the structure is called commensurate and magnetic unit cell can be defined. Otherwise, the structure is periodic but incommensurate with the crystal lattice and the magnetic unit cell becomes infinitely large.

Steps to find the magnetic structure are outlined below.

1. Determine the propagation vector \vec{k}_m
2. Determine the group of the wave vector \vec{k} , G_k

The set of point group operations which transform \vec{k} into itself or into an equivalent \vec{k} vector is called the group of the wave vector, G_k .

3. Find irreducible representations (IR) of G_k using Kovalev [36] or Bradley and Cracknell [33].

4. Find the permutation and axial representations. Construct the reducible magnetic representation Γ_{Mag} .
5. Decompose Γ_{Mag} as a linear combination of IR's of G_k .

$$\Gamma_{Mag} = \sum_{\nu} n_{\nu} \Gamma_{\nu}^{\mu} \quad (2.28)$$

where n_{ν} is the number of times that the IR Γ_{ν} of order μ appears in the magnetic representation Γ_{Mag} for the chosen crystallographic site.

6. For each IR, find the basis vectors using the expression.

$$\mathbf{S}_{\lambda}^{(kv} | i) = \sum_{h \in G_k^0} d_{\lambda[\mu]}^{*kv}(g) \exp[-i\vec{k} \cdot \vec{a}_p(g, j)] \delta_{i,g[j]} \delta_h \begin{pmatrix} R_{x[\beta]}^h \\ R_{y[\beta]}^h \\ R_{z[\beta]}^h \end{pmatrix} \quad (2.29)$$

7. Construct every possible linear combination of the magnetic basis vectors and see which one(s) reproduces neutron diffraction data.

The magnetic structure is a linear combination of the basis function of the magnetic representation.

Spin of the 0^{th} cell

$$\vec{S}_{oi} = \sum_{\lambda} C_{\lambda}^v \mathbf{S}_{\lambda}^{(kv} | i) \quad (2.30)$$

Spin of the n^{th} cell ,

$$\vec{S}_{ni} = \exp(i\vec{k} \cdot \vec{t}_{\mathbf{n}}) S_{oi} \quad (2.31)$$

After finding the spin directions from these steps, scattering cross section can be found by using equations 2.27, 2.26, 2.24 to refine the neutron powder diffraction data.

2.2.3 Inelastic Neutron Scattering

Inelastic neutron scattering happens when the energy and momentum of the incident and scattered is not conserved and the neutron losses or gains some energy during the process.

Thus the energy and momentum transfer can be written as,

$$\hbar\omega = \frac{\hbar^2}{2m_n}(k_f^2 - k_i^2) \quad (2.32)$$

$$\vec{Q} = \vec{k}_f - \vec{k}_i = \vec{\tau} + \vec{k} \quad (2.33)$$

where \vec{k} is the propagation vector and $\vec{\tau}$ is a reciprocal lattice vector.

An important property of the scattering function that is related to the inelastic neutron scattering is the principle of detail balance,

$$S(-\vec{Q}, -\omega) = e^{-\frac{\hbar\omega}{K_B T}} S(\vec{Q}, \omega) \quad (2.34)$$

where K_B is the Boltzmann's constant and T is the temperature.

This property shows that the statistical weight of the initial state will be different for different regions in energy transfer. When the energy transfer is positive (neutron energy loss/ creation of excitation) intensity is much larger than the negative energy region (neutron energy gain/ annihilation of excitation).

The differential cross section for the atomic magnetic neutron scattering can be written as [22]

$$\frac{d^2\sigma}{d\Omega_f dE_f} = N/\hbar \frac{k_f}{k_i} p^2 e^{-2W} \sum_{\alpha,\beta} (\delta_{\alpha,\beta} - \hat{Q}_\alpha \hat{Q}_\beta) S^{\alpha\beta}(\vec{Q}, \omega) \quad (2.35)$$

$$S^{\alpha\beta}(\vec{Q}, \omega) = \frac{1}{2\hbar} \int_{-\infty}^{\infty} dt e^{-i\omega t} \sum_l e^{i\vec{Q}\cdot\vec{r}_l} \langle S_0^\alpha(0) S_l^\beta(t) \rangle \quad (2.36)$$

2.2.3.1 Linear spinwave calculations

The spin wave is the analogue of the normal mode of nuclear displacements, or phonons. Spinwave energy is quantized. When the angular frequency of the wave is ω , the energy relative to its ground state is $n\hbar\omega$ where n is an integer. The quantum of energy $\hbar\omega$ is known as a magnon.

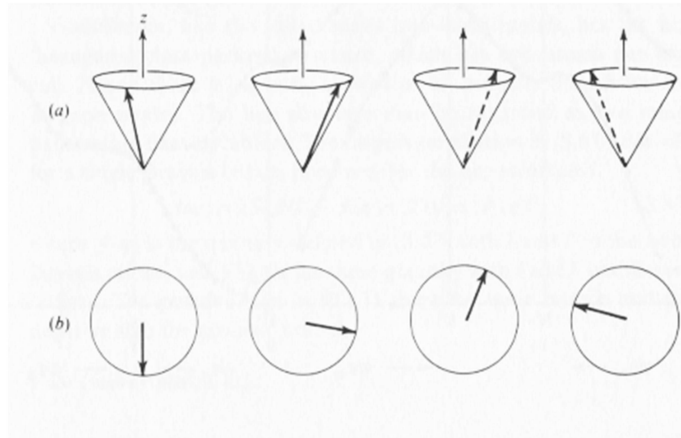


FIGURE 2.6: (a) Physical picture of a spin wave. The z axis is the mean direction of the spin vector. (b) Projection of S in the xy plane. From reference [27]

In this thesis, magnetic excitations due to spinwave are modeled using the linear spin wave theory. Here, I will discuss an example of linear spinwave theory to calculate the dispersion[27, 37].

Consider a Heisenberg Hamiltonian with nearest neighbor interactions.

$$H = \sum_{i,j} J_{i,j} \vec{S}_i \cdot \vec{S}_j \quad (2.37)$$

Let S_l^x , S_l^y , S_l^z be the operators for the atom l corresponding to the x, y, z components of spin angular momentum.

Denote eigen state of S^z (omitting subscript l) with eigen value M by $|M\rangle$.

Define operators

$$S^+ = S^x + iS^y \text{ and } S^- = S^x - iS^y \quad (2.38)$$

$$S^+ |M\rangle = \{(S - M)(S + M + 1)\}^{1/2} |M + 1\rangle \quad (2.39)$$

$$S^- |M\rangle = \{(S + M)(S - M + 1)\}^{1/2} |M - 1\rangle \quad (2.40)$$

Let $n = S - M$ to renumber the states in terms of spin deviations

$$S^+ | n \rangle = (2Sn)^{\frac{1}{2}} \left(1 - \frac{n-1}{2S} \right)^{1/2} | n-1 \rangle \quad (2.41)$$

$$S^- | n \rangle = (2Sn)^{\frac{1}{2}} \left(1 - \frac{n}{2S} \right)^{1/2} | n-1 \rangle \quad (2.42)$$

Define a pair of creation and annihilation operators for spin deviations,

$$a | n \rangle = n^{1/2} | n-1 \rangle \quad \text{and} \quad a^\dagger | n \rangle = (n+1)^{1/2} | n+1 \rangle \quad (2.43)$$

Then ,

$$aa^\dagger | n \rangle = (n+1) | n \rangle \quad \text{and} \quad a^\dagger a | n \rangle = n | n \rangle \quad (2.44)$$

$$[a, a^\dagger] = 1 \quad (2.45)$$

Linear Approximation

We now make an approximation which is to neglect $\frac{n-1}{2S}$ and $\frac{n}{2S}$ in Eq 2.41-2.42

Thus,

$$S_l^+ = (2S)^{1/2} a_l \quad (2.46)$$

$$S_l^- = (2S)^{1/2} a_l^\dagger \quad (2.47)$$

Also,

$$S_l^z | n \rangle = (S - n) | n \rangle \quad (2.48)$$

$$S_l^z = S - a_l^\dagger a_l \quad (2.49)$$

$$\mathbf{S}_1^x = \sqrt{\frac{\mathbf{S}}{2}} (\mathbf{a} + \mathbf{a}^\dagger) \quad (2.50)$$

$$\mathbf{S}_1^y = i\sqrt{\frac{\mathbf{S}}{2}} (\mathbf{a}^\dagger - \mathbf{a}) \quad (2.51)$$

$$\mathbf{S}_1^z = \mathbf{S} - \mathbf{a}_1^\dagger \mathbf{a}_1 \quad (2.52)$$

We are looking for excitations which can be characterized by a well-defined momentum \vec{k} . Introduce Fourier transform of operators,

$$a_k = N^{-\frac{1}{2}} \sum_j e^{i \vec{k} \cdot \vec{r}_j} a_j \quad (2.53)$$

$$a_k^\dagger = N^{-\frac{1}{2}} \sum_j e^{-i \vec{k} \cdot \vec{r}_j} a_j^\dagger \quad (2.54)$$

The inverse transformation is then given by,

$$a_j = N^{-\frac{1}{2}} \sum_k e^{-i \vec{k} \cdot \vec{r}_j} a_k \quad (2.55)$$

$$a_j^\dagger = N^{-\frac{1}{2}} \sum_k e^{i \vec{k} \cdot \vec{r}_j} a_k^\dagger \quad (2.56)$$

We need to express the Hamiltonian in terms of magnon variables a_k .

Magnon variables satisfy following commutation relations,

$$[a_k, a_{k'}^\dagger] = \delta_{kk'} \quad (2.57)$$

$$[a_k, a_{k'}] = 0 \quad (2.58)$$

$$[a_k^\dagger, a_{k'}^\dagger] = 0 \quad (2.59)$$

Let's consider the simplest example of an insulating antiferromagnet described by the Heisenberg Hamiltonian,

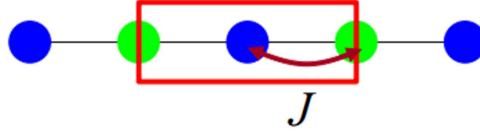


FIGURE 2.7: Linear aniferromagnet chain with two sublattice

$$H = J \sum_{j\delta} \vec{S}_j \cdot \vec{S}_{j+\delta} \quad (2.60)$$

There are two sublattices A and B and the nearest neighbor interaction J is between one of the atoms in sub lattice A and sub lattice B as shown.

Following previous results,

$$\mathbf{S}_{jx}^a = \sqrt{\frac{S}{2}} (\mathbf{a}_j + \mathbf{a}_j^\dagger) \quad (2.61)$$

$$\mathbf{S}_{jy}^a = i\sqrt{\frac{S}{2}} (\mathbf{a}_j^\dagger - \mathbf{a}_j) \quad (2.62)$$

$$\mathbf{S}_{jz}^a = S - \mathbf{a}_j^\dagger \mathbf{a}_j \quad (2.63)$$

$$\mathbf{S}_{lx}^b = \sqrt{\frac{S}{2}} (\mathbf{b}_l + \mathbf{b}_l^\dagger) \quad (2.64)$$

$$\mathbf{S}_{ly}^b = i\sqrt{\frac{S}{2}} (\mathbf{b}_l^\dagger - \mathbf{b}_l) \quad (2.65)$$

$$\mathbf{S}_{lz}^b = S - \mathbf{b}_l^\dagger \mathbf{b}_l \quad (2.66)$$

Introduce magnon variables,

$$a_k = N^{-\frac{1}{2}} \sum_j e^{i \vec{k} \cdot \vec{r}_j} a_j a_k^\dagger = N^{-\frac{1}{2}} \sum_j e^{-i \vec{k} \cdot \vec{r}_j} a_j^\dagger \quad (2.67)$$

$$b_k = N^{-\frac{1}{2}} \sum_j e^{i \vec{k} \cdot \vec{r}_j} b_j b_k^\dagger = N^{-\frac{1}{2}} \sum_j e^{-i \vec{k} \cdot \vec{r}_j} b_j^\dagger \quad (2.68)$$

Summation should be carried out separately for two atoms in the unit cell, between corresponding nearest neighbors. By writing S_j using Bose operators, converting them

to magnon variables and keep only bilinear terms, we find ,

$$H = 2JNzS^2 - 2JzS \sum_k \gamma_k \left(a_k^\dagger b_k^\dagger + a_k b_k \right) + (a_k^\dagger a_k + b_k^\dagger b_k) \quad (2.69)$$

Where

$$\gamma_k = z^{-1} \sum_{\delta} e^{i\vec{k} \cdot \vec{\delta}} \quad (2.70)$$

Merely expressing the Hamiltonian to bilinear order in the magnon variables does not diagonalize it immediately. We can however perform a canonical transformation to bring the Hamiltonian into diagonal form.

$$\alpha_k = u_k a_k - v_k b_k^\dagger \quad (2.71)$$

$$\beta_k = u_k b_k - v_k a_k^\dagger \quad (2.72)$$

$$\alpha_k^\dagger = u_k a_k^\dagger - v_k b_k \quad (2.73)$$

$$\beta_k^\dagger = u_k b_k^\dagger - v_k a_k \quad (2.74)$$

u_k, v_k are real and satisfy $u_k^2 - v_k^2 = 1$.

One such choice is $u_k = \cosh(\theta_k)$ and $v_k = \sinh(\theta_k)$. For each k , choose the angle θ_k such that the anomalous terms like $a_k^\dagger b_k^\dagger$ vanish. One then finds the solution,

$$\tanh(2\theta_k) = -\gamma_k \quad (2.75)$$

$$H = 2JNzS^2 - 2JzS \sum_k (1 - \gamma_k^2) (\alpha_k^\dagger \alpha_k + \beta_k^\dagger \beta_k + 1) \quad (2.76)$$

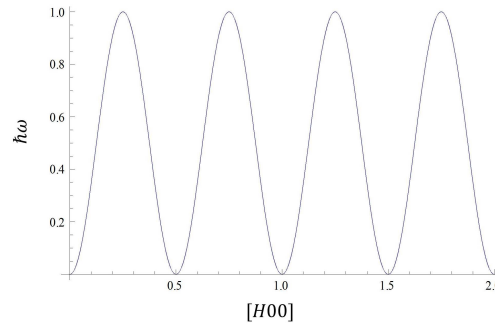


FIGURE 2.8: Dispersion of spinwave mode for linear 1D antiferromagnet chain

$$\omega_k = 2JzS (1 - \gamma_k^2) \quad (2.77)$$

For antiferromagnetic linear 1D chain,

$$z = 2 \text{ and } \gamma_k = \cos(\vec{k} \cdot \vec{\delta})$$

$$\omega_k = 4JS (1 - \cos^2(\vec{k} \cdot \vec{\delta})) \quad (2.78)$$

Figure 2.8 shows the spinwave dispersion along $[H00]$ direction for the linear antiferromagnetic chain.

Another example for linear spin wave calculation is discussed in Appendix A. In that example, linear spinwave calculations are performed analytically to find the Dynamical matrix, then the Hamiltonian is diagonalized using Mathematica and powder averaged neutron scattering cross section is calculated to reproduce the inelastic neutron scattering data[38].

In this thesis, for calculation of spinwave dispersion and intensity in the third and fourth chapters, SpinW program [39] written in Matlab software was used. The code was modified according to our systems. Also in the program additional Matlab routine was written to perform the energy convolution correctly using the experimental energy resolution values.

Chapter 3

Orbital and magnetic states of frustrated magnet $\text{BaV}_{10}\text{O}_{15}$

3.1 Introduction

Transition metal oxides have attracted attention due to the various phase transitions and ground states that they show. Among them Vanadium oxides which can have a wide range of stable oxidation ranging from 2+ to 5+ show various novel phenomena. The interplay between orbital with spin and lattice degrees of freedom has been studied in different V systems. For example, LiVO_2 having orbitally active magnetic V^{3+} ions exhibits formation of trimers at 500 K driven by a structural phase transition with an orbitally ordered spin-singlet low temperature state[10]. When the mixed valence V ions with more than one oxidation state is introduced in addition, the system exhibits more complex behaviors. Mixed valence systems with $\text{V}^{4+}/\text{V}^{5+}$ or $\text{V}^{4+}/\text{V}^{3+}$ have been studied extensively and various phenomena like charge ordering and spin gap formation [40–42], charge ordering and metal insulator transition [43, 44] and metallic weak ferromagnetism [45–47] have been observed. Mixed valence ions with $\text{V}^{2+}/\text{V}^{3+}$ are comparatively less studied with limited number of oxides available. $M\text{V}_{10}\text{O}_{15}$ ($M=\text{Sr},\text{Ba}$) is one of the examples for a system with $\text{V}^{2+}/\text{V}^{3+}$, which has multiple interesting phases that coexist [48–50].

$\text{BaV}_{10}\text{O}_{15}$ [48–53] can be considered as Ba^{2+} doped V_2O_3 . V_2O_3 with V^{3+} ions exhibits rich phases, and most interestingly it undergoes a transition from metallic state to Mott insulator at 160 K [54–56]. Doping with Ba^{2+} changes the oxidation state of V ions to 2.8+ for $\text{BaV}_{10}\text{O}_{15}$. This reduction of V^{3+} by 20 %, nominally accounts for four out of five V ions to be V^{3+} and one with V^{2+} . High temperature crystal structure of $\text{BaV}_{10}\text{O}_{15}$ is orthorhombic with $Cmca$ symmetry with three different kinds of V ions [49]. V ions

form an interesting pattern which is previously referred as V "boats" as shown in Figure 3.1 (a). Each V ion is octahedrally coordinated by six oxygen ions and V boat in the $z=1/4$ plane is 180° rotated with the V boat in the $z=0$ plane. Bonds between each V ion in these planes are edge shared with each other to form a bi-layered structure. These bi-layers are then translated by $x=0.5$ for $z=-1/4$ plane [50]. Although it is previously reported as a bilayered structure with negligible overlap between the two bi-layers, a face shared bond (or weak corner shared bonds) in the octahedra connects these two bi-layers together, making it more like a three dimensional structure. Upon cooling, it is previously reported that this system undergoes a first order phase transition at $T=130$ K from $Cmca$ to $Pbca$ symmetry and proposed a V dimerization as the driving force for the structural phase transition [48, 57].

BaV₁₀O₁₅ system attracted much more attention after the study of T. Kajita *et al.* [50] about the detailed crystal structure, magnetization, resistivity and conductivity using a single crystal of BaV₁₀O₁₅. According to that study, the resistivity and bulk susceptibility show a discontinued jump at $T_S=123$ K, where crystal structure changes from $Cmca$ orthorhombic phase to another orthorhombic phase with $Pbca$ symmetry. Upon further cooling, bulk susceptibility along a direction starts to decrease as the system undergoes the antiferromagnetic transition at $T_N=43$ K with an easy axis along a . Along b and c directions the susceptibility increase. In the low temperature phase, there are five different kinds of V ions, namely V1 (red), V2 (blue), V3 (Dark green), V2B (sky blue) and V3B (green) as shown in Figure 3.1 (b). The single crystal diffraction data show more than 3 % contraction of three V bonds. It is predicted that three ions, V2B, V3 and V3B form a "trimer" and the trimer atoms are not ordered forming a spin singlet state. This is further supported by the optical conductivity measurements where a charge gap of ~ 0.3 eV was observed, which was induced by the trimer formation at T_S .

Subsequent studies of BaV₁₀O₁₅ using various kinds of measurements tried to understand the possible nature of the trimer formation. Using NMR measurements, it has been shown that the spin-singlet V trimer formation in a itinerant phase above the semiconductor-insulator transition temperature $T_{SI}=140$ K [52]. Below T_{SI} , the observation of the asymmetric electric hyperfine coupling tensor agreed with the orbital order that they proposed giving direct d-d bonds of the trimer [52]. The orbital state of the V trimers were further investigated by resonant x-ray scattering, where they found that orbital ordering proposed by Pen *et al.* is more appropriate to describe their data. Another Raman scattering study also confirmed the existence of disorder originating from the orbital degrees of freedom above T_S and its suppression by long range orbital ordering below T_S [51].

Although there had been several studies performed to understand the nature of the trimer formation at T_S , the exact nature of the low temperature long range ordered phase below T_N had not been known. According to a previous study, BaV₁₀O₁₅ has a very complex magnetic structure although the exact magnetic structure was not reported. In this study we performed elastic and inelastic neutron scattering experiments to understand the ground state of the long range ordered phase. By combining both elastic and inelastic data, we here present a possible simple magnetic structure and a spin Hamiltonian that can explain our data quite well. Possible orbital states for the system are also studied.

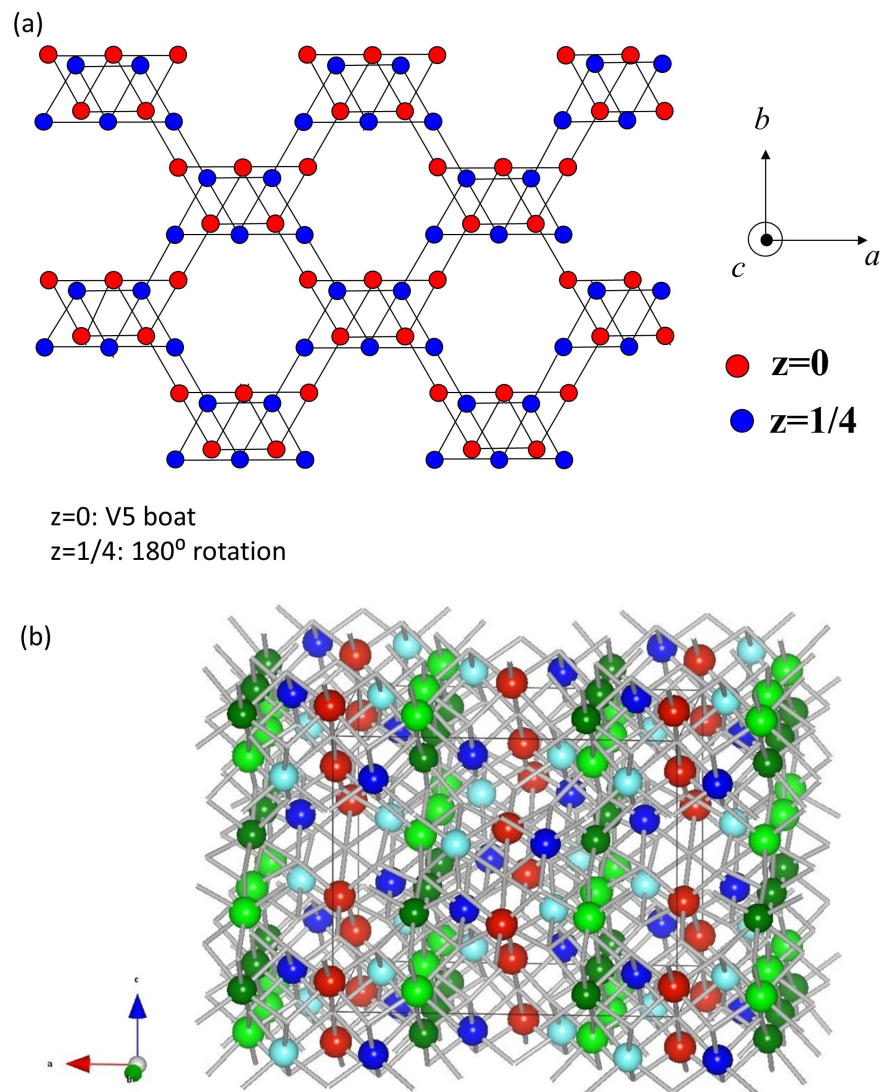


FIGURE 3.1: Arrangement of V ions in BaV₁₀O₁₅ (a) V "boats" in the ab plane (b) V ions in the Low temperature *Pbca* phase with five different V ions, namely V1 (red), V2 (blue), V3 (Dark green), V2B (sky blue) and V3B (light green)

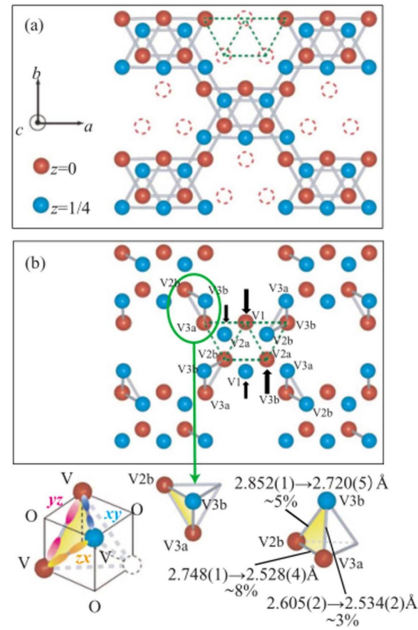


FIGURE 3.2: Figure from reference [50]. (a) The arrangement of the V ions in $BaV_{10}O_{15}$ for $z=0$ and $z=1/4$. (b) V-V bonds showing a contraction with trimer formation that associated with structural phase transition. Lower panel : V trimer with the changes of bond length and possible orbitals in the trimer

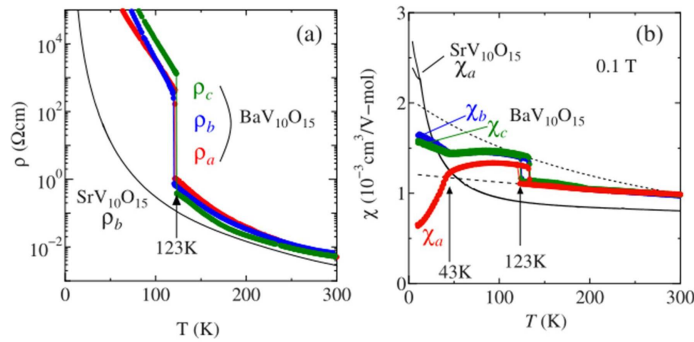


FIGURE 3.3: Figure from reference [50]. Temperature dependence of (a) resistivity (b) magnetic susceptibility for $BaV_{10}O_{15}$ and $SrV_{10}O_{15}$

3.2 Methods

3.2.1 Experimental details

Single crystals and polycrystalline samples of BaV₁₀O₁₅ were synthesized by Prof. Takuro Katsufuji's group at Waseda University, Japan. Large single crystals of approximately 2 inches long were grown by the floating-zone technique. Magnetization of the BaV₁₀O₁₅ sample was measured by Physical Property Measurement System (PPMS) with Vibrating Sample Magnetometer (VSM) insert. Neutron powder diffraction (NPD) measurements were performed on the HB2A powder diffractometer with incident neutron wavelength of $\lambda = 2.41 \text{ \AA}$ at two different temperatures above and below the magnetic transition temperature $T_N = 43 \text{ K}$. The powder sample was loaded into an aluminum can in a He atmosphere and mounted in a closed-cycle refrigerator. Inelastic single crystal neutron scattering (INS) measurements were performed at time of flight neutron scattering spectrometer ARCS at Spallation Neutron Source, ORNL with monochromatic neutrons of two different incident energies $E_i = 60 \text{ meV}$ and $E_i = 120 \text{ meV}$. The single crystal sample was aligned in $[HH0]$ plane for all the single crystal experiments. Inelastic powder neutron scattering (INS) measurements were performed at time of flight chopper spectrometer MARI at ISIS, United Kingdom with collaboration with Takatsugu Masuda and Minoru Soda at Institute of Solid State Physics (ISSP), Japan. The data were collected at several different temperatures ranging from 300 K to 5 K to study the temperature evolution of higher energy magnetic excitations with neutron incident energy of $E_i = 150 \text{ meV}$.

3.2.2 Calculation details

Neutron diffraction data were analyzed to find the crystal and magnetic structure of BaV₁₀O₁₅. Rietveld refinements were carried out using the FULLPROF program [58]. Group theoretical analysis to find the magnetic structure was performed using Sarah software [35]. Linear spinwave calculations were performed using a modified code of SpinW program [39] written in Matlab with proper convolution of energy resolution.

3.3 Bulk susceptibility and Elastic and inelastic neutron scattering data

3.3.1 Bulk susceptibility

To understand and check the transitions previously reported in the BaV₁₀O₁₅, bulk magnetic susceptibility measurements were performed using Vibrating Sample Magnetometer option in PPMS. The susceptibility was measured only along a direction to confirm the transitions.

Similar to the previously reported results, the T dependence of the magnetic susceptibility shows several anomalies. Upon cooling the sample, magnetic susceptibility shows a 25% jump around $T_S = 130$ K showing a first order structural phase transition. Upon further cooling the magnetic susceptibility along a axis decreases and changes the slope at $T_N = 43$ K indicating an antiferromagnetic ordering along a axis as shown in Figure 3.4.

Curie-Weiss law, $\chi(T) = C/(T - \Theta_c)$ can be used to fit the temperature dependence of magnetic susceptibility. C is a material-specific Curie constant, T is absolute temperature measured in Kelvin (K), and Θ_c is the Curie temperature, measured in Kelvin (K). The fitting for temperatures above the structural transition temperature is shown in the inset of Figure 3.4. From the fitting for $T > 130$ K, the Curie constant of $C = 1.21$ K cm³/V-mol and the Curie temperature $\Theta_c = -912$ K were obtained. The effective magnetic moment p_{eff} is $3.102 \mu_B$ by using the obtained Curie constant. If we assume V spins are localized in high spin state having four out of five, V spins are with $S = 1$ ($3d^2$) and $S = 3/2$ ($3d^3$), then the effective magnetic moment p_{eff} is $3.066 \mu_B$. This suggests that a possible charge ordering occurs in this system with four V^{3+} and one V^{2+} ions. Immediately below the structural transition temperature, p_{eff} seems to be decreased but the Curie temperature Θ_c varies between $T_S = 130$ K and $T_N = 43$ K. It is previously reported that Θ_c varies from 280 K (immediately below T_S) to 350 K (immediately above T_N) [50]. Although the structural phase transition relieves the frustration to some extent due to decrease of Θ_c by possible orbital ordering, the V spins in this phase are still highly frustrated, with frustration index (Θ_c/T_N) of around 6.5 to 8.

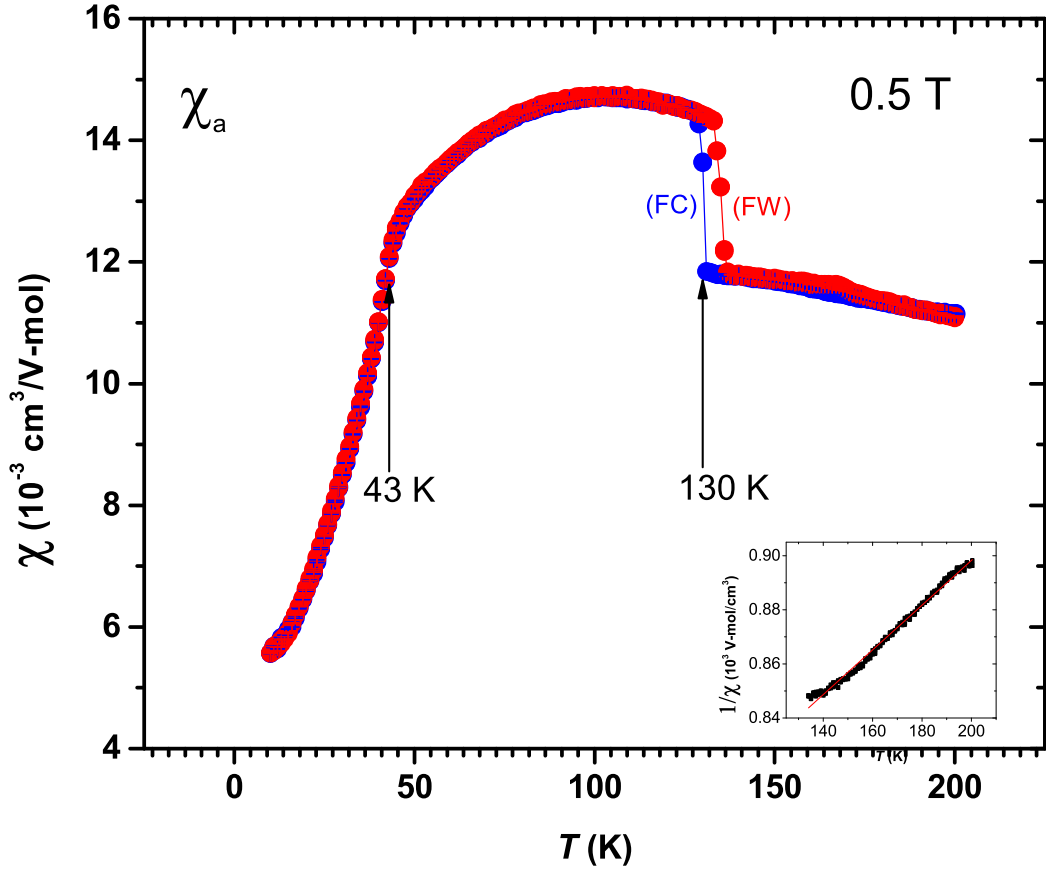


FIGURE 3.4: Temperature dependence of magnetic susceptibility for $BaV_{10}O_{15}$ along the a axis. Inset : Curie-Weiss fitting above the transition temperature

3.3.2 Neutron diffraction and Crystal Structure

Figure 3.5 (a) shows the neutron powder diffraction data measured at 4 K and the refinement of the data with the $Pbca$ symmetry using Fullprof. The aluminum peaks are excluded from the powder spectrum during the refinement. The crystal symmetry changes from $Cmca$ to $Pbca$ at the structural transition temperature of 130 K. The refined crystal structure parameters at 4 K are summarized in Table 3.1 which agree with the values published previously for 100 K in reference [50].

Our main focus in the powder diffraction experiment is to find out the magnetic structure of $BaV_{10}O_{15}$. Using the powder diffraction data measured at two different temperatures, above and below T_N , the main magnetic peaks were identified, which are shown in Figure 3.5 (b). The magnetic peaks can be indexed with the characteristic wave vector of $k = (0.5, 0, 0)$. The main magnetic peaks are very weak and almost hidden in the background.

Determination of the magnetic structure is difficult due to the small magnetic peaks and the many possibilities for the magnetic structure. Systematic approach considering our inelastic scattering data will be presented in the next section.

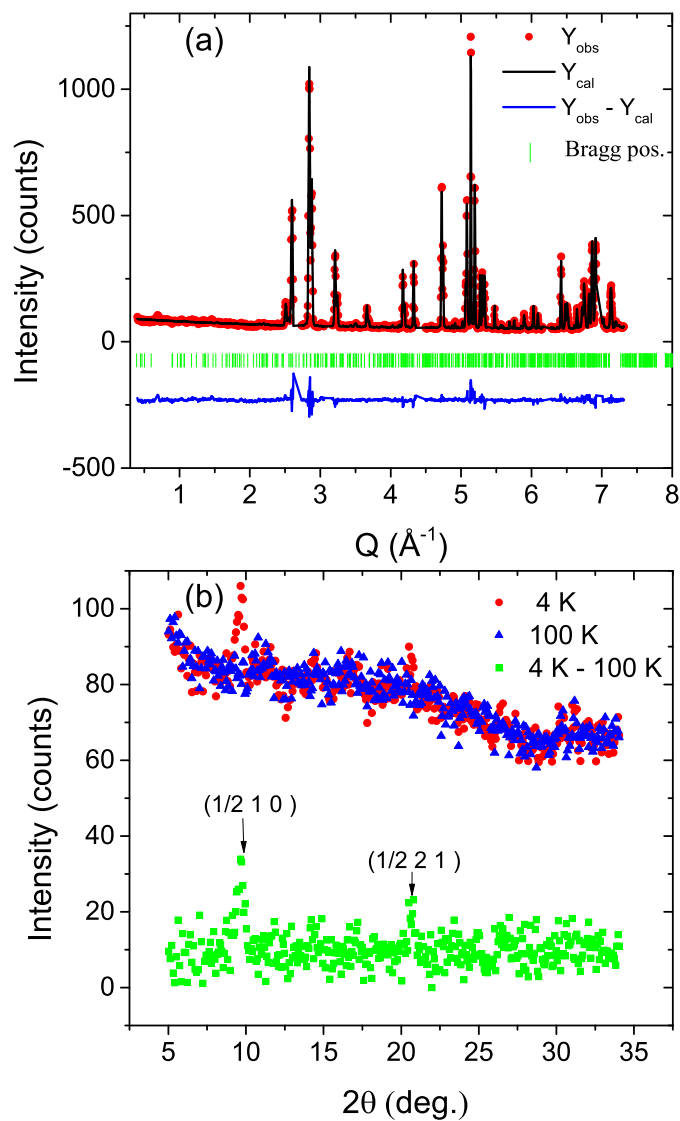


FIGURE 3.5: (a) Neutron powder diffraction data of $BaV_{10}O_{15}$ measured at 4 K. Circles are the data and the black line represents the calculated intensity obtained from the refinement by Fullprof for the crystal structure with $Pbca$ space group. Green bars represent nuclear peak positions and blue lines indicate difference between data and calculation. (b) Neutron powder diffraction data of $BaV_{10}O_{15}$ measured at 4 K and 100 K and the difference of 4 K and 100 K in the low Q region

TABLE 3.1: The crystal structural parameters of BaV₁₀O₁₅ by refining the data shown in Figure 3.5 using the program FULLPROF. B_{iso} is an isotropic thermal parameter expressed as $\exp(-B_{\text{iso}} \sin^2 \theta / \lambda^2)$, where θ is the scattering angle and λ is the wavelength of the neutron. R_{wp} and χ^2 correspond to the weighted R factor and chi-square. The space group symmetry is $Pbca$

BaV₁₀O₁₅ at 4 K, $Pbca$,
 $\chi^2 = 4.92$, $R_{wp} = 12.0$
 $a = 11.6187(7)$ $b = 9.8589(9)$ \AA , $c = 9.4221(7)$ \AA

Atom(W)	x	y	z	$B_{\text{iso}}(\text{\AA}^2)$
Ba1	0	0.5	0	0.33(3)
V1	0.506(7)	0.676(5)	0.141(3)	0.1
V2	0.365(9)	0.405(3)	0.115(4)	0.1
V3	-0.257(2)	0.656(1)	0.150(2)	0.1
V4	0.638(5)	0.163(6)	0.739(3)	0.1
V5	0.242(1)	0.846(6)	0.600(5)	0.1
O1	-0.255(8)	0.490(7)	-0.001(1)	0.31(3)
O2	0.115(8)	0.248(2)	0.002(6)	0.31(3)
O3	0.255(2)	0.329(1)	0.252(5)	0.31(3)
O4	0.632(6)	0.588(1)	0.245(4)	0.31(3)
O5	0.503(5)	0.342(5)	0.241(3)	0.31(3)
O6	0.5	0.5	0	0.31(3)
O7	0.879(5)	0.252(5)	0.513(1)	0.31(3)
O8	0.370(5)	0.912(5)	0.745(2)	0.31(3)

3.3.3 Inelastic neutron scattering data

The crystal structure and possible trimer formation in this system had been studied using single crystal diffraction, NMR measurements. However, the magnetic correlations, charge and orbital ordering were not fully understood. Thus, we performed inelastic neutron scattering experiments on a single crystal and a powder sample of BaV₁₀O₁₅ to investigate correlations between spin, charge and orbital degrees of freedom.

First, inelastic neutron scattering on a single crystal sample of BaV₁₀O₁₅ was performed at ARCS time of flight spectrometer. The single crystal was aligned in $[HK0]$ plane with incident neutron along the a^* axis. The contour maps of neutron scattering cross section along the main symmetry directions in reciprocal space are shown in Figure 3.6. The magnetic excitations showed clear and simple spinwave modes, despite having 80 magnetic ions in the magnetic unit cell. Dispersion along all three directions are unique. The most salient feature of the spinwave dispersion is the strong dispersive two modes observed along the $L([001])$ direction. It is similar to spinwave dispersion expected from antiferromagnetic or ferromagnetic chain. The previous studies emphasize that the V spins are arranged in "boat like" structure with negligible coupling along c direction. However our results of inelastic neutron scattering data measured along L direction show that coupling in c direction is finite and important in this system. Along the $H([100])$ direction, an almost dispersionless spinwave mode was observed centered around 13 meV. This means that there is negligible coupling along a direction in the V boats. Further, spinwave modes along $K([010])$ direction consist of a highly dispersive mode which extends up to 11 meV and an almost flat mode around 13 meV, which is different from the other two directions. This unique but simple dispersion gives us important information in identifying the ground state of the ordered phase of BaV₁₀O₁₅ which will be discussed in detail in the next section.

When the single crystal inelastic neutron scattering data measured using ARCS were loaded in powder mode in MSlice software, evidence for higher energy modes was observed. Thus, to get more information about a possible high energy magnetic excitation, inelastic neutron scattering experiment with incident energy of 120 meV was also performed using ARCS time of flight spectrometer. A broad but dispersionless excitation was observed centered around 33 meV along all three directions in reciprocal space as in Figure 3.7. The origin of this high energy excitation could be due to a broad spinwave excitation or due to singlet to triplet excitations from the trimer formation [50] of V2B, V3 and V3B ions.

In order to get more insight about the origin of the high energy excitation, temperature evolution was studied using an inelastic powder neutron scattering experiment using

MARI spectrometer at ISIS. The intensity contour map of the inelastic data measured on the powder sample BaV₁₀O₁₅ at different temperatures with incident neutron energy of 150 meV is shown in Figure 3.8 (a),(b) and (c). An anomalous excitation peak was observed only in the low Q region around 33 meV which started to become very weak only at temperatures close to $T_c=130$ K. Energy cuts to the contour map were obtained by integrating the data in the low Q region $0.8 \text{ \AA}^{-1} < Q < 2.5 \text{ \AA}^{-1}$ for temperatures from 5 K to 300 K and are shown in Figure 3.8 (d). The 33 meV peak is fitted with Lorentzian peak. At T = 75 K (to 300 K), an additional peak around 20-25 meV was needed to fit the data, indicating a movement of an excitation to lower energy with increasing temperature. A detailed analysis of the integrated intensity of the 33 meV mode will be discussed in the next section.

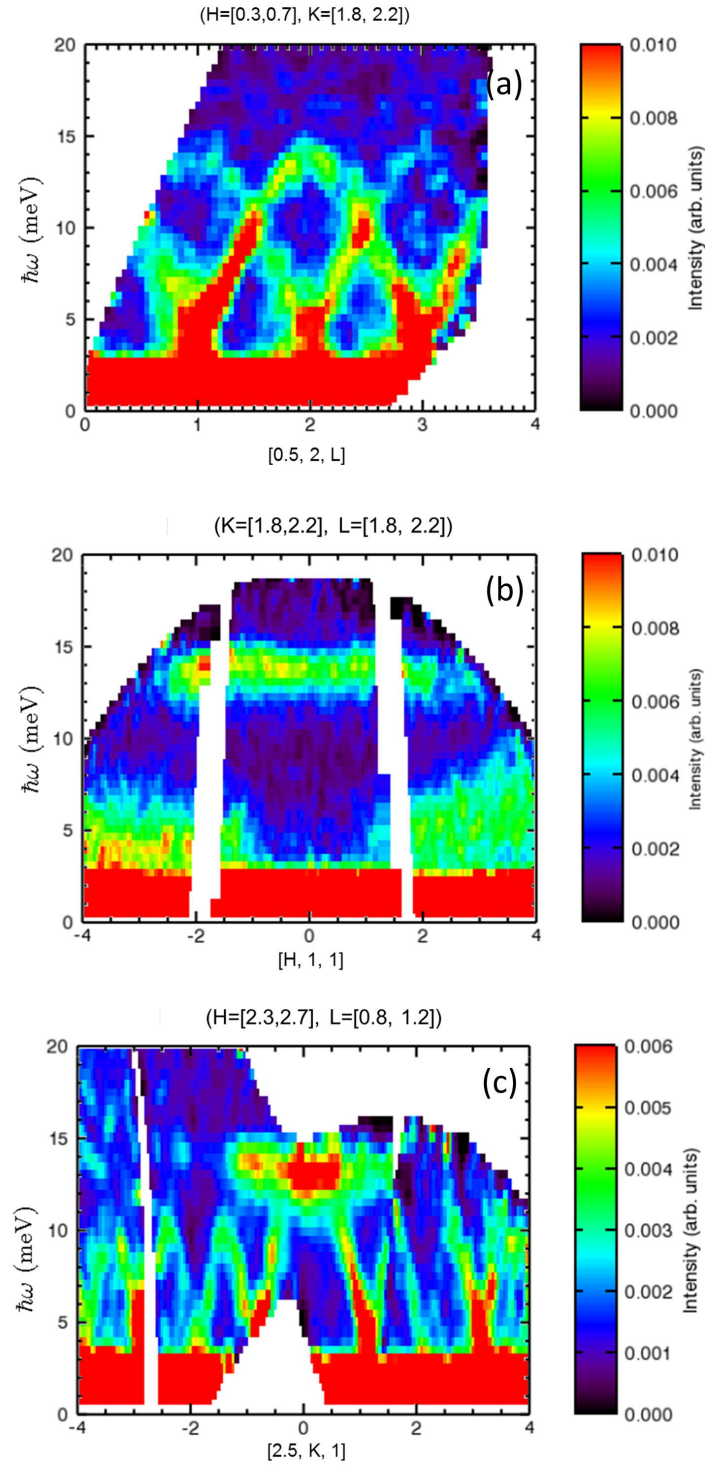


FIGURE 3.6: Time of flight inelastic neutron scattering data of BaV₁₀O₁₅ single crystal measured at ARCS spectrometer with incident neutron energy of $E_i = 65$ meV. Q -E maps, (a) $[0.5\ 2\ L]$ (b) $[H\ 1\ 1]$ (c) $[2.5\ K\ 1]$ directions

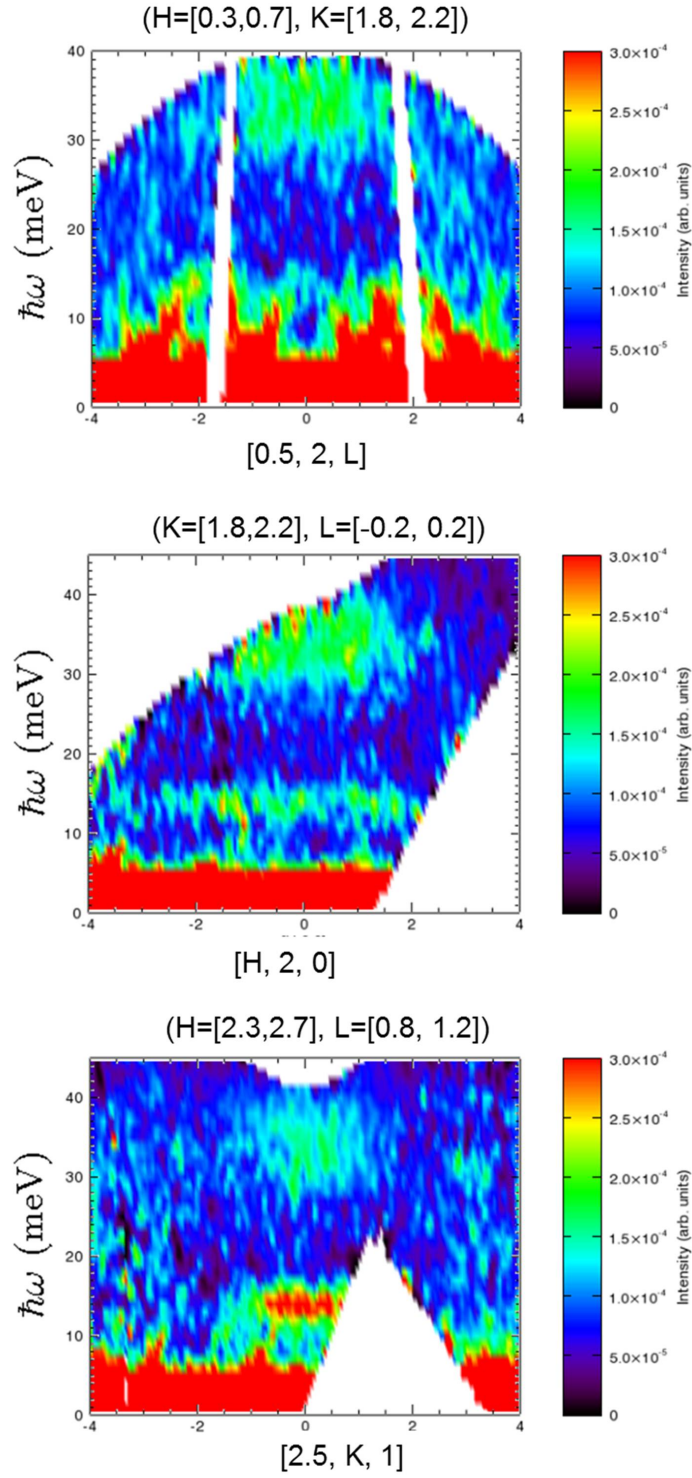


FIGURE 3.7: Time of flight inelastic neutron scattering data of BaV₁₀O₁₅ single crystal measured at ARCS spectrometer with incident neutron energy of $E_i = 120$ meV. Q - E maps, (a) [0.5 2 L] (b) [H 2 0] (c) [2.5 K 1] directions

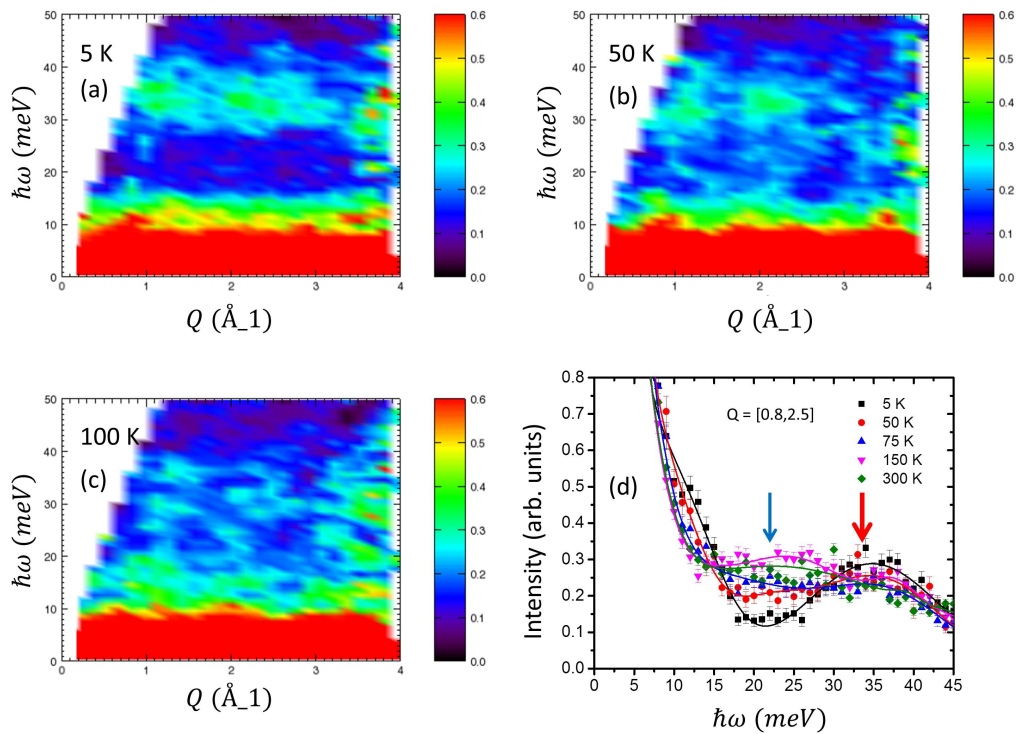


FIGURE 3.8: Time of flight inelastic neutron scattering data of $BaV_{10}O_{15}$ powder sample measured at MARI spectrometer at ISIS with incident neutron energy of $E_i = 150$ meV. $|Q$ -E maps, (a) 5 K (b) 50 K (c) 100 K. (d) Energy cuts of inelastic neutron scattering data for different temperatures integrated in low Q region $0.8 \text{ \AA}^{-1} < Q < 2.5 \text{ \AA}^{-1}$. Lines are the fitting for the data with multiple Lorentzian peak functions. Red arrow indicates the 33 meV peak position. Blue arrow indicates the additional peak around 20-25 meV that appear for $T \gtrsim 75K$

3.4 Determination of magnetic states of BaV₁₀O₁₅

3.4.1 Complexity of the system

Previous studies using different techniques have proposed formation of trimers by three out of five V ions forming a spin singlet state and the rest of the two V ions long range order below the transition temperature. However, the detailed low temperature magnetic structure had been unknown. In BaV₁₀O₁₅, V spins are arranged in a very frustrated unit. Consider the arrangement of V spins in the *ab* plane. As shown in Figure 3.1, it consists of a unit referred as "V-boat". Two V-boats at $z = 0$ and $z = 1/4$ layers are arranged 180° rotated with each other to form a highly frustrated bilayered cluster that repeats in *ab* plane in a systematic manner as shown in Figure 3.9 (a) and (b).

Each V ion in the cluster is surrounded by six oxygen ions that are octahedrally coordinated to form VO₆. These octahedra are edge shared with each other. Also within the cluster there are corner sharing bonds. These bilayers are then arranged in the z direction such that it is translated by (0.5 0.5 0) lattice units with the adjacent bilayer in the z direction and connected to each other with face sharing bonds (between green and dark green ions) as shown Figure 3.9 (c). Corner sharing bonding also exists between the bilayers (not shown for simplicity). Thus, this V spin system is arranged in a complex manner having three different kinds of bondings that we can see in an octahedrally coordinated system. An example for face, edge and corner sharing bondings are presented in Figure 3.9 (d) which shows only the V3 and V3B ions for clarity. The smallest repeating unit is shown in Figure 3.9 (e) which consists of triangles, tetrahedra and pyramids like units which are highly frustrated.

BaV₁₀O₁₅ has both charge and orbital degrees of freedom. Nominally four out of five V ions are V³⁺ ($3d^2$) and one is V²⁺ ($3d^3$). V³⁺ ($3d^2$) ions have orbital degrees of freedom where the two electrons can occupy any two t_{2g} orbitals out of d_{xy} , d_{yz} and d_{zx} orbitals. Thus, combining both charge and orbital degrees of freedom and assuming similar ions occupy same orbitals (e.g. all V1 - d_{xy}), we have 405 possible orbital states to consider.

The magnetic diffraction peaks observed from the long range ordering below $T_N = 43$ K are weak and limited. The system contains 80 magnetic ions in the unit cell. Thus, considering all the points discussed here, finding out the ground state of the system in BaV₁₀O₁₅ is a very challenging task. In the next sections, an approach to find a spin model and an orbital model that can reasonably represent both powder diffraction and inelastic neutron scattering data that we measured will be discussed.

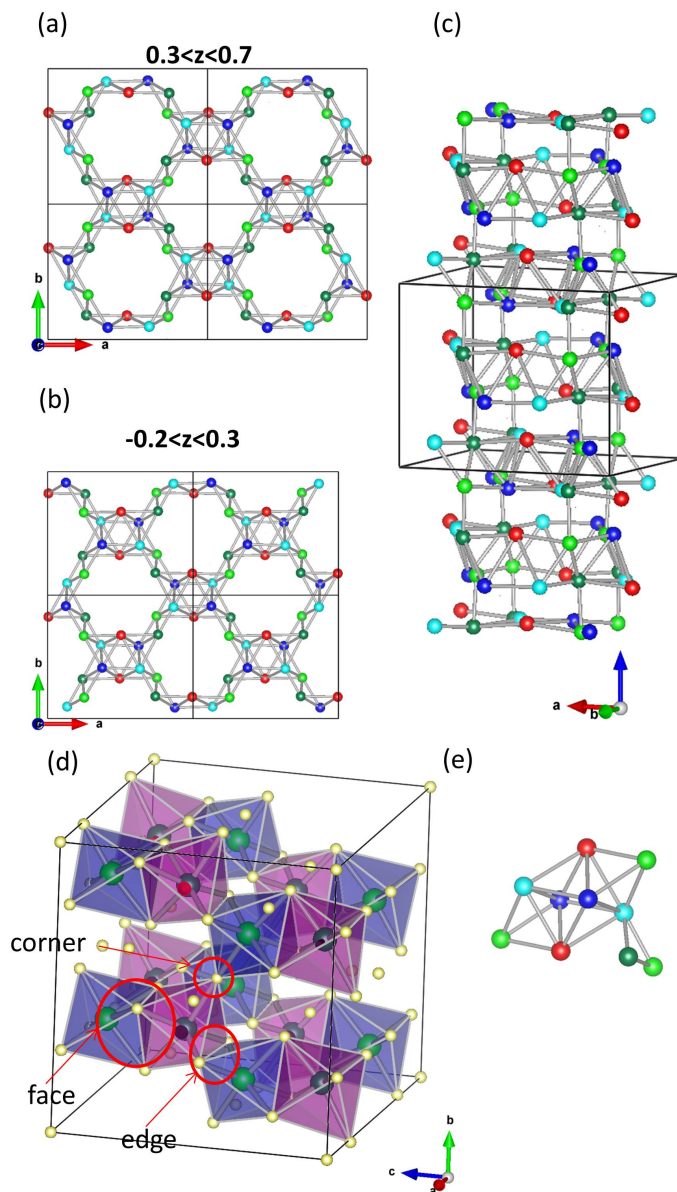


FIGURE 3.9: Arrangement of V spins and different types of interactions in BaV₁₀O₁₅ (a),(b) "Boat" like structure in the *ab* plane in different layers. (c) connection between the layers consisting of array of V boats. (d) Example of different types of interactions in BaV₁₀O₁₅, face, edge and corner sharing bonds. Only V3 (dark green) and V3B (green) ions are shown. (e) Highly frustrated unit, V boat.

3.4.2 Systematic approach to find the magnetic state

As discussed in previous sections, BaV₁₀O₁₅ undergoes a structural phase transition from *Cmca* to *Pbca* symmetry at $T_s = 130$ K and upon further cooling, the system long range orders with an easy axis along *a* direction. There have not been many studies to find the magnetic structure of this system, possibly due to its complexity in the arrangement of V ions. A previous attempt to find the magnetic structure is reported in reference [49] as shown in Figure 3.10. They report that all five V ions order in this system giving rise to a complex magnetic structure. But the exact spin orientation of the magnetic structure is not reported. Thus, the low temperature magnetic structure of this system had been unknown.

Usual procedure to determine the magnetic structure is to perform group theoretical calculations and the refinement is performed carrying out all the possibilities of the basis vectors to generate the magnetic structure of the system. As discussed in the previous section, propagation vector of the magnetic ordering of BaV₁₀O₁₅ is $k = (0.5 \ 0 \ 0)$. The calculation of basis vectors using group theoretical methods were carried out using version 2 K of the program SARA h -Representational Analysis[35]. The magnetic representation of a crystallographic site can then be decomposed in terms of the irreducible representations (IRs) of $G_{\mathbf{k}}$ (space group symmetry elements, g , that leave the propagation vector \mathbf{k} invariant):

$$\Gamma_{Mag} = \sum_{\nu} n_{\nu} \Gamma_{\nu}^{\mu} \quad (3.1)$$

where n_{ν} is the number of times that the IR Γ_{ν} of order μ appears in the magnetic representation for the chosen crystallographic site.

In the present system, the crystal structure of BaV₁₀O₁₅ before the magnetic phase transition can be reproduced by the space group *Pbca* (#61). This space group involves 1 centering operation and 8 symmetry operations. These 8 symmetry operations leave the propagation \mathbf{k} invariant or transform it into an equivalent vector.

The decomposition of the magnetic representation Γ_{Mag} in terms of the non-zero IRs of $G_{\mathbf{k}}$ for each crystallographic site is examined, and their associated basis vectors, ψ_n , are given in Table 3.3.

There are 5 crystallographic sites which we name as V1, V2, V2B, V3 and V3B. For each site, there are 8 equivalent positions leaving 40 V ions in the crystallographic unit cell. Magnetic unit cell doubles along *a* direction leading to 80 magnetic atoms in the magnetic unit cell. Basis vectors for each equivalent positions are as in Table 3.3. The

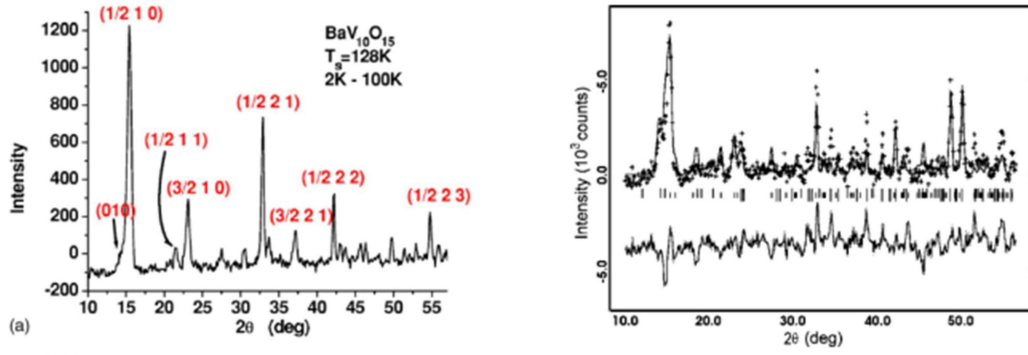


FIGURE 3.10: Previous neutron powder diffraction data and refinement as in reference [49] (a) Difference plots 2 K - 100 K for BaV₁₀O₁₅, $T_s = 128$ K (b) Refinement of the neutron diffraction data.

magnetic representation $\Gamma_{Mag} = 6\Gamma_1^2 + 6\Gamma_2^2$. Both Γ_1 and Γ_2 are two dimensional, thus for each irreducible representation there are 12 basis vectors. Magnetic moment of each V ion is a linear combination of the basis vectors. Looking at the Table 3.3, we need at least two basis vectors to order all equivalent positions in one direction. Thus to represent a 3 - dimensional spin direction we need at least 6 basis vectors in total. Carrying out all the possibilities to select the symmetry allowed magnetic structures is a very difficult task due to the enormous number of possible combinations exist. And it becomes more difficult when a limited number of magnetic peaks are observed and their intensities are very small, almost hiding in the background. Thus, we need the information from other techniques to simplify the problem. Inelastic neutron scattering data provide very useful information about the possible spin structure of the system.

Going back to the Figure 3.6, we observe these features in the dispersion of the spinwave modes.

1. **Highly dispersive mode along L direction.** : To have a dispersive mode along L-direction, V ions should be connected in the c-direction by one of the three possibilities. i.e. Face, edge or corner sharing bonding.
2. **Flat mode along H direction.** : Dispersionless mode is observed along a particular direction in reciprocal space when ions are disconnected along that corresponding direction in real space. Thus, along *a*-direction there should be little to no interaction/connection between V ions.

Figure 3.11 (a) shows V ions in the bilayered cluster at $-0.2 < z < 0.3$ and edge sharing bonds between them. Bond lengths vary from 2.52 Å to 3.14 Å, which is the important factor to determine the relative strength of the interaction due to the orbital

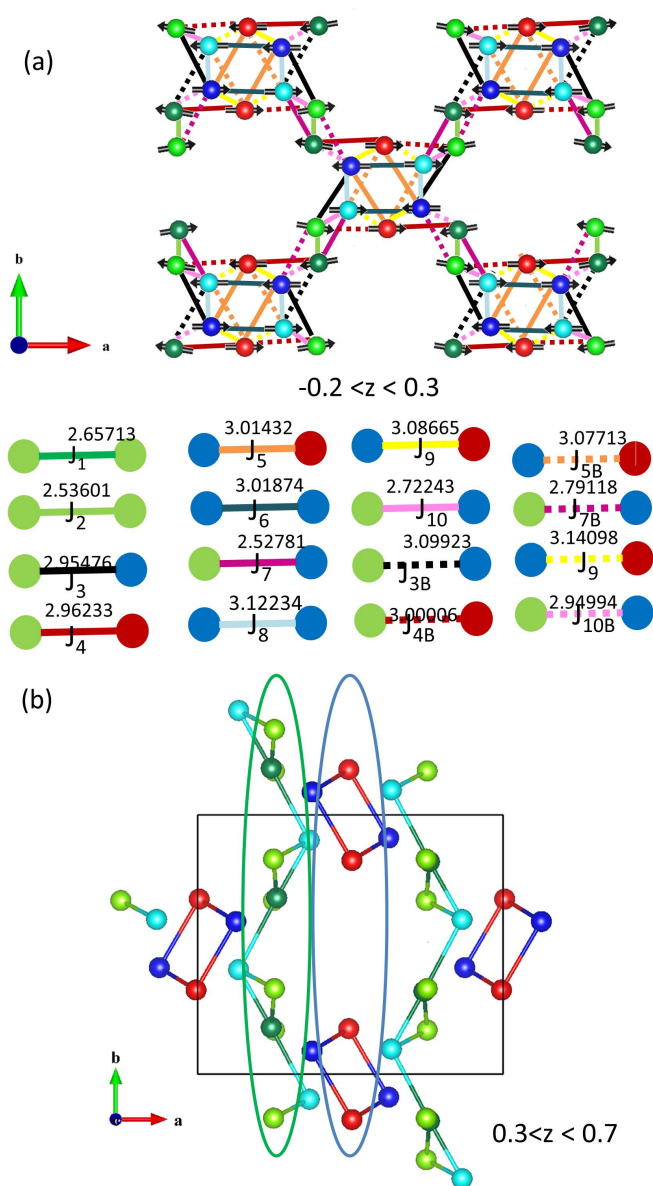


FIGURE 3.11: (a) Arrangement of V ions in the ab plane with $-0.2 < z < 0.3$ and the edge sharing and face sharing bonds of $BaV_{10}O_{15}$ in that plane with the corresponding bond lengths (b) Example of how the connection along a direction can be broken. The V ions here are in the plane $0.3 < z < 0.7$

overlap. When all five V ions are ordered, the system is highly frustrated and spinwave dispersions are not stable, as we will discuss later in this chapter.

The dispersionless mode along H direction can be achieved in different ways. If only V1 (red) and V2 (blue) ions are ordered then the ordered V ions are disconnected along a direction as shown in Figure 3.11 (b) but connected along c direction by corner sharing bonding (not shown). The second way is when only V2B (sky blue), V3 (dark green) and V3B (green) are ordered below T_N . As in Figure 3.11 (b), this also makes the disconnected arrangement of ordered V ions in a direction, but connected along c direction by face sharing bonding (not shown).

Thus, we consider our analysis in three different ways.

1. Only V1 and V2 ions order below T_N .
2. Only V3 , V2B and V3B ions order below T_N .
3. All 5, V ions order below T_N .

For the simplicity, first we consider collinear magnetic structures for each category presented above. When only V1 and V2 ions are ordered, we can consider a unit where V1 and V2 ions form a pseudo-square and these pseudo-squares are arranged in space such that they are connected to each other by a corner sharing bond in c -direction with the adjacent pseudo-square in the other plane . When we consider one pseudo-square and adjacent V ions to each ion in the pseudo-square, there are only 8 possible arrangements of V spins as shown in Figure 3.12. The second type, with only V3 , V2B and V3B ions ordering below T_N , has several possible arrangements of spins. Few selected magnetic structures out of the possibilities are presented in Figure 3.13. In these spin structures V3 , V2B and V3B ions form triangles which are connected along b (edge shared bond) and c (face shared bond) directions. These arrangements of spins are frustrated. An unfrustrated model with 120° arrangement of spins is not allowed due to symmetry.

To find the magnetic structure that can explain our neutron powder diffraction data in Figure 3.5, relieved refinements were performed. Many possible magnetic structures were investigated following the basis vectors presented in Table 3.3 and here few examples of the refinements for each category will be presented.

Since the magnetic peaks are almost hidden in the background, the difference of the neutron powder diffraction data at 4 K and 100 K are used in the refinement, which show only the magnetic contribution of NPD pattern. Data are carefully rebinned to reduce the noise. Since the background becomes negative, a constant value is added to the data for refinement purposes in Fullprof.

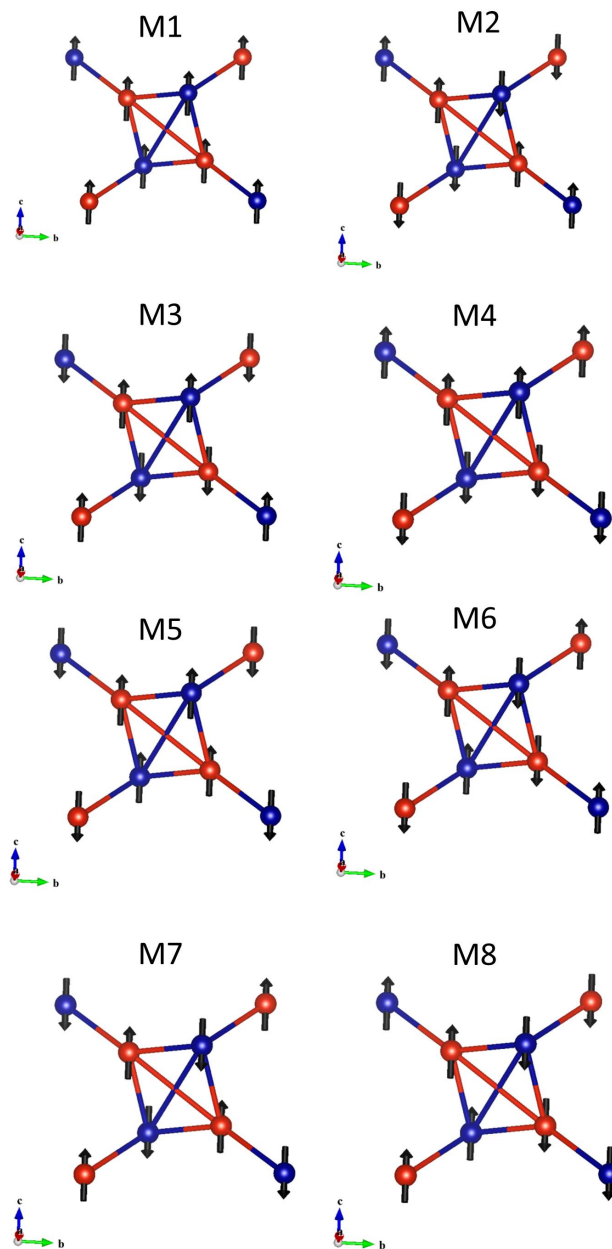


FIGURE 3.12: Possible magnetic structures with only V1 and V2 ions ordered below T_N of BaV₁₀O₁₅

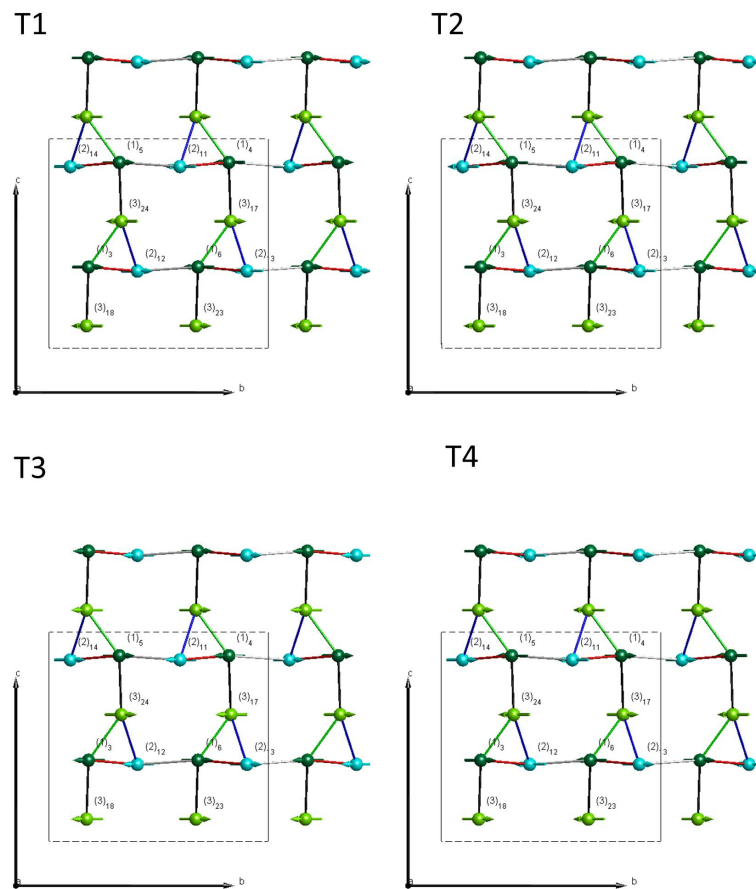


FIGURE 3.13: Few examples of possible magnetic structures with only V2B, V3 and V3B ions ordered below T_N of BaV₁₀O₁₅

TABLE 3.2: Refined magnetic moments of V1 and V2 ions for the model M8.

	m_a (μ_B)	m_b (μ_B)	m_c (μ_B)	$\langle m \rangle$ (μ_B)
V1	0.884 ± 0.250	0	0.259 ± 0.051	0.921 ± 0.255
V2	1.002 ± 0.189	0	0.194 ± 0.062	1.021 ± 0.199

Figure 3.14 shows the refinement results for selected models with only V1 and V2 atoms ordered. The Model M8 gives a reasonably good fitting for the data, while other models could not produce relative intensities of the main magnetic peaks. Ordered moment of the V1 and V2 ions are $0.9(2) \mu_B$ and $1.0(2) \mu_B$ respectively which is smaller than the fully ordered moment expected for $S=1$ ($2 \mu_B$) or $S=3/2$ ($2 \mu_B$). In this model four V ions in the pseudo-square are frustrated. The unfrustrated spin configuration model M7, cannot produce the main diffraction peak intensity.

The possibility of only V2B, V3 and V3B ions ordered is also investigated and the best fit out of different possibilities is shown in 3.15 (a). Although the main magnetic peak (0.5 1 0) is fitted well with this model, the intensity of (0.5 2 1) peak is zero. We also considered the third category where all the spins are ordered. The best refinement when all five atoms are ordered is shown in Figure 3.15 (b), which fits the NPD data well. This model also has some similarity with model M8, where the all/part of pseudo-squares formed by V1 and V2 ions are frustrated. Infact it is found that when a frustrated model for V1 and V2 ions are arranged in the pseudo-square, the refinement gives us a better fitting compared to other models.

Thus, by using systematic approach for the magnetic structure refinement we narrowed down the number of possibilities for the low temperature spin structure. The possible models are further tested with our inelastic neutron scattering (INS) data to find out the best model and Hamiltonian that can describe both NPD and INS data qualitatively.

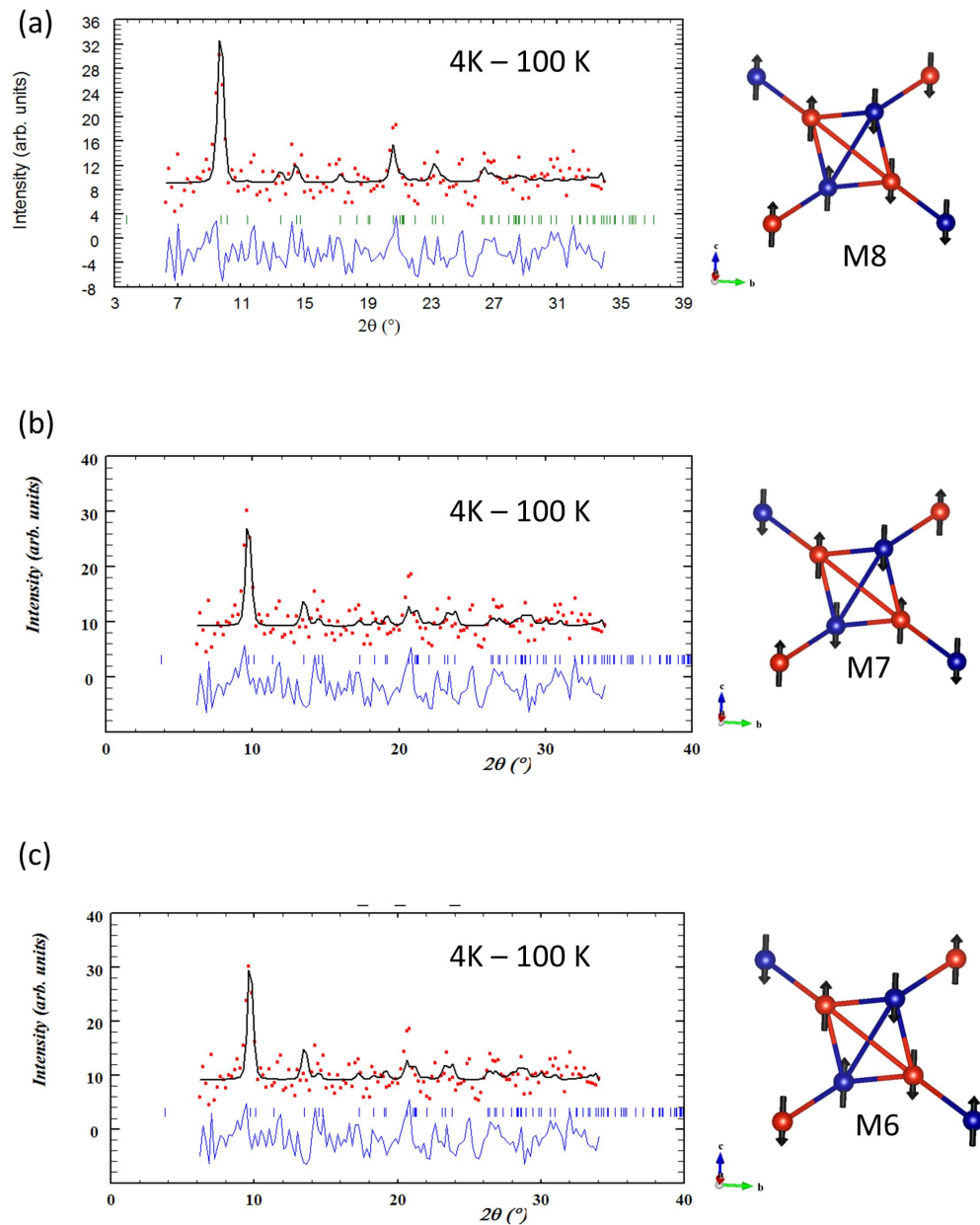


FIGURE 3.14: Refinement of NPD data Possible magnetic structures with only V1 and V2 ions ordered below T_N of $BaV_{10}O_{15}$ (a) M8 model (b) M7 model (c) M6 model

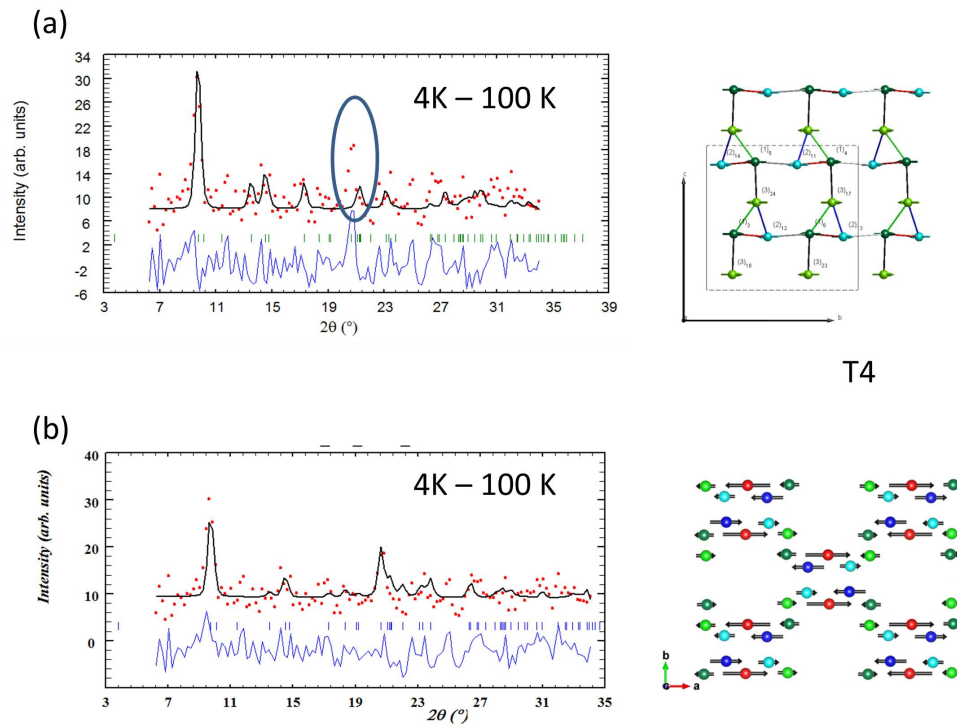


FIGURE 3.15: Refinement of NPD data of possible magnetic structures with (a) only V2B, V3 and V3B ions ordered below T_N of $BaV_{10}O_{15}$ (b) all five V atoms are ordered

3.4.3 Simulation of magnetic excitations : Linear spinwave calculations

In order to understand the nature of magnetic excitations and coupling between spin, charge and orbital degrees of freedom, linear spinwave calculations were performed.

Following Heisenberg spin Hamiltonian was used to calculate and model the spinwave dispersion and intensities,

$$\mathcal{H} = \sum_{\langle ij \rangle} J_{ij} \vec{S}_i \cdot \vec{S}_j \quad (3.2)$$

J_{ij} is the nearest neighbor interaction between the magnetic ions. The number of nearest neighbor interactions changes from model to model.

For the intensity calculation of the spinwave modes, SpinW program [39] was used and resulting contour map was convoluted with experimental energy resolution for ARCS spectrometer with $E_i = 65$ meV for energy transfer below 20 meV and with $E_i = 120$ meV greater than 20 meV energy transfer.

Different spin structures presented in the previous section were considered. First when only V2B, V3 and V3B ions are ordered, linear spinwave calculations were performed and the closest result for the observed data was produced by model T1 as in Figure 3.16. In this, J_4 exchange interaction which connects V3 and V3B ions with a face sharing bond is the largest with 40 meV. The low energy dispersion along L direction matches well but the high energy excitations around 40 meV are the strongest which contradict with the experimentally observed magnetic excitations. Also, the refinement of neutron powder diffraction data using this spin configuration does not produce a good fitting.

Secondly, the linear spinwave calculation for the spin configuration proposed previously in the reference [52] is presented. Here, V1 and V2 ions form a tetramer or pseudo-square where all the bonds between V1 and V2 are satisfied with antiferromagnetic coupling. V1-V2 pseudo-squares in the ab plane are connected by corner sharing bonds to the other layer. This model can also produce some of the main features in our neutron scattering data. But the number of spinwave modes is different from the observed excitations. Along K direction, the calculation produces three spinwave modes but our data only have two modes. Additionally, this model also failed to give a good fitting for the NPD data.

The linear spinwave simulation when all five atoms are ordered was also investigated, for example, for the spin structure in Figure 3.15 (b). However, it fails to stabilize the

calculated spinwave dispersions giving imaginary modes and even the qualitative picture of the observed dispersion was hard to reproduce with such a magnetic structure.

The best fit for the inelastic neutron scattering data was obtained by simulation of the spinwave excitations using the model M8. The calculated contour map of inelastic scattering cross section is shown in Figure 3.18. The exchange constant for the simulation is summarized as in Table 3.4. Due to the possible charge ordering of the system there can be two situations for the spin value, S of V1 and V2 and parameters for both possibilities are presented. According to this model, antiferromagnetic interaction J_1 which is mainly along b direction is the strongest. J_2 is small compared to J_1 . Corner sharing interactions J_4 and J_5 which have 180° V-O-V bond angle is also antiferromagnetic and almost half of J_1 . For the propagation of a spinwave mode, J_3 interaction which is from a corner sharing bond but with 120° V-O-V bond angle, needs to be ferromagnetic. As can be seen in the simulation, the spinwave dispersions and the intensity below 20 meV match quite well. Also, as discussed in the previous section, neutron powder diffraction refinement of this model (Figure 3.14 (a)) agrees with the data well. Thus, the best model for the low temperature magnetic structure considering simulation for both NPD and INS data, is when only V1 and V2 atoms are ordered and the spin directions are as in model M8 in Figure 3.12. The values of the exchange constants in light of possible orbital ordering of the system will be discussed in a later section. Interestingly, the observed and calculated spinwave models have additional modes around 30 meV, which are in the same energy range as the broad excitation observed in our INS experiment at ARCS spectrometer with $E_i = 120$ meV.

TABLE 3.4: Exchange constants used for each spinwave model in figure 3.18 (model M8) for the Hamiltonian in equation 3.2

	J_1 (meV)	J_2 (meV)	J_3 (meV)	J_4 (meV)	J_5 (meV)
$S_{V1} = 1, S_{V2} = 1$	13.2	2.8	-6.2	5.8	5.6
$S_{V1} = 3/2, S_{V2} = 1$	14	2.9	-8	7	7

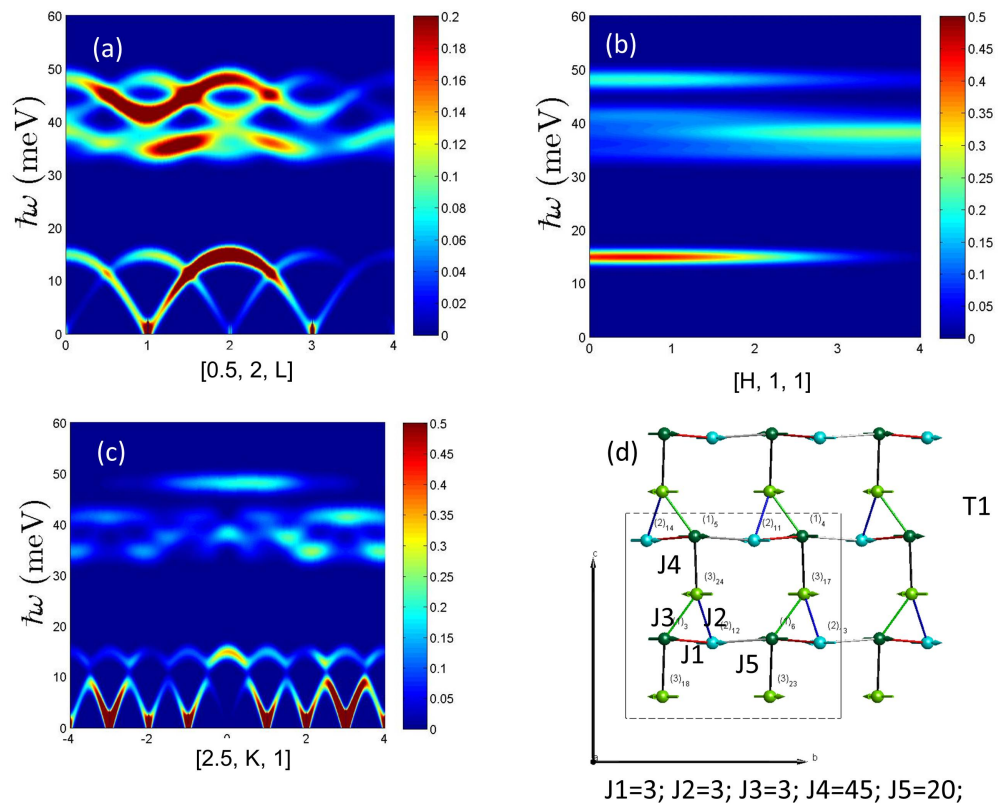


FIGURE 3.16: Linear spinwave calculation for Model T1 as in Figure 3.13 of BaV₁₀O₁₅. Along (a) (0.5 2 L) (b) (H 1 1) (c) (2.5 K 1). (d) Magnetic structure and exchange constants

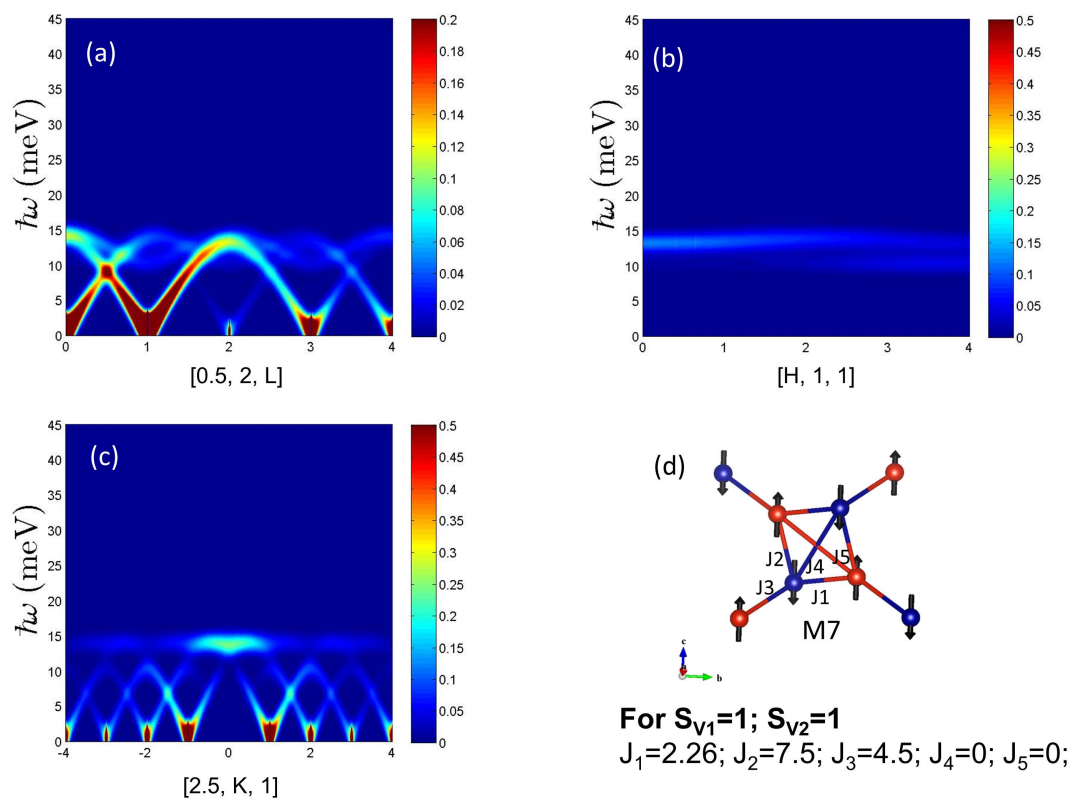


FIGURE 3.17: Linear spinwave calculation for Model M7 as in Figure 3.12 of BaV₁₀O₁₅ along (a) (0.5 2 L) (b) (H 1 1) (c) (2.5 K 1). (d) Magnetic structure and exchange constants

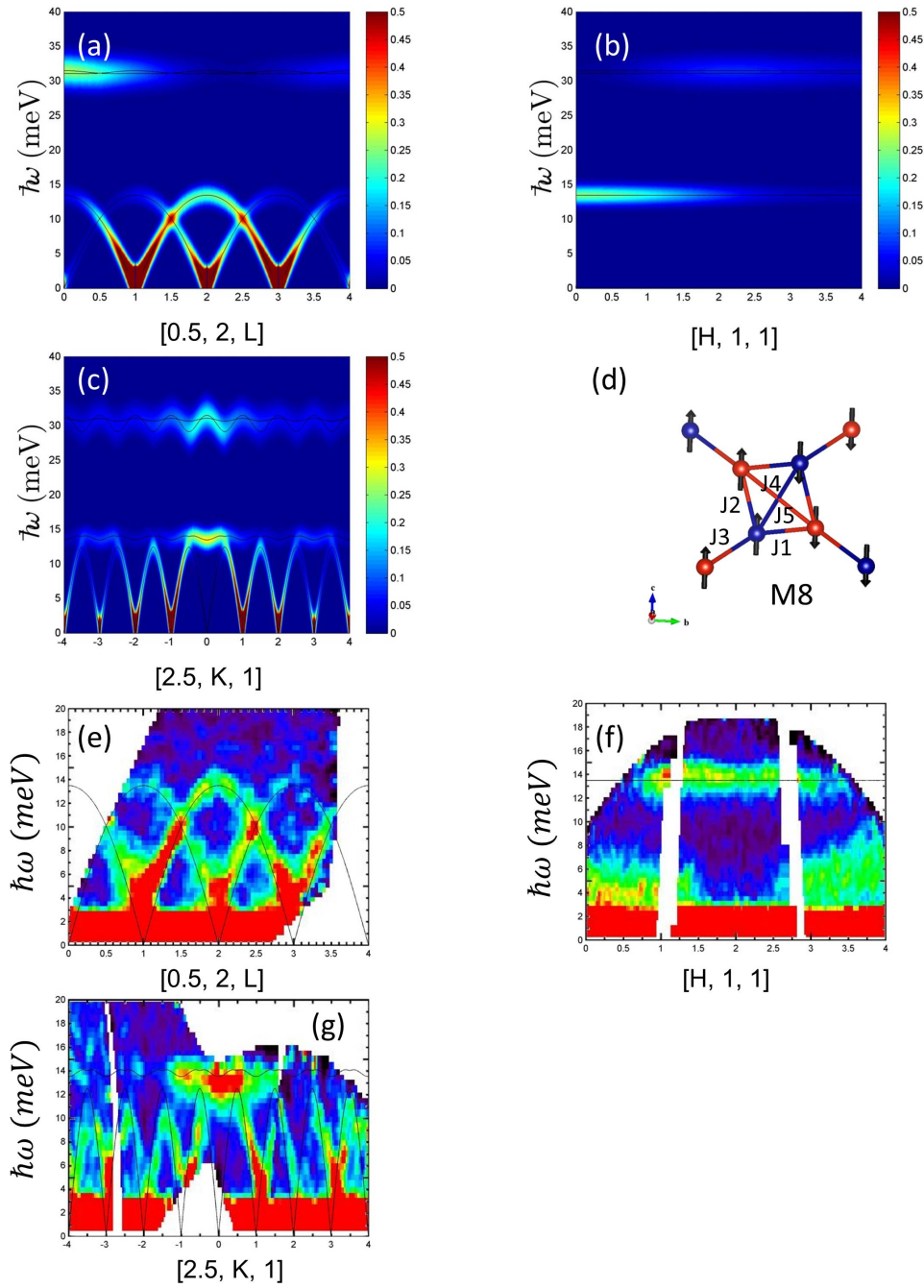


FIGURE 3.18: Linear spinwave calculation for Model M8 as in Figure 3.12 of $BaV_{10}O_{15}$ along (a) $(0.5, 2, L)$ (b) $(H, 1, 1)$ (c) $(2.5, K, 1)$, (d) Magnetic structure (e), (f), (g) Calculated spinwave dispersions for Model M8 superimposed on top of the inelastic neutron scattering data measured using single crystal of $BaV_{10}O_{15}$ at ARCS time of flight spectrometer

3.4.4 Temperature dependence of higher energy magnetic excitation

In order to study the temperature evolution of the magnetic excitations that is observed around 33 meV, the time of flight inelastic neutron scattering measurements of BaV₁₀O₁₅ powder sample were performed at MARI spectrometer at ISIS with incident neutron energy of $E_i = 150$ meV.

$|Q|$ -E maps at 5 K, 50 K, 100 K and the energy cuts of inelastic neutron scattering data for different temperatures integrated in low Q region $0.8 \text{ \AA}^{-1} < Q < 2.5 \text{ \AA}^{-1}$ are shown in Figure 3.8. The energy cuts were fitted with multiple Lorentzian peak functions,

$$I(\omega) = I(0) \frac{\kappa^2}{\kappa^2 + \omega^2} \quad (3.3)$$

From the fitting, few important features were observed. The broad peak at 33 meV can be fitted with one Lorentzian peak along with the peaks corresponding to low energy excitations below 20 meV. Upon warming at $T = 75$ K ($T > T_N$), an additional peak around 20 - 25 meV appears. This may indicate that part of the excitation at 33 meV moves to lower energy which will eventually become quasi elastic with further increase in temperature. However, clearly, 33 meV mode is still visible for $T > 75$ K with less intensity and becomes almost zero around 150 K. The temperature dependence of the integrated intensity of the 33 meV peak is extracted from the fitting as shown in Figure 3.19.

It is previously proposed that with large contraction of V-V bonds between V2B, V3 and V3B ions form a trimer in a cooperative paramagnetic phase.

For spins arranged in a triangle, the Hamiltonian with Heisenberg exchange interactions is,

$$\mathcal{H} = J_1 \vec{S}_1 \cdot \vec{S}_2 + J_2 \vec{S}_2 \cdot \vec{S}_3 + J_3 \vec{S}_3 \cdot \vec{S}_1 \quad (3.4)$$

For simplicity we consider $J_1 = J_2 = J_3 = J$. Because of possible charge ordering in this mixed valence system with one out of five vanadium ions is $S = 3/2$ and others are $S = 1$, there will be two scenarios, i.e. $S_1 = S_2 = S_3 = 1$ and $S_1 = S_2 = S_3 = 3/2$. The ground state energy for each case is,

$$E = \left(\frac{1}{2}S(S+1) - 3\right)J ; S_1 = S_2 = S_3 = 1 \quad (3.5)$$

$$E = \left(\frac{1}{2}S(S+1) - 31/8\right)J ; S_1 = S_2 = 1 \text{ and } S_3 = 3/2 \quad (3.6)$$

Energy level diagram for both cases are shown in Figure 3.19.

The differential magnetic neutron cross section for inelastic transitions $|S_i\rangle \rightarrow |S_f\rangle$ is [59, 60],

$$\begin{aligned} \frac{d^2\sigma}{d\Omega_f dE_f} = C_0 \rho(S, T) \sum_{\alpha\beta} (\delta_{\alpha\beta} - \hat{Q}_\alpha \hat{Q}_\beta) \times \sum_{jj'} \exp[i\mathbf{Q}\cdot(\mathbf{R}_j - \mathbf{R}_{j'})] \times \\ \sum_{MM'} \langle SM | \hat{S}_j^\alpha | S'M' \rangle \langle S'M' | \hat{S}_j^\beta | SM \rangle \times \delta(\hbar\omega + E(S) - E(S')) \end{aligned} \quad (3.7)$$

where

$$C_0 = N \frac{k'}{k} \left(\frac{\gamma e^2}{m_e c^2} \right)^2 F^2(\mathbf{Q}) \exp[-2W(\mathbf{Q})] \quad (3.8)$$

$$\rho(S, T) = Z^{-1} \exp \left[\frac{-E(S)}{K_B T} \right] \quad (3.9)$$

$Q = k - k'$ is the scattering vector and Q is the magnetic form factor. Z is the partition function.

Thus, the neutron scattering intensity $I(T)$, as a function of temperature for an inelastic transition from a particular spin state to another can be written as,

$$I(T) \propto Z^{-1} \exp \left[\frac{-E(S)}{K_B T} \right] \quad (3.10)$$

The observed integrated intensity of the 33 meV excitation is fitted with equation 3.10. The transition from the ground state to the first excited state is considered as it is the strongest excitation that can be observed with inelastic neutron scattering. By fitting, the exchange constant J value is obtained which is 14(1) meV for $S_1 = S_2 = S_3 = 1$

and 12(2) meV for $S_1 = S_2 = S_3 = 3/2$. These fitted J values are much lower than the expected J values (33 meV and 22 meV respectively) for the excitation from ground state to the first excited state. Although the shape of the temperature dependence has a similar behavior, it does not match exactly with the expected intensity. From the fitting of the energy cuts, we found that an additional peak was observed for $T > 75$ K around 20-25 meV. Thus, it is possible that the broad excitation around 33 meV mode is due to ground state to excited state excitation from the Trimer (V2B, V3 and V3B ions) plus the contribution from the spinwave excitation from V1 and V2 ions in the ordered phase. Although that can be a possible scenario for this system from the available data and simulation, the determination of exact contribution to the intensity to the spinwave mode is difficult to extract from the currently available data. In fact if the contribution for the higher energy excitation from the trimer excitation is half of what is observed for $T < 75$ K, then the temperature dependence of the intensity matches better with the trimer excitation with $J = 33$ meV (or $J = 22$ meV).

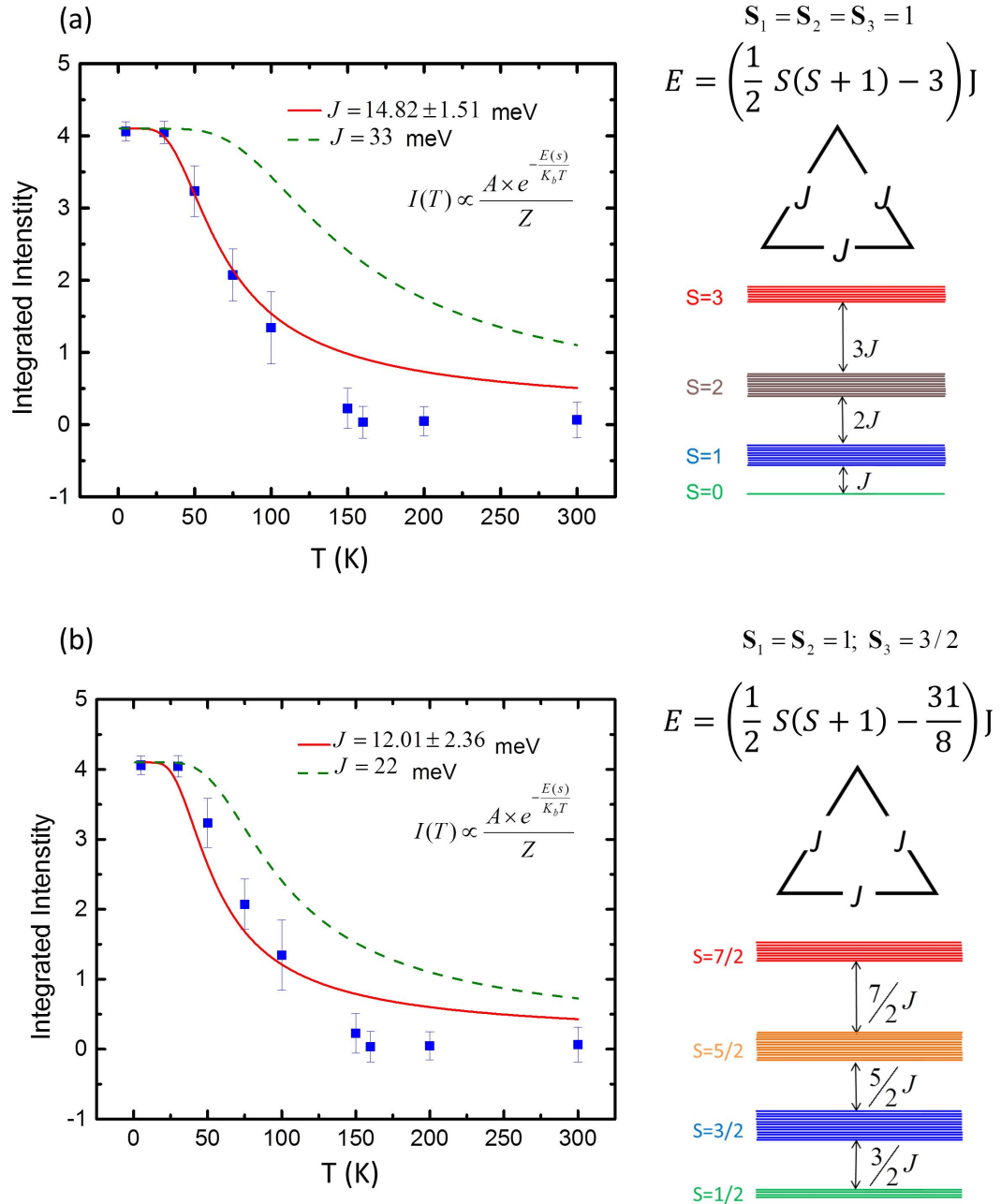


FIGURE 3.19: Temperature dependence 33 meV excitation measured using powder inelastic neutron scattering experiment of $\text{BaV}_{10}\text{O}_{15}$ using MARI spectrometer at ISIS (a) Fitting assuming $S_1 = 1, S_2 = 1, S_3 = 1$ (b) Fitting assuming $S_1 = 1, S_2 = 1, S_3 = 3/2$

3.5 Possible orbital ordering of BaV₁₀O₁₅

BaV₁₀O₁₅ nominally consists of four out of five V ions with 3+ (t_{2g}^2 , S=1) and one 2+ (t_{2g}^2 , S=3/2) ion. V³⁺ ions are orbitally active. All the V ions are in an octahedral ligand field. Thus t_{2g} orbitals have the lower energy and V³⁺ ions are orbitally degenerate, where it can pick two out of the three possible t_{2g}^2 orbitals, namely d_{xy} , d_{yz} and d_{zx} . As discussed before, when the octahedron becomes distorted, an orbital ordering can occur by lifting the degeneracy. Let's consider the best fit magnetic structure model M8, that we discussed earlier. According to the model, only V1 and V2 ions are long range ordered and other three ions do not order below T_N .

Let's first look at the possible orbital model considering only V1 and V2 ions. The Figure 3.20 shows some possible orbital configurations for V1 and V2 ions. When $S_{V1} = S_{V2} = 1$, four different possibilities are presented. The distortion of the octahedral environment of ligand field is different from ion to ion. For example, the ligand field of V1 and V2 ions are presented in Figure 3.21 (b). Both V1 and V2 ions are surrounded by six oxygen ions in a distorted octahedra with different ligand bond lengths. Typically if a ligand bond is larger along one direction, then, the repulsion between metal ion and ligand (or cation and anion) are lowest along that direction. Thus the orbitals corresponding to that particular direction will have lower energies. In our case, six different ligand bonds exist, thus a straight forward interpretation of which orbital favors is a question. But to get an idea, we consider the average bond lengths along x , y and z directions, which are shown in Figure 3.21 (b). For both V1 and V2, the average ligand bond with V ion is largest along x direction and smallest along z direction. Thus, it can be reasonably assume that the d_{xy} orbital is occupied in both V1 and V2. This also agrees with the spin Hamiltonian presented for spinwave model M8 in the previous section.

In all the orbital diagrams in Figure 3.20, d_{xy} orbitals are occupied by one electron and for first four models, the other electron is occupied by either d_{yz} or d_{zx} orbitals. The last two orbital models are when one of the V ions out of V1 and V2 is 3+ (S=3/2), thus there is no orbital degeneracy.

In the spin Hamiltonian that describes our inelastic neutron scattering data, J_1 antiferromagnetic interaction is the strongest and J_2 antiferromagnetic interaction is much weaker. According to the above orbital models, when d_{xy} orbital is occupied in both V1 and V2, there can be a direct overlapping between the orbitals along the directions of both J_1 and J_2 . However, we also need to consider the V-V bond length to get an estimate of the relative strength. It is well known that the edge sharing bonds with the nearby octahedron are very sensitive to its bond length. A system can have a critical bond length (cation-cation separation), R_c and when the bond length is greater than

R_c , cation-cation interaction is considered as "weak" and as "strong" when smaller than R_c [61]. This type of short (strong) and long (weak) bonds are previously observed in ZnCr₂O₄, where the difference between the long and short bonds are approximately 0.01 Å to 0.02 Å. In BaV₁₀O₁₅, the bond length corresponding to J_1 and J_2 interactions are 3.014 Å and 3.087 Å respectively. Thus, this difference in bond length is considerable and in comparison to ZnCr₂O₄ the difference is 3-4 times larger. Thus, our spin Hamiltonian with $J_1 > J_2$ (antiferromagnetic) is valid and a probable case for this system.

On the other hand, J_3 , J_4 and J_5 interactions are cation-anion-cation interactions where they share common corners with near by octahedra. The cation-anion-cation interactions are optimal when the angle between cation-anion-cation (V-O-V) is 180° as in the case of J_4 and J_5 in our spin model. Thus, an antiferromagnetic interaction which is relatively smaller than the edge shared J_1 , cation-cation interaction is expected as in our best fit Hamiltonian. J_3 interactions also involve corner sharing bonding with V-O-V angle of 122°. When the angle between cation-anion-cation is around 90°, the interaction is found to be ferromagnetic as we discussed in Chapter 1. But it changes from ferromagnetic to antiferromagnetic when the angle increases at a specific value. Two possible orbital arrangement for V1 and V2 ions with the p orbitals of oxygen ion is shown in Figure 3.22(b). If the p orbitals are selected such that creating a π bond with V1 ions, then, considering the occupation of orbitals in the V2 ions, there is a possibility of bonding with a different p orbital than the previous, which can lead to ferromagnetic interaction. The other possibility is the interaction through double exchange process of this possible mixed valence arrangement of V1 and V2 ions with 2+ and 3+ oxidization states(or reverse). In mixed valence systems with Mn⁴⁺ and Mn³⁺ ions, ferromagnetic interactions had been previously observed [19, 20]. However, the reason for the ferromagnetic interaction J_3 is yet to be understood. Theoretical calculations involving the distortions and relative orientations of the octahedra need to be considered to understand the ferromagnetic nature of the J_3 interaction.

As previously proposed [50], the other three ions V2B, V3 and V3B are probably in a spin singlet state with $S = 1$. As shown in Figure 3.22, the V-V bond length are much smaller (0.5 to 0.7 Å) than the V-V bonds between V1 and V2. Thus the exchange interaction between these ions will be much larger than J_1 (~ 13 meV) in our spinwave model. And it is quite possible that the intra trimer interactions are in the order of 30 meV in this system, giving rise to the 33 meV excitation observed, from singlet to triplet excitation. The orbital configuration considering all the results are as shown in Figure 3.21 (a), where we have drawn the trimer and non-trimer V ions separately for clarity.

To identify whether the higher energy excitations are due to both magnons and singlet to triplet excitation, single crystal inelastic neutron scattering experiment at higher

temperatures such as $T = 75$ K and $T = 150$ K could be performed, which remain as a future plan. Also, the analysis did not consider the superexchange interactions between the pseudo-squares via spin singlet state, which can slightly modify the calculated excitation spectrum.

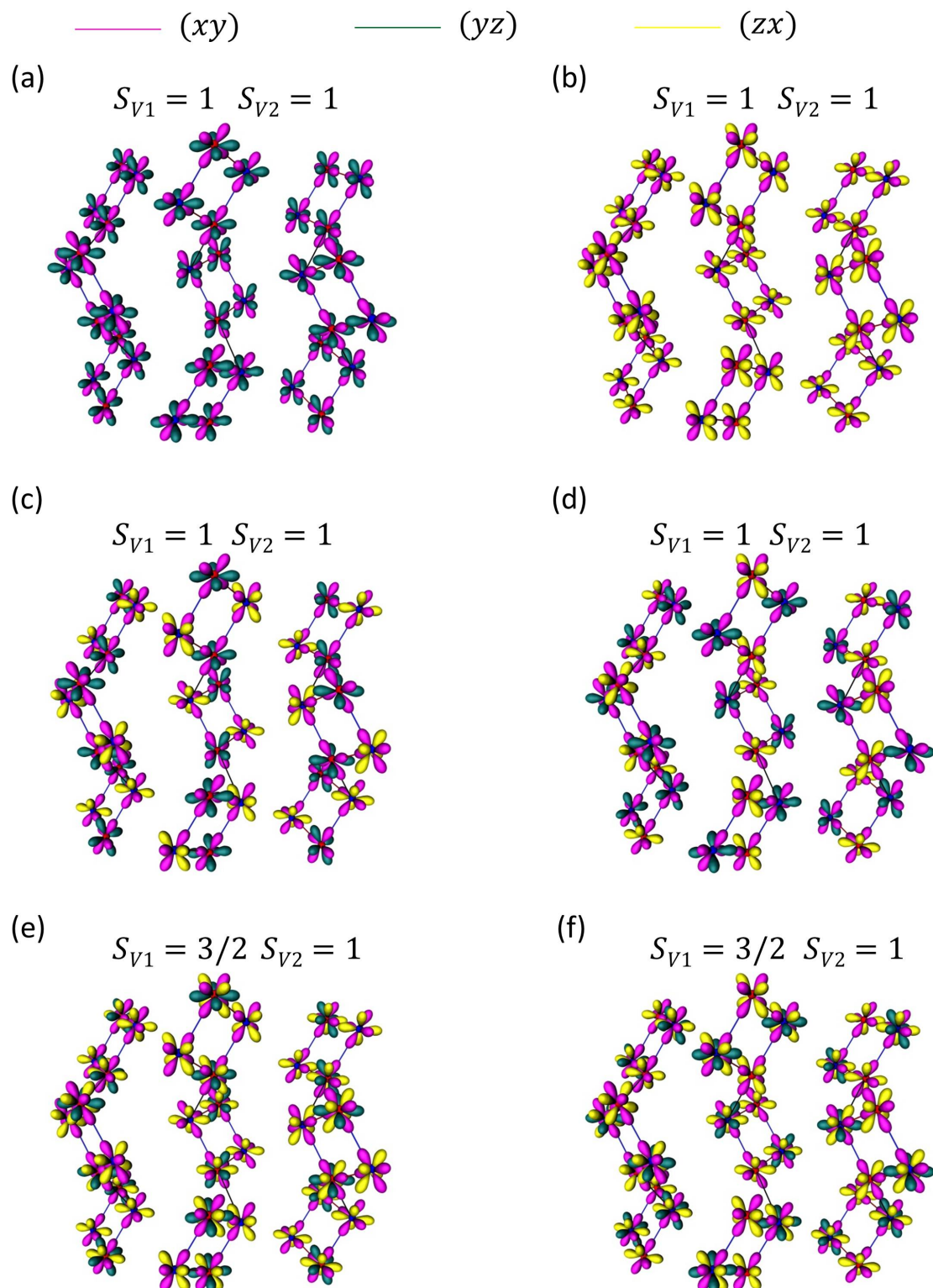


FIGURE 3.20: Possible orbital configurations for V1 and V2 ions

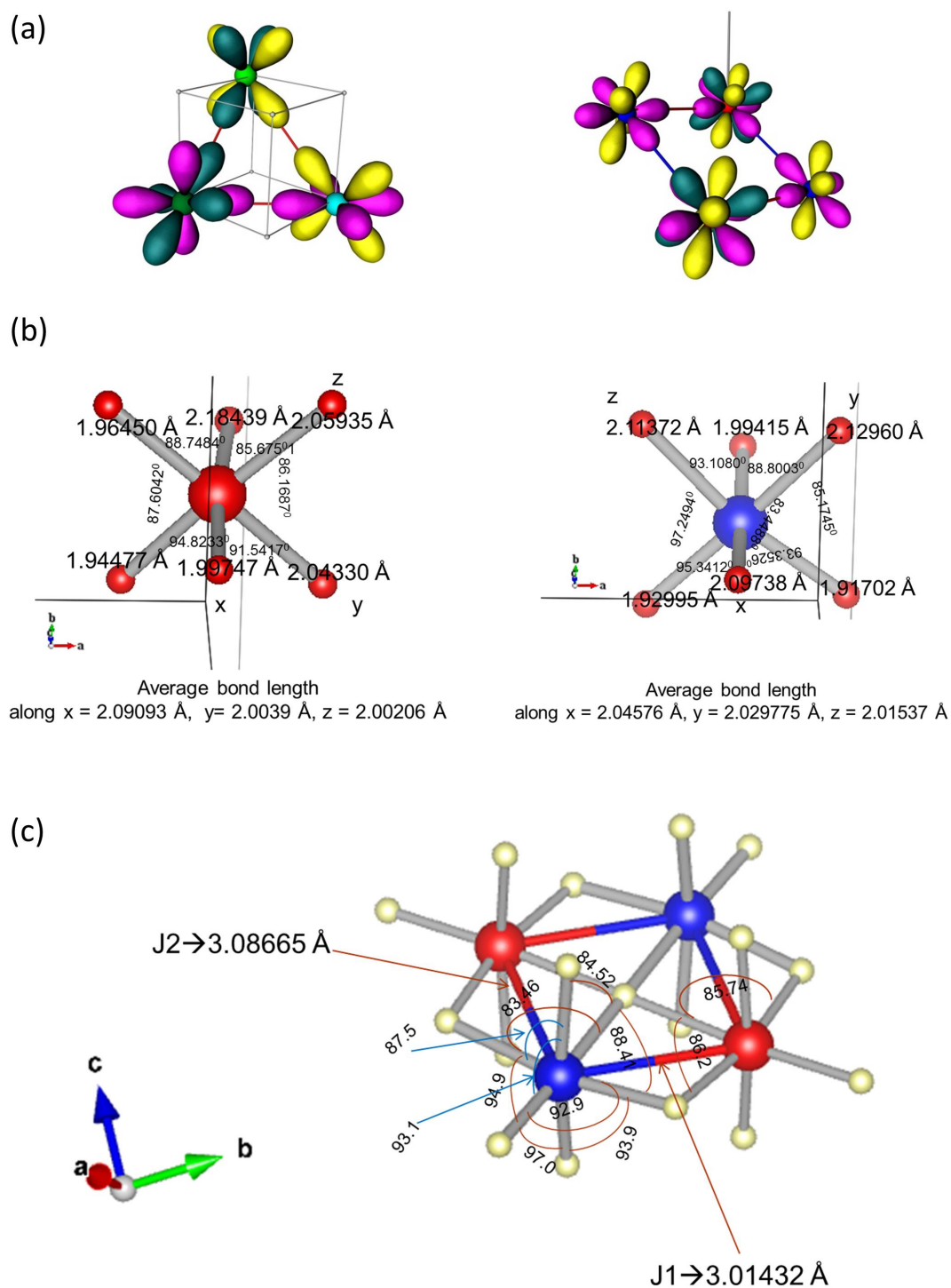


FIGURE 3.21: (a) Possible orbital models for V2B, V3 and V3B ions (left) and V1 and V2 ions (right) (b) Octahedral environment of V1 and V2 ions by oxygen (c) Octahedral environment within the pseudo-square with V1 and V2 ions and respective bond length and angles

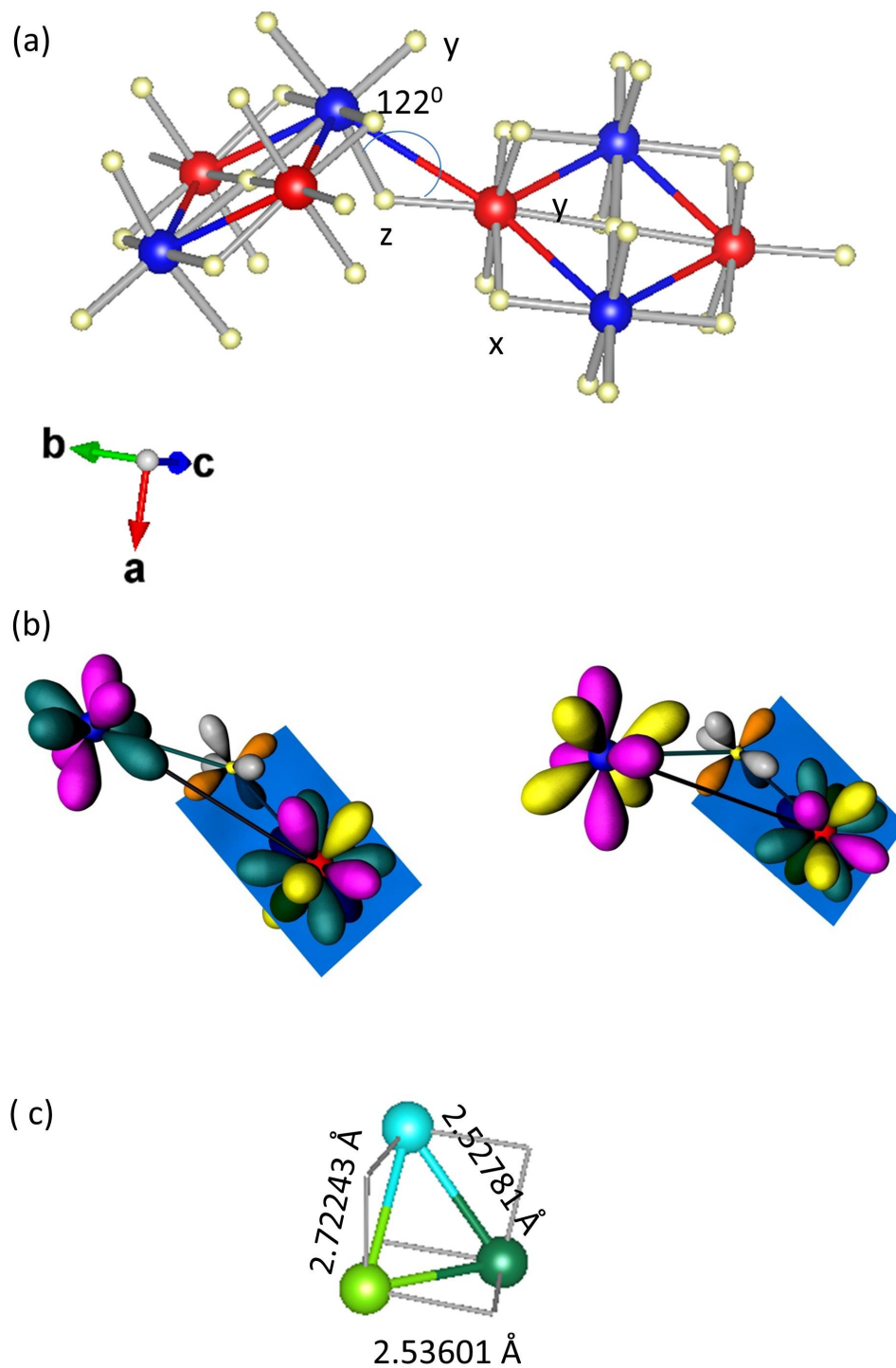


FIGURE 3.22: (a) Corner sharing bonding of 120° in the octahedral environment of V1 and V2 ions by oxygen (b) Two possible orbital arrangements for V1 and V2 with the Oxygen p orbitals (c) Trimer bonds between V2B, V3 and V3B

3.6 Summary and Conclusions

In this chapter, orbital and magnetic properties of highly frustrated magnet BaV₁₀O₁₅ are presented. Combining both elastic and inelastic neutron scattering techniques, we successfully found a probable model for the low temperature magnetic structure. The magnetic structure is a long range ordered state of V1 and V2 ions forming a pseudo-square in the bc plane. These pseudo-squares are connected along c axis with another pseudo-square in a different layer translated along b axis.

Even though the magnetic unit cell consists of 80 magnetic ions in the unit cell, we observed simple and unique excitations along symmetry directions. With the help of the features observed in the inelastic neutron scattering data, probable magnetic structure were systematically investigated. The magnetic structure consists of AFM spin chains along $\sim b$ axis in $+ + - - + +$ fashion and FM chains along $\sim c$ axis. The linear spin-wave calculations performed for the above spin structure could reproduce our observed inelastic neutron scattering data using a Hamiltonian with the nearest neighbor and the next nearest neighbor interactions.

Orbital models for the V ions in BaV₁₀O₁₅ that qualitatively match with the model Hamiltonian are also proposed. Higher energy excitations observed might be at least partially due to singlet to triplet excitations from the spin singlet trimer formed by the ions which did not order below T_N . Further inelastic neutron scattering experiments using a single crystal of BaV₁₀O₁₅ at much higher temperatures (75 K and 150 K) will be useful in identifying the contribution of higher energy excitation to spin wave and singlet to triplet excitation.

Chapter 4

Orbital glass state and spin correlations of spinel CoV_2O_4

4.1 Introduction

4.1.1 Introduction to Spinel Vanadates

Spinel structures AB_2O_4 have been extensively studied to find various exotic phenomena due to the effects of magnetic and orbital frustration. Among them are zero energy excitation modes in the spin liquid phase of the spinel chromates, zero-field and field-induced novel phase transitions in chromates and vanadates, and heavy fermionic behaviors in LiV_2O_4 to name few [62]. In spinel AB_2O_4 , B-site forms the most frustrated arrangement in three dimensions; a network of corner sharing tetrahedra. B site is surrounded by six oxygen atoms in an octahedral arrangement and edge sharing with other nearest B-sites. Thus, the dominant antiferromagnetic nearest neighbor interactions are present making it a highly frustrated unit [61]. Among the spinel family, spinel vanadates AV_2O_4 provide a novel playground to study the novel phases emerging from the interplay between lattice, spin and orbital degree of freedom. In spinel vanadates magnetic V^{3+} ions with two t_{2g} d -electrons have orbital degree of freedom in addition to its spin.

Spinel vanadates can be categorized into two families. The first category is when A-site is non-magnetic (Zn,Cd) and the other is when it is magnetic (Mn,Fe,Co). Upon cooling, the systems belonging to the first category with non-magnetic A^{2+} ions ($A=\text{Zn,Cd}$) undergo a first order structural phase transition due to an orbital order and a magnetic order at a lower temperature[63–65]. In ZnV_2O_4 a sharp drop in bulk susceptibility is observed at $T_c = 50$ K due to structural phase transition from cubic to tetragonal and the system long range orders at $T_N = 40$ K[63]. A similar behavior is observed in

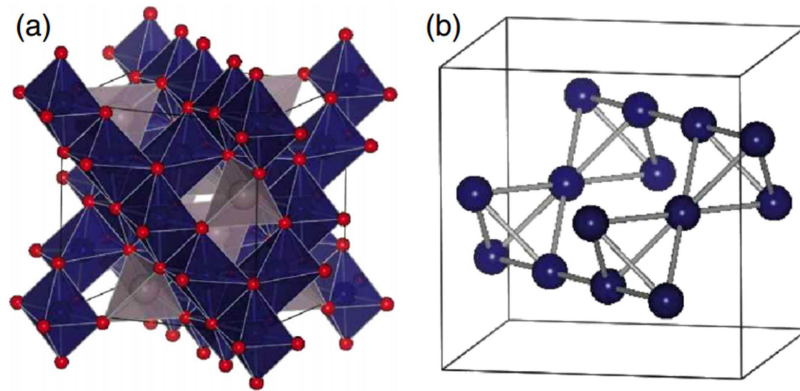


FIGURE 4.1: (a) Crystal structure of spinel AB_2O_4 . The blue (grey) polygon represents BO_6 octahedron (AO_4 tetrahedron). The neighboring BO_6 octahedra share an edge. (b) The three-dimensional network of corner-sharing tetrahedra formed by B-site. (From reference [62])

CdV_2O_4 with $T_c = 90$ K and $T_N = 30$ K[65]. High temperature cubic paramagnetic, the intermediate tetragonal paramagnetic, and the low temperature tetragonal long range ordered phase are common for these systems.

When the A-site is magnetic (Mn,Fe,Co) the spin and orbital interplay between A-site and B-site also plays a vital role. All of these three systems, MnV_2O_4 , FeV_2O_4 and CoV_2O_4 , undergo a ferrimagnetic transition upon cooling where spins in A-site are opposite to spins in B-site, but with different magnetic moments.

MnV_2O_4 [16, 66–74] exhibits a ferrimagnetic transition at $T = 56$ K and a structural phase transition from cubic phase to orbital ordered tetragonal ($c < a$) phase at a slightly lower temperature $T = 53$ K. Simultaneously the magnetic structure changes from collinear ferrimagnetic to non-collinear ferrimagnetic structure with canting from c -axis about 65 degrees. Several orbital models were proposed for this system. A model with antiferro orbital where one 3d electron occupies the xy orbital at every V site, and the other occupies the yz and zx orbitals alternately along the c axis[16] was initially proposed and later theoretical results suggested a much more complicated orbital pattern considering the trigonal distortion of VO_6 octahedra [71, 72].

FeV_2O_4 [75–83] on the other hand presents a more complex situation where both A-site and B-site are orbitally active. As a result several successive phase transitions are observed. Upon cooling, from cubic, high-temperature tetragonal, orthorhombic, and low-temperature tetragonal phases ($c > a$) are caused due to orbital degree of freedom of both Fe^{2+} and V^{3+} ions [75]. The low temperature tetragonal transition is associated with transition from collinear to non-collinear ferrimagnetic structure driven by orbital order of V^{3+} ions, but magnetic structure of FeV_2O_4 is different from MnV_2O_4 where

V spins point to $\langle 111 \rangle$ directions of the VO₆ octahedra and 45° different from those of MnV₂O₄ when projected onto the xy plane[77].

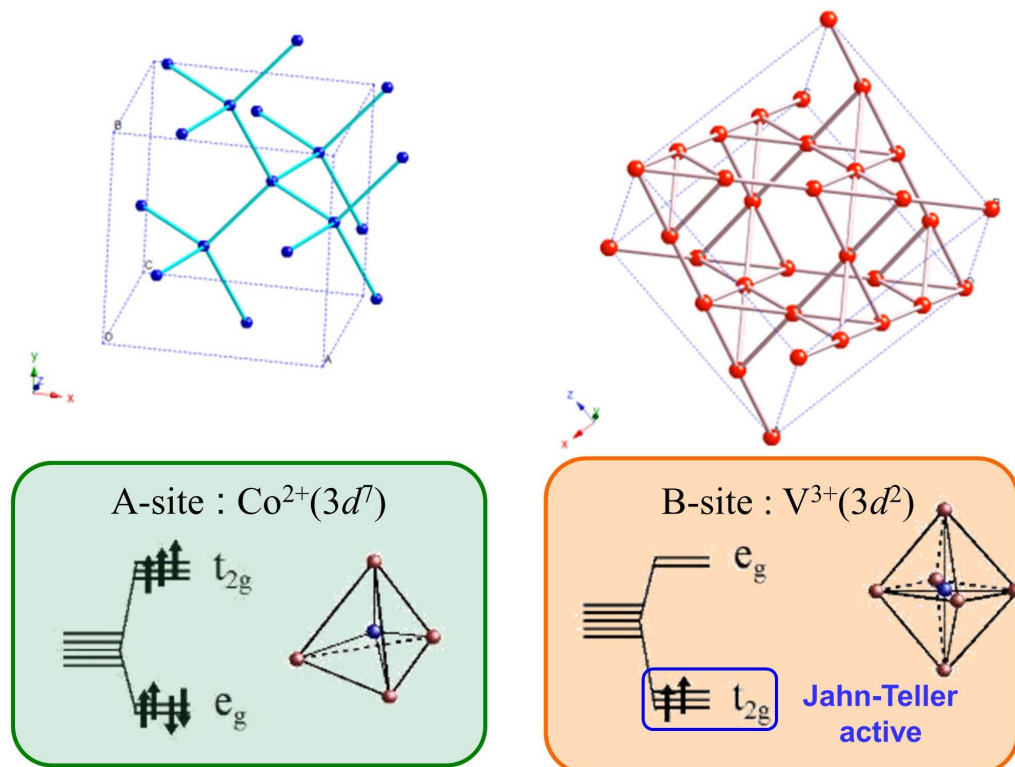
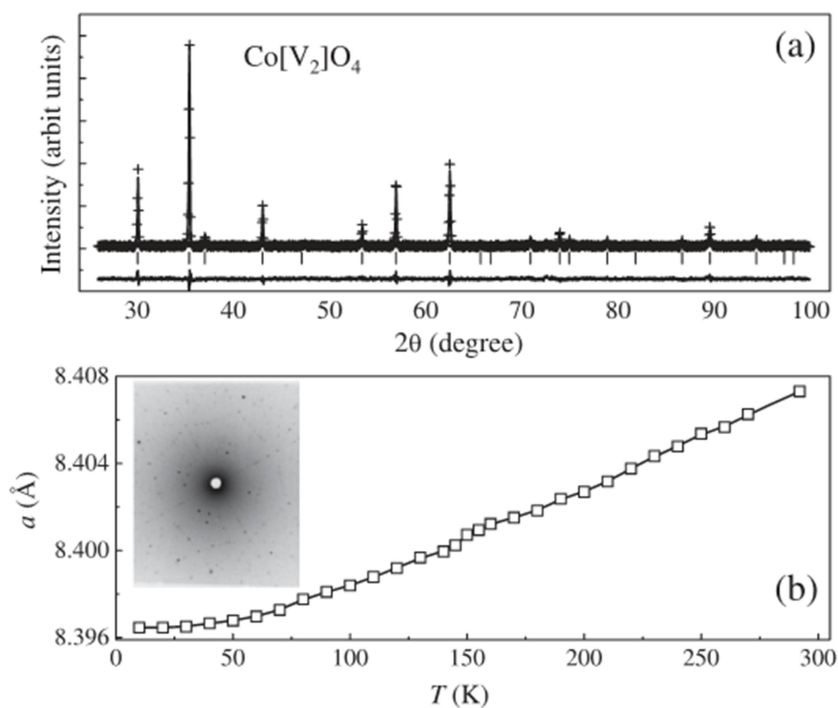
Spinel CoV₂O₄ is less studied compared to other spinels [84–89]. Spinel CoV₂O₄ lies close proximity to itineracy and provides a unique situation to study the magnetic, structural and orbital properties. Nevertheless, the interplay between spin, lattice and orbital degree of freedom has been difficult to study due to the nearly metallic state.

4.1.2 Crystal structure and bulk properties CoV₂O₄

Spinel CoV₂O₄ with Co²⁺ ($e_g^4 t_{2g}^3$) and V³⁺ (t_{2g}^2) has been studied since 1960's and reported to have cubic crystal structure with $Fd\bar{3}m$ symmetry at room temperature[90–92]. In one unit cell of CoV₂O₄ there are 8 cobalt ions, 16 vanadium ions and 32 oxygen ions. It is reported using X-ray diffraction data that the crystal structure remains cubic down to 10 K as shown in figure 4.3 [84]. No detectable lattice distortions are observed using X-ray diffraction while cooling[86].

Although CoV₂O₄ crystal structure is reported to remain cubic, upon cooling several transitions are observed in both magnetization and heat capacity measurements. Bulk susceptibility study and heat capacity measurements revealed a ferrimagnetic transition at $T_C = 150$ K [84]. Subsequent studies on the bulk properties of CoV₂O₄ done on polycrystalline samples reported two cusps at 60 K and 100 K below T_C in magnetization as shown in figure 4.4 and specific heat data exhibited a large peak at $T_C = 150$ K with another additional peak at 60 K. No peak was observed at 100 K. The peak at 60 K was attributed to a short range orbital order. This study was conflicting with a previous single crystal study where only one peak of magnetization at $T = 75$ K was observed but no corresponding peak in heat capacity was detected[85].

A recent dielectric study has shown evidence for very small structural distortion at low temperatures. Due to near metallic state of CoV₂O₄, measurements had been performed only at temperatures below 30 K. According to their dielectric measurements, it is predicted that CoV₂O₄ single crystal undergoes slight distortions with a contraction ($c < a$) along the direction of the applied field[88].

FIGURE 4.2: Arrangement of Co and V sites of CoV_2O_4 and the crystal field splittingFIGURE 4.3: X-ray Diffraction pattern for CoV_2O_4 at room temperature. (b) Temperature dependence of the lattice parameter for CoV_2O_4 (from reference [84])

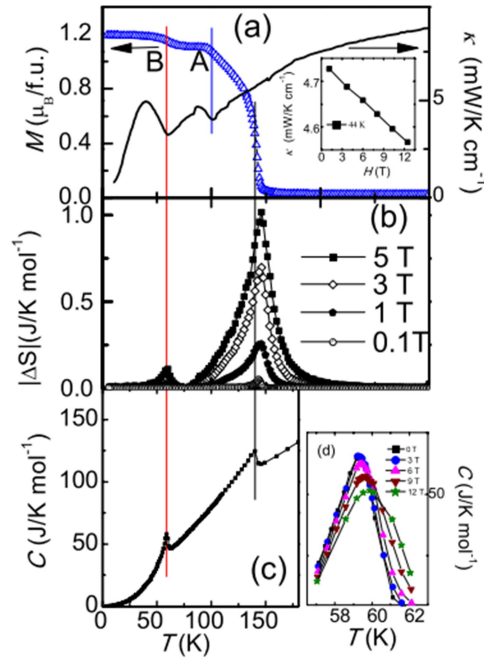


FIGURE 4.4: Figure from reference [86]. The temperature dependence of (a) the magnetization and the thermal conductivity (b) the magnetic entropy change; (c) the heat capacity; (d) the field dependence of the transition peak at 59 K, for CoV₂O₄.

4.1.3 Near metallic nature of CoV₂O₄

Vanadium spinels AV_2O_4 show wide range of properties from insulating to semiconducting and even near metallic. Figure 4.5 adapted from reference [84] summarizes how the activation and c/a ratio change with vanadium-vanadium distance (R_{VV}) associated with different vanadium spinels. This system approaches the itinerant electron limit as R_{VV} decreases [90]. CdV₂O₄ is the most insulating out of this family with the largest R_{VV} . On the other hand, CoV₂O₄ has $R_{VV}=2.9724 \text{ \AA}$ at room temperature is the smallest for this spinel family, and thus reside closest to the metallic state. This distance is very close to the critical vanadium-vanadium distance predicted for a metallic state which is 2.94 \AA [93]. Upon application of pressure, R_{VV} distance further reduces and increases the ferrimagnetic transition temperature T_C . At around 6 GPa metallic conductivity occurs for CoV₂O₄ giving rise to overlap of valence and conduction bands. Nevertheless the resistivity is still much higher than a good metal under this condition [84].

Recent theoretical calculations show that spinorbit interaction coupled with Coulomb correlation is important to reproduce the semiconducting behavior at ambient pressure. It is being predicted from the calculations that effective spinless FalicovKimball model

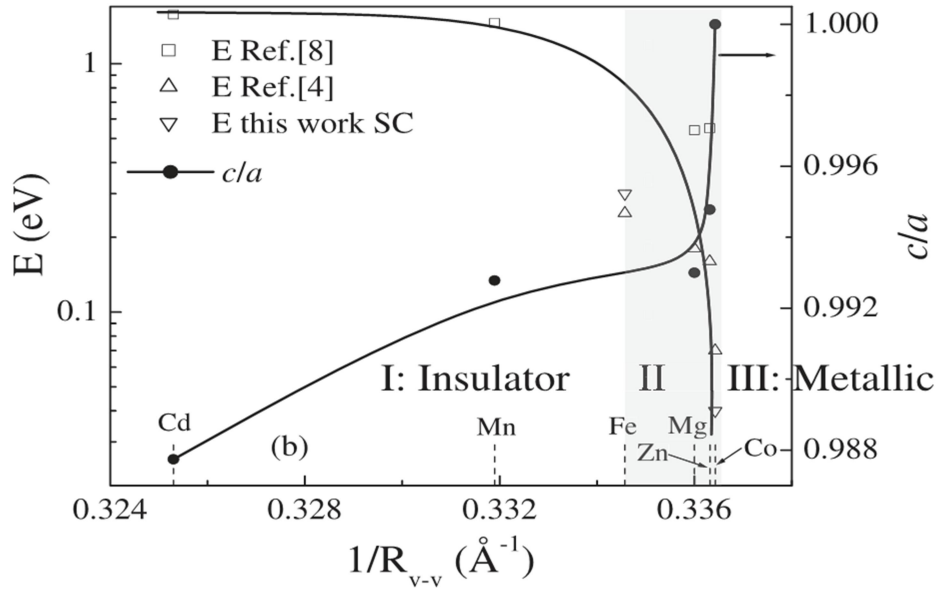


FIGURE 4.5: Activation energy, E and c/a ratio of AV_2O_4 spinels as a function of V-V distance. (from reference [84])

with two degenerate itinerant bands and one localized can be a better explanation for this system[87]. Another recent neutron scattering study of $Mn_{1-x}Co_xV_2O_4$ proposed disappearance of orbital order by extrapolating from the data of $x \leq 0.8$ samples due to enhancement of itineracy with Co doping.

Nevertheless, observed anomalies in $M(T)$ below T_C are not full understood to the date. These anomalies might suggest that the orbital degree of freedom play an important role in this system although the associated lattice distortion might be too small to be detected easily from the diffraction measurements. Thus, an experiment probe that is more sensitive to the subtle changes of magnetic and structural properties is essential to understand this system[94]. Here, in this chapter I will discuss our polarized and unpolarized neutron scattering results and analysis along with the magnetorestriction measurements performed by the collaborating group at Wesada University, Japan.

4.2 Methods

4.2.1 Experimental details

Single crystals and polycrystalline samples of CoV₂O₄ were synthesized and grown by Prof. Takuro Katsufuji's group at Waseda University, Japan. Single crystals were grown by the floating-zone technique. It is found that a large single crystal cannot be grown but a V₂O₃ impurity phase appears if crystal growth is started with a polycrystalline rod having a stoichiometric amount of Co and V (= 1 : 2). Thus, the single crystals with three different amounts of additional Co (#1, #2, #3) were grown. Polycrystalline samples with intentionally increased amounts of Co, Co_{1+x}V_{2-x}O₄ ($x = 0, 0.1, 0.2$), were synthesized in sealed quartz tubes for comparative studies. Magnetizations of the samples were measured at Waseda University by a SQUID magnetometer and the strain measurement was performed by a strain-gauge technique.

Neutron powder diffraction (NPD) measurements were performed on the BT1 powder diffractometer with a Cu(311) monochromator ($\lambda = 1.5398 \text{ \AA}$) for several different temperatures. Powder samples were loaded into vanadium cans in a He atmosphere and mounted in a close-cycle refrigerator. The single crystal neutron diffraction measurements were performed at E5 4-Circle Diffractometer at HZB with neutron wavelengths of $\lambda = 2.4 \text{ \AA}$ and 0.9 \AA . Polarized elastic neutron scattering experiments were performed at HB1 Polarized Triple-Axis Spectrometer at High Flux Isotope Reactor (HFIR), ORNL with neutron energy of 13.5 meV. Vertical guide field of 3 T was applied using 8 T Vertical Asymmetric Field Cryomagnet. The inelastic neutron scattering (INS) measurements were performed first at cold neutron triple axis spectrometer with fixed final neutron energy of 5 meV. Then to understand the higher energy excitations, inelastic neutron scattering experiments with thermal neutrons were performed at HB1 Polarized Triple-Axis Spectrometer at HFIR, ORNL with fixed final neutron energy of 13.5 meV. To further understand the excitations with detailed spectrum, time of flight inelastic neutron scattering experiments were performed at ARCS spectrometer at Spallation Neutron Source, ORNL with monochromatic neutrons of incident energies $E_i = 60 \text{ meV}$. The single crystal sample was aligned in [HH0] plane for all the single crystal experiments.

4.2.2 Calculation details

Neutron diffraction data were analyzed to find the crystal and magnetic structures of both powder and single crystal samples of CoV₂O₄. Rietveld refinements were carried out using the FULLPROF program [58]. Group theoretical analysis to find the magnetic

structure were performed using Sarah software [35]. Linear spinwave calculations were performed using SpinW program [39] written in Matlab.

4.3 Crystal and magnetic structure

4.3.1 Neutron powder diffraction data

Investigating the detailed crystal and magnetic structure was the first objective of the study. Neutron powder diffraction measurements were performed at BT1 neutron powder diffractometer at National Institute of Standards and Technology. NPD data were collected at several different temperatures. Figure 3.1 shows the neutron diffraction data and Rietveld refinements for several different temperatures. The data were collected for 12 hours, 8 hours and 4 hours for 2 K, 55 K and 100 K respectively. The refinement includes both nuclear and magnetic phase. Details of the magnetic refinement will be discussed later in this chapter.

It is previously reported that CoV₂O₄ has a cubic structure with $Fd\bar{3}m$ space group down to 10 K [84]. Neutron diffraction data around (008) Bragg peak were measured for several different temperatures to confirm whether there is any structural transition in the system or not. Figure 4.7 (a) shows the intensity of (008) peak for several different temperatures. Upon cooling from room temperature, there is a gradual shift of Bragg peak but there is no observable peak splitting. Figure 4.7 (b) shows the FWHM of the (008) Bragg peak fitted with a Gaussian function and FWHM stays almost constant with temperature. Upon cooling down if there is any observable change in crystal symmetry from cubic to tetragonal, either the (008) peak should split, or a change in width of the peak should be visible. Thus, within the resolution of the experiment, the crystal structure of CoV₂O₄ remains cubic down to 5 K.

Structural parameters and goodness-of-the-fit from the refinement are listed in Table 4.1.

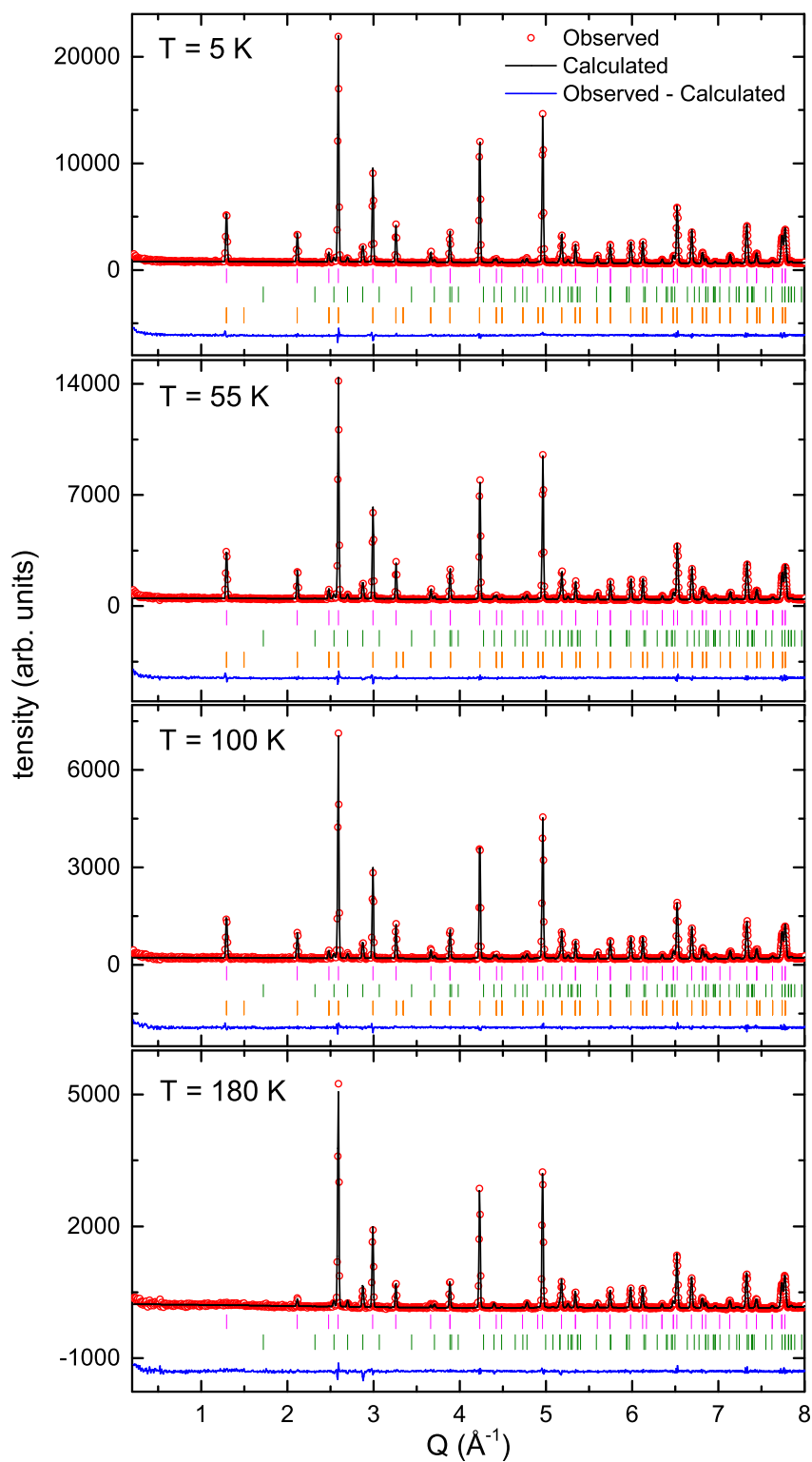


FIGURE 4.6: Neutron powder diffraction data of CoV₂O₄ measured at 5 K, 55 K and 100 K. Circles are the data and the black line represents the calculated intensity obtained from the refinement by Fullprof for collinear and non-collinear spin structures. Green bars represent nuclear and magnetic Bragg peak positions and blue lines indicate difference between data and calculation.

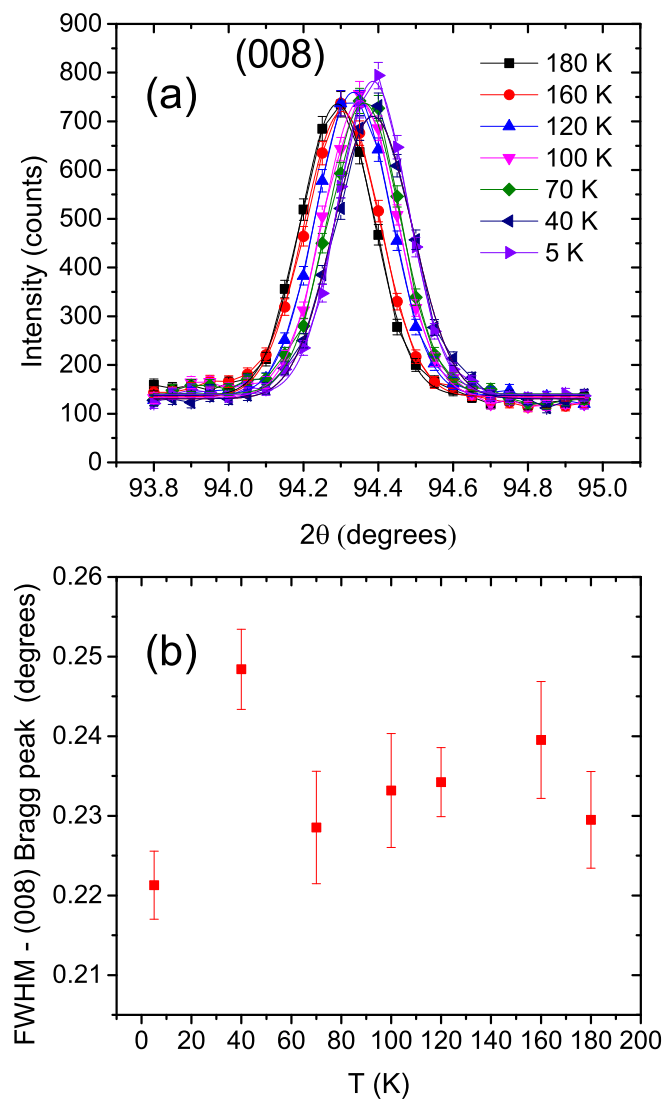


FIGURE 4.7: (a) Temperature dependence of the (008) Bragg peak intensity as a function of the scattering angle. (b) FWHM of the (008) Bragg peak fitted with a Gaussian function as a function of temperature.

TABLE 4.1: The crystal structural parameters of CoV₂O₄ by refining the data shown in Fig.4.6 using the program FULLPROF. B_{iso} is an isotropic thermal parameter expressed as $\exp(-B_{\text{iso}} \sin^2 \theta / \lambda^2)$, where θ is the scattering angle and λ is the wavelength of the neutron. R_{wp} and χ^2 correspond to the weighted R factor and chi-square. The space group symmetry is $Fd\bar{3}m$

	R_{wp}	R_{mag}	$a(\text{\AA})$	Co (3b) (x=y=z) B_{iso}	V (9e) (x=y=z) B_{iso}	O (6c) (x=y=z) B_{iso}
	χ^2					
T = 6 K	3.14 2.0	12.15	8.39542(3)	0.125 0.25(3)	0.5 0.30	0.26050(2) 0.209(8)
T = 55 K	2.69 1.7	8.01	8.39561(3)	0.125 0.32(4)	0.5 0.30	0.26050(3) 0.218(9)
T = 100 K	2.94 1.13	7.18	8.39755(3)	0.125 0.26(4)	0.5 0.30	0.26050(3) 0.23(1)
T = 180 K	3.62 1.31	-	8.40147(4)	0.125 0.43(6)	0.5 0.30	0.26050(4) 0.29(1)

4.3.2 Magnetic structure refinement

As discussed in Chapter 2, Representational Analysis allows the determination of the symmetry-allowed magnetic structures that can result from a second-order magnetic phase transition, given the crystal structure before the transition and the propagation vector of the magnetic order [28–35]. These calculations were carried out using the program *SARAH-Representational Analysis* [35].

In our case, the crystal structure of CoV₂O₄ before the phase transition can be reproduced by the space group $Fd\bar{3}m$ (#227:2). This space group involves 4 centering operations and 48 symmetry operations.

The decomposition of the magnetic representation Γ_{Mag} in terms of the non-zero IRs of $G_{\mathbf{k}}$ for each crystallographic site is examined, and their associated basis vectors, ψ_n , are given in Tables 4.2 and 4.3. The labeling of the propagation vector and the IRs follow the scheme used by Kovalev [36].

Possible magnetic structures were investigated by carrying out all the possibilities of basis vector combination listed in Tables 4.2 and 4.3. From the bulk susceptibility data, it is known that this system undergoes a ferrimagnetic transition at $T_C = 169$ K. Among the possible irreducible representations of $Fd\bar{3}m$ symmetry with $\mathbf{k}=(0,0,0)$ only one irreducible representation Γ_9 can produce a ferrimagnetic arrangement between Co and V spins. Using the Γ_9 representation we found two possible magnetic structures. The magnetic structure that yields the best refinement factor at 5 K is a non-collinear structure as shown in Fig. 4.8(b). Co and V spins have ferrimagnetic moments along c -axis.

TABLE 4.2: Basis vectors for the space group $Fd\bar{3}m:2$ with $\mathbf{k}_{11} = (0, 0, 0)$. The decomposition of the magnetic representation for the *Co* site (.125, .125, .125) is $\Gamma_{Mag} = 1\Gamma_8^3 + 1\Gamma_9^3$. The atoms of the nonprimitive basis are defined according to 1: (.125, .125, .125), 2: (.875, .875, .875).

IR	BV	Atom	BV components					
			$m_{\parallel a}$	$m_{\parallel b}$	$m_{\parallel c}$	$im_{\parallel a}$	$im_{\parallel b}$	$im_{\parallel c}$
Γ_8	ψ_1	1	8	0	0	0	0	0
		2	-8	0	0	0	0	0
	ψ_2	1	0	8	0	0	0	0
		2	0	-8	0	0	0	0
	ψ_3	1	0	0	8	0	0	0
		2	0	0	-8	0	0	0
Γ_9	ψ_4	1	8	0	0	0	0	0
		2	8	0	0	0	0	0
	ψ_5	1	0	8	0	0	0	0
		2	0	8	0	0	0	0
	ψ_6	1	0	0	8	0	0	0
		2	0	0	8	0	0	0

TABLE 4.3: Basis vectors for the space group F d -3 m:2 with $\mathbf{k}_{11} = (0, 0, 0)$ for V site (.5, .5, .5). $\Gamma_{Mag} = 1\Gamma_3^1 + 1\Gamma_5^2 + 1\Gamma_7^3 + 2\Gamma_9^3$. Atoms, 1: (.5, .5, .5), 2: (.5, .25, .25), 3: (.25, .5, .25), 4: (.25, .25, .5).

IR	BV	Atom	BV components					
			$m_{\parallel a}$	$m_{\parallel b}$	$m_{\parallel c}$	$im_{\parallel a}$	$im_{\parallel b}$	$im_{\parallel c}$
Γ_3	ψ_1	1	12	12	12	0	0	0
		2	12	-12	-12	0	0	0
		3	-12	12	-12	0	0	0
		4	-12	-12	12	0	0	0
Γ_5	ψ_2	1	6	-6	0	0	0	0
		2	6	6	0	0	0	0
		3	-6	-6	0	0	0	0
		4	-6	6	0	0	0	0
	ψ_3	1	3.464	3.464	-6.928	0	0	0
		2	3.464	-3.464	6.928	0	0	0
		3	-3.464	3.464	6.928	0	0	0
		4	-3.464	-3.464	-6.928	0	0	0
Γ_7	ψ_4	1	0	-2	2	0	0	0
		2	0	2	-2	0	0	0
		3	0	2	2	0	0	0
		4	0	-2	-2	0	0	0
	ψ_5	1	2	0	-2	0	0	0
		2	-2	0	-2	0	0	0
		3	-2	0	2	0	0	0
		4	2	0	2	0	0	0
	ψ_6	1	-2	2	0	0	0	0
		2	2	2	0	0	0	0
		3	-2	-2	0	0	0	0
		4	2	-2	0	0	0	0
Γ_9	ψ_7	1	4	4	4	0	0	0
		2	4	-4	-4	0	0	0
		3	4	-4	4	0	0	0
		4	4	4	-4	0	0	0
	ψ_8	1	4	-2	-2	0	0	0
		2	4	2	2	0	0	0
		3	4	2	-2	0	0	0
		4	4	-2	2	0	0	0
	ψ_9	1	4	4	4	0	0	0
		2	-4	4	4	0	0	0
		3	-4	4	-4	0	0	0
		4	4	4	-4	0	0	0
ψ_{10}	1	-2	4	-2	0	0	0	
	2	2	4	-2	0	0	0	
	3	2	4	2	0	0	0	
	4	-2	4	2	0	0	0	
ψ_{11}	1	4	4	4	0	0	0	
	2	-4	4	4	0	0	0	
	3	4	-4	4	0	0	0	
	4	-4	-4	4	0	0	0	
ψ_{12}	1	-2	-2	4	0	0	0	
	2	2	-2	4	0	0	0	
	3	-2	2	4	0	0	0	
	4	2	2	4	0	0	0	

V moments are canted away from *c*-axis by 20° with antiferromagnetic (AFM) *ab* component of magnetic moment along (110) directions. The frozen moment was determined to be $\langle M \rangle_{\text{Co}} = 2.89(3) \mu_{\text{B}}/\text{Co}$, that is, close to the expected value of the magnetic moment for the high-spin state of Co^{2+} of $3 \mu_{\text{B}}$ and $\langle M \rangle_{\text{V}} = 0.71(3) \mu_{\text{B}}/\text{V}$ which is much less than the expected value for V^{3+} of $2 \mu_{\text{B}}$. On the other hand collinear structure also gives a reasonably good fitting for our data with $\langle M \rangle_{\text{Co}} = 2.95(2) \mu_{\text{B}}/\text{Co}$ and $\langle M \rangle_{\text{V}} = 0.75(2) \mu_{\text{B}}/\text{V}$. (200) bragg peak which is forbidden by the crystal symmetry is a pure magnetic peak. In other spinels, MnV_2O_4 and FeV_2O_4 , a non-zero intensity of (200) peak was observed below the temperatures of their structural transition temperature (T_s) and intensity becomes zero above T_s . AFM V moments which are canted away from *c*-axis (65° MnV_2O_4 and 55° for FeV_2O_4) are responsible for the non-zero intensity of (200) peak at low temperatures below T_s , as intensity of (200) Bragg peak is proportional to the square of the sum of the in-plane moment of V ions. In our powder diffraction data of CoV_2O_4 , no clear intensity increase was observed for (200) bragg peak position, though it is still possible that it is hidden in the background. Although non-collinear structure having AFM component for V moments produces a non-zero intensity at (200) bragg peak position, the calculated relative intensity of (200) bragg peak is 1.2% of the calculated intensity of the main magnetic bragg peak (111) for the refined non-collinear magnetic structure with canting from *c*-axis by 20° . From powder diffraction it is difficult to observe such a weak intensity. According to the reliability factor R_{Mag} the canted ferrimagnetic structure was favorable compared to collinear ferrimagnetic structure with a better fitting of other magnetic peaks. To check whether there is a magnetic transition at T_p , powder diffraction data at 55 K and 100 K were collected. Refinement of the 100 K data for both collinear and non-collinear structures were carried out. Although non-collinear model with canting from *c*-axis by 16.85° gives a better reliability factor $R_{\text{Mag}}=7.28$, both models fit with the NPD data quite well. From the temperature dependence of the refined canting angle it is evident that the canting angle started to decrease for temperature at a temperature around 100 K, but it is not clear from powder diffraction measurements whether the collinear to non-collinear transition is present in the system at some temperature below ferrimagnetic transition temperature $T_C = 169$ K. Single crystal diffraction measurements were necessary to observe the very weak (200) Bragg peak intensity which is directly related to the canting angle of V spins, and thus to check whether there is a possible reorientation of the spins in this system at a lower temperature. The single crystal diffraction results, both unpolarized and polarized elastic neutron scattering will be discussed in a later section of this chapter.

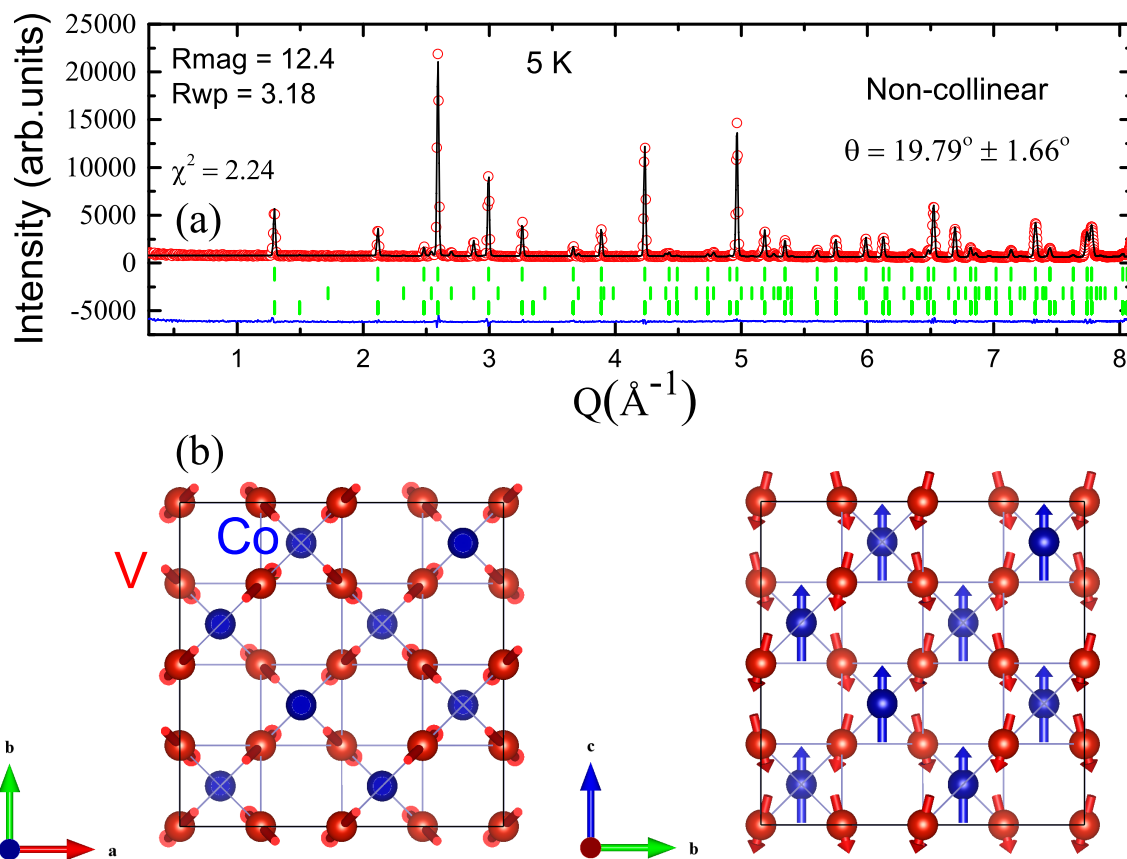


FIGURE 4.8: Neutron powder diffraction data of CoV₂O₄ measured at 5 K. Circles are the experimental data and black lines represent the calculated intensities. Green bars represent nuclear and magnetic Bragg peak positions and blue lines indicate difference between experimental data and calculation. (c) A sketch of the magnetic structures for CoV₂O₄.

4.4 Temperature dependence

4.4.1 Bulk susceptibility and Magnetostriction data

In this section the magnetization and magnetostriction measurements performed on CoV₂O₄ single crystal and powder samples will be discussed. The data were obtained from the collaborative work done by Prof. Takuro Katsufuji's group at Waseda University, Japan. The work discussed in this section will be published as in Reference [94]

T dependence of the magnetization $M(T)$ of single crystal sample (#1) of CoV₂O₄ is shown in Figure 4.9. Magnetic field of 0.1 T along the [100] axis is applied. It has been found that by induction-coupled plasma the estimated Co:V ratios of the #1 and #2 single crystals were 1.21:1.79 and 1.3:1.7 [94].

$M(T)$ increases below ferrimagnetic transition temperature $T_C = 169$ K without any clear anomaly. Although the single crystal sample does not show any anomaly, a powder sample obtained by the grinding the single sample (#1) shows a peak at 45 K, which we denote as T_p . $M(T)$ of other ground single crystals and polycrystalline samples are shown in Fig. 4.11 (a). A peak in $M(T)$ exists for all the samples below T_C . Interestingly, the peak position, T_p , and T_C vary with samples but as T_C increases, T_p decreases. As shown in Fig. 4.11 for single crystal and polycrystalline samples of Co_{1+x}V_{2-x}O₄, T_C increases as x increases while T_p decreases.

Magnetostriction phenomenon can be found in ferromagnetic materials which is based on magnetomechanical properties of these materials. In a ferromagnetic material its structure is divided into magnetic domains, each of which has a uniform magnetic polarization. When Ferromagnetic materials are placed in a magnetic field, the boundaries between the domains shift and the domains rotate, which can cause a microscopic distortion of their dimensions. These domains show a tendency towards parallel arrangement within a limited field. This distortion can be detected in the diffraction measurement with extremely high resolution.

There are several possible mechanisms of magnetostriction, but in any case, the coupling between spin and orbital (either intersite or intrasite) plays some role, short or long-range order of orbitals may results in a small change in the crystal structure.

Let's now look at the result of strain measurements [94], with applied magnetic field H along a crystal axis, say [001] which we can call the c axis in rest of the discussion. Strain measurements, $\Delta L/L$, for single crystal sample #1 of CoV₂O₄ are shown in Fig.

4.10. Fig. 4.10 (a) and (b) shows the change in $\Delta L/L \parallel H$ and $\Delta L/L \perp H$ with applied magnetic field H for various temperatures.

Figure 4.10 (c) shows the T dependence of low- H $\Delta L/L$. The low- H $\Delta L/L$ is zero for $T > T_C$ and increase gradually below T_C for $\Delta L/L \parallel H$ and attain maximum ($\parallel H$) around $T = 100$ K. With further cooling it change their signs at 45 K with an anomaly.

As discussed previously, magnetic domains are initially randomly oriented without any field and become aligned under an external magnetic field. This alignment causes a macroscopic elongation or contraction of the crystal. The absolute values of the elongation or contraction along the direction of the magnetization can be obtained by taking the difference between the low- H $\Delta L/L$ for $\Delta L/L \parallel H$ and that for $\Delta L/L \perp H$. Figure 4.10 (d) shows this result, which is denoted as $\Delta L_{\text{diff}}/L$, as a function of T . This quantity is a measure of $(\frac{c}{a} - 1)$ where a and c are the lattice constants, assuming that the magnetic moments are along the c axis. Interestingly, $\Delta L_{\text{diff}}/L$ first increases in second order fashion with a weak lattice distortion of an order of $\Delta L_{\text{max}}/L \sim 10^{-4}$ at 100 K and with further cooling it smoothly crosses the zero line at 45 K with no anomaly. It is notable that T at which the sign of $\Delta L_{\text{diff}}/L$ changes coincides with T_p , the peak temperature of $M(T)$ shown in Fig. 4.9 (a). The change in $\Delta L_{\text{diff}}/L$ thus the $\frac{c}{a} - 1$ with temperature is completely different from MnV_2O_4 as shown in Fig. 4.10. In MnV_2O_4 a strong first order crystal distortion is present due to an orbital order of $\text{V}^{3+} t_{2g}$ orbitals. Even though it is weak compared to MnV_2O_4 , our result clearly shows a second order type crystal distortion that changes from elongation to contraction upon cooling.

In Fig. 4.11, $\Delta L_{\text{diff}}/L$ of other samples (#2 and #3) are also shown. For all the samples, $\Delta L_{\text{diff}}/L$ takes the maximum at $\sim 100\text{K}$, and decreases and changes their sign upon further cooling.

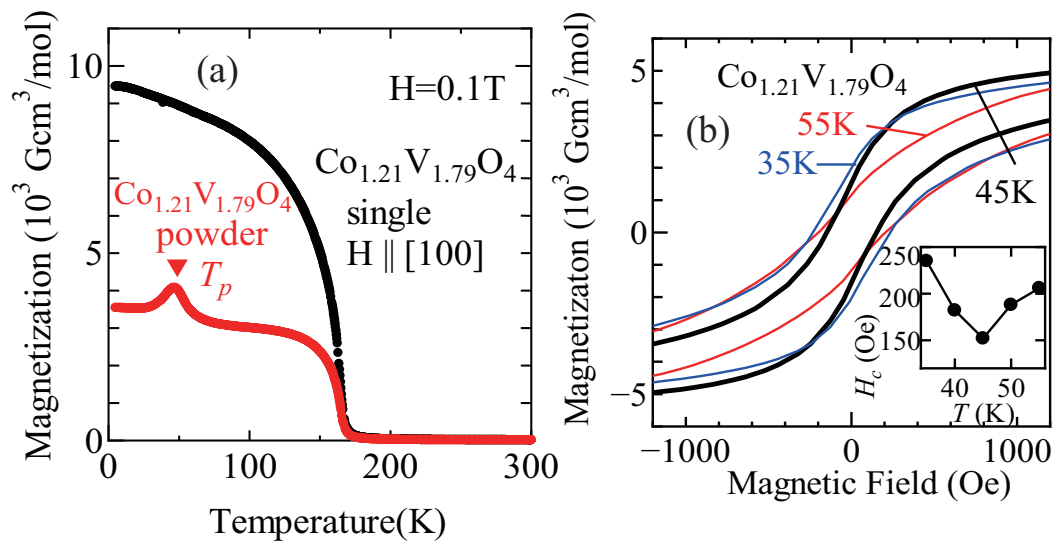


FIGURE 4.9: Reference [94], (a) Temperature dependence of magnetization for a single crystal of CoV_2O_4 (#1) with an applied field of 0.1 T along the $[100]$ axis and that for powder sample obtained by grinding the single crystal. (b) Magnetization vs magnetic field for a ground single crystal of CoV_2O_4 (#1) around $T_p = 45\text{K}$. The inset shows the temperature dependence of coercive field (the magnetic field when magnetization becomes zero).

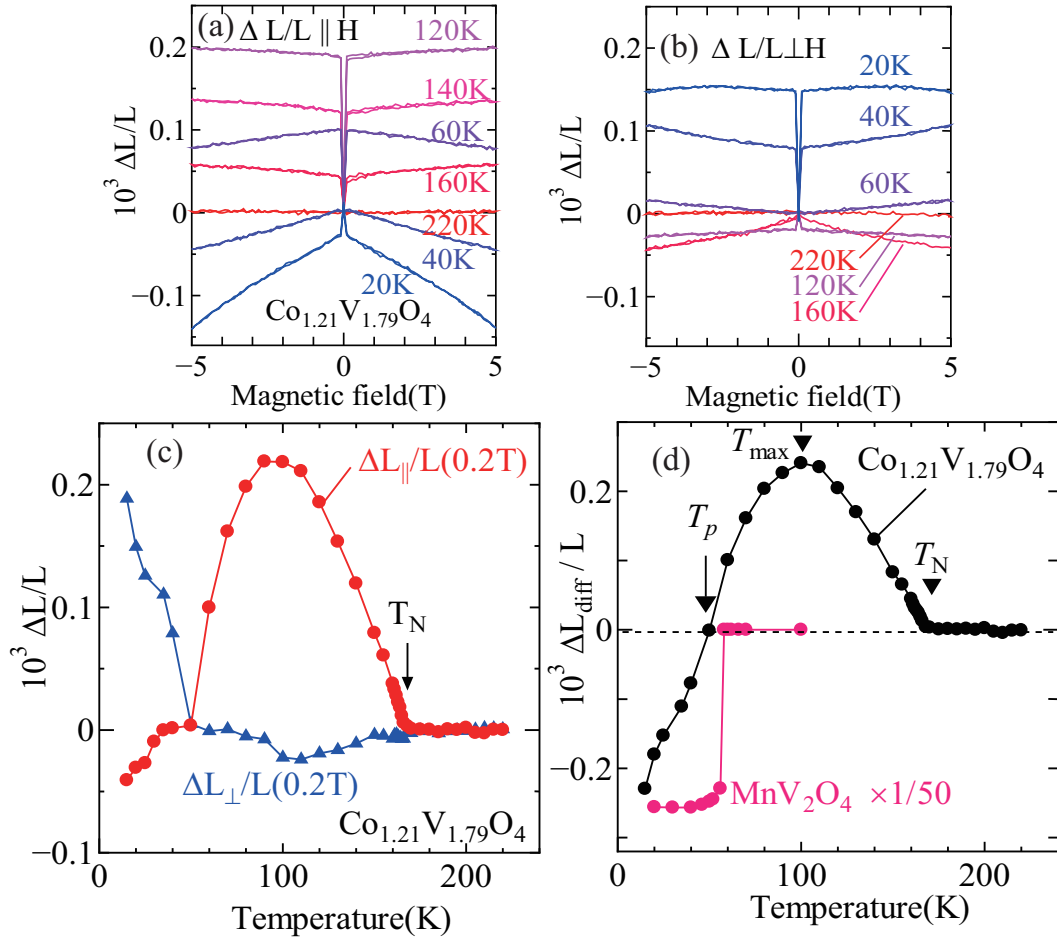


FIGURE 4.10: Reference [94], (a)(b) Magnetic-field (H) dependence of strain ($\Delta L/L$) at various temperatures with (a) $\Delta L/L \parallel H$ and (b) $\Delta L/L \perp H$ for a single crystal of CoV_2O_4 (#2). (c) Temperature dependence of magnetostriction at low- H (difference between $\Delta L/L$ at 0.2 T and that at 0 T, closed symbols) and high- H (difference between $\Delta L/L$ at 5 T and that at 0.2 T, open symbols) with $\Delta L/L \parallel H$ (circles) and $\Delta L/L \perp H$ (triangles) for a single crystal of CoV_2O_4 (#1). (d) Difference between low- H magnetostriction with $\Delta L/L \parallel H$ and that with $\Delta L/L \perp H$ ($\Delta L_{\text{diff}}/L$) as a function of temperature. For comparison $c/a - 1$ obtained by the x-ray diffraction measurement for MnV_2O_4 is also shown.

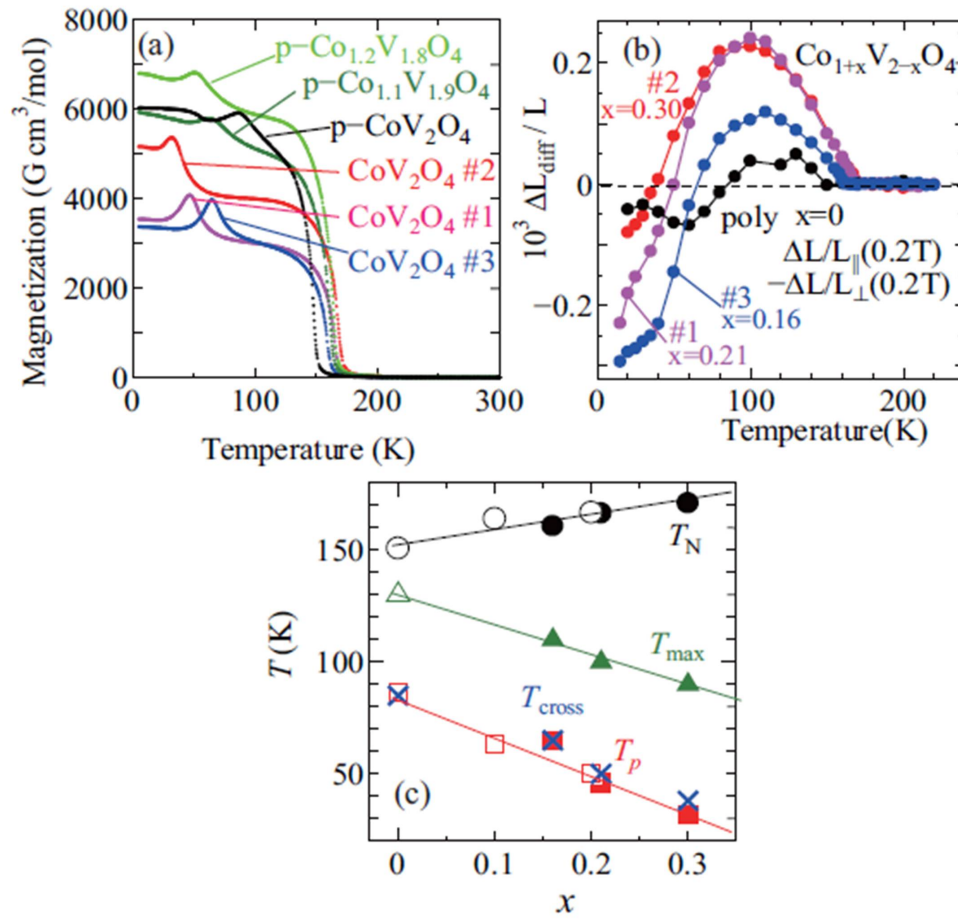


FIGURE 4.11: Reference [94], (a) Temperature dependence of magnetization for ground single crystals (#1, #2, #3) and polycrystalline samples of CoV_2O_4 (b) Difference between low- H magnetostriction with $\Delta L/L \parallel H$ and that with $\Delta L/L \perp H$ ($\Delta L_{\text{diff}}/L$) as a function of temperature for various samples of CoV_2O_4 . (c) x dependence of T_C (circles) and T_P (squares) for single crystals (solid) and polycrystalline (open) samples of $\text{Co}_{1+x}\text{V}_{2-x}\text{O}_4$

4.4.2 Elastic single crystal data

In order to further look at the evolution of the magnetic structure, single crystal diffraction measurements were also performed using the single crystal sample of CoV₂O₄ (#2) using neutron diffractometer E5 at HZB with a neutron wavelength of $\lambda = 2.4 \text{ \AA}$. Structural and magnetic refinements of single crystal data were also carried out using FullProf. Figure 4.12 (a) shows the single crystal refinement of the crystal structure of CoV₂O₄ for 200 K with $Fd\bar{3}m$ space group symmetry. The crystal structure parameters agree with the values obtained using the refinement of powder diffraction data in Table 4.1. The extinction parameter was found by refining the crystal structure from the data obtained at 200 K and used for refinement of other temperatures. Twinning of the single crystal due to the cubic symmetry was considered in the refinement. Single crystal refinement results of crystal and magnetic structure for 10 K is shown in Fig. 4.12 (b). Non-collinear structure as shown in Figure 4.8 gives the best fitting for the data. The canting angle obtained from the refinement for the single crystal is $\sim 10^\circ(2)$, which is smaller than that obtained for the powder sample ($\sim 20^\circ(2)$).

T dependence of the intensity of Bragg peaks for a single crystal of CoV₂O₄ (#2) was measured using neutron wavelength of $\lambda = 2.4 \text{ \AA}$ is shown in Fig. 4.13(a) and (b). Evolution of the intensity of the Bragg peaks agrees with the ferrimagnetic transition at 170 K, which agrees with the magnetization data shown in Fig. 4.9 (a). (400), (202), (313), (511) and (111) peaks all show an anomaly around $T_p=40$ K. Intensities of these Bragg peaks start to level out around 100 K, then decrease and attain a minimum around 40 K. The intensity then again increases at temperatures below 40 K. This behavior is different from the temperature dependence observed in other spinels, MnV₂O₄ and FeV₂O₄. (002) Bragg peak also shows the same transition around 170 K, and increases gradually. Temperature evolution of (002) Bragg peak having non-zero intensity above 170 K may suggest the gradual change of V moments in the non-collinear structure.

In order to find whether or not the anomaly around 40 K is purely a magnetic transition, the temperature evolution of Bragg peaks with higher momentum transfer Q in reciprocal space was measured using neutron wavelength of $\lambda = 0.9 \text{ \AA}$. Bragg peaks with larger Q , (800) with $Q=5.98 \text{ \AA}^{-1}$ and (666) with $Q=7.77 \text{ \AA}^{-1}$ also show the same anomaly observed around $T_p=40$ K as shown in Fig. 4.12(c). Fig. 4.12(d) shows the relative change of intensity of the Bragg peaks. (800) Bragg peak intensity reduces by 70% of its intensity at 100 K and while (666) Bragg peak reduces by 50%. The contribution of these peaks to the magnetic structure is minimal as their magnetic form factor squared is very small (see Fig. 4.12(c)). This indicates that the anomaly of the Bragg peak intensities at T_p is not entirely caused by the change in the magnetic structure. Another possible origin is the change in the extinction effect on the diffraction intensities caused

by a change in mosaic structures [95]. In our current samples such an extinction effect becomes maximum at T_p , where there is a least distortion of the crystal, consistent with the suppression in the intensity of the Bragg peaks at T_p .

From the unpolarized single crystal elastic scattering data it is inconclusive whether the non-collinear magnetic structure transition occurs also at T_C or at lower temperature. In this system magnetic peaks coincide with the nuclear peaks. Thus, a measurement that can directly probe the magnetic contribution of Bragg peaks were necessary such as a polarized neutron scattering experiment which will be discussed in the next section.

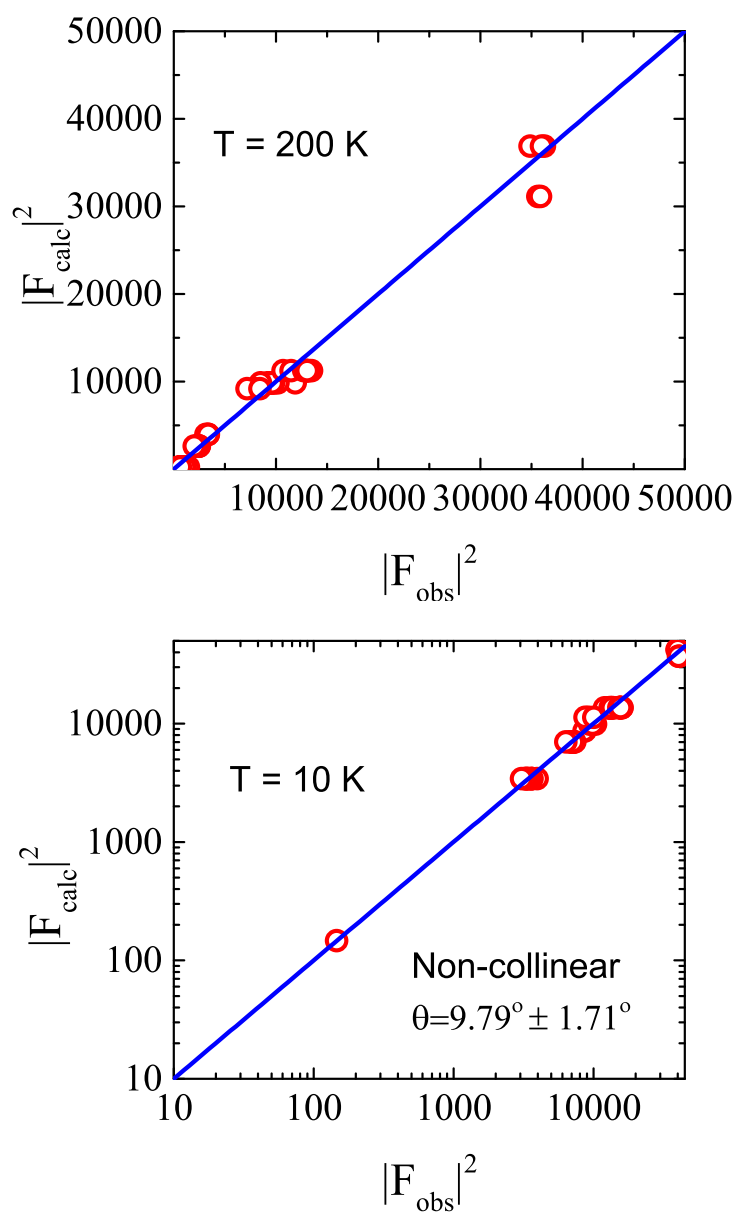


FIGURE 4.12: Single Crystal refinement of CoV_2O_4 at (a) 200 K : Measured (y axis) and calculated (x axis) values for the absolute nuclear structure factors of main peaks. (b) 10 K : Measured (y axis) and calculated (x axis) values for the absolute nuclear + magnetic structure factors of main peaks.

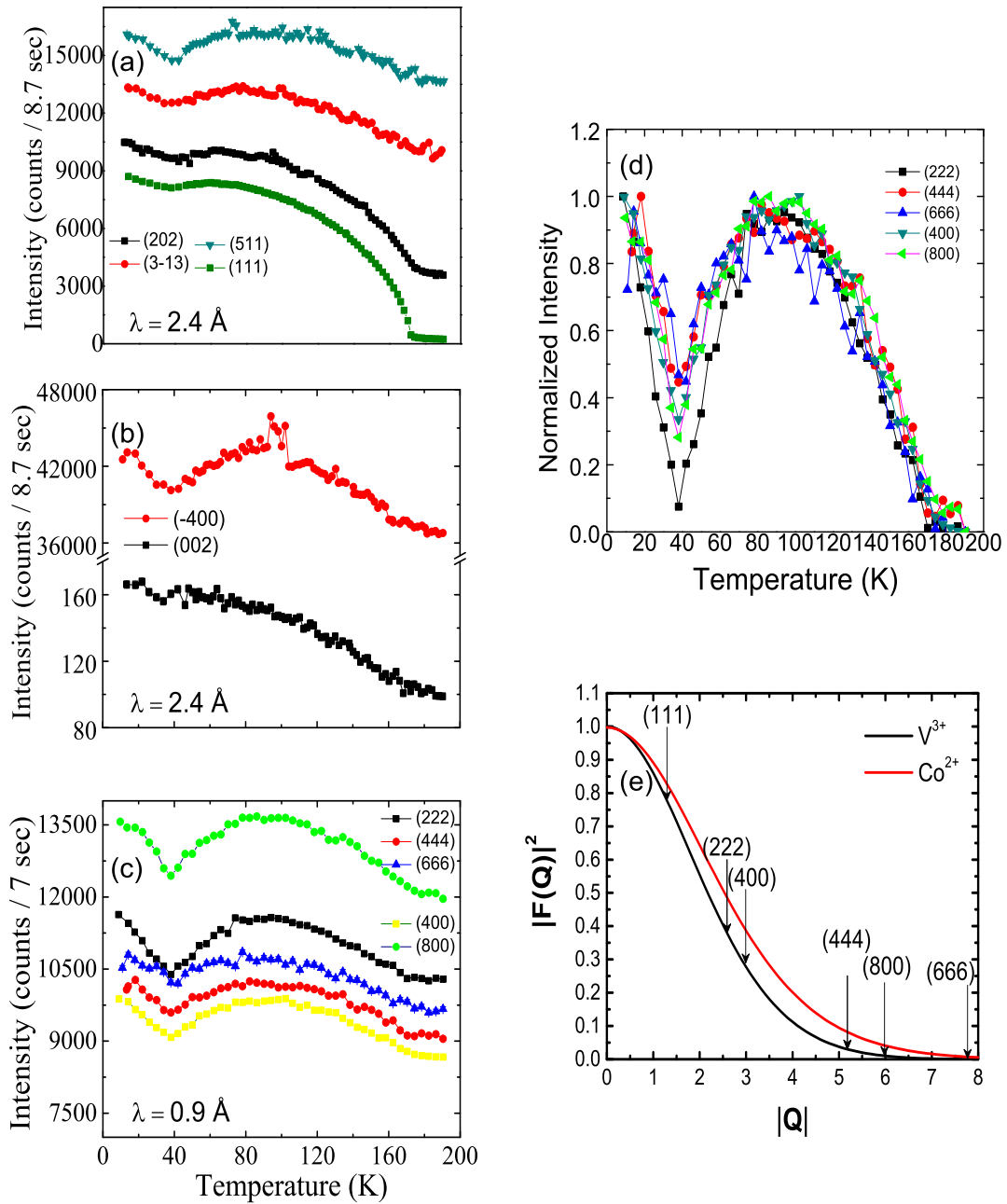


FIGURE 4.13: (a)(b) Temperature dependence of the measured intensity of main magnetic Bragg peaks of a single crystal (#3) of CoV_2O_4 measured using neutron wavelength $\lambda = 2.4 \text{ \AA}$ (c) Temperature dependence of the measured intensity of selected Bragg peaks with large absolute value of momentum transfer Q measured using neutron wavelength $\lambda = 0.9 \text{ \AA}$ (d) Normalized intensity of Bragg peaks shown in Fig. 4.13 (c). Intensity is normalized, by subtracting the value at high T ($> T_C$) and normalized respect to the maximum intensity. (e) Magnetic form factor squared Co^{2+} (blue) and V^{3+} (red) vs absolute value of momentum transfer Q . Corresponding values for selected Bragg peaks are marked with an arrow.

4.4.3 Polarized neutron scattering results

In order to identify the pure magnetic contribution of the Bragg peak intensities, we performed a polarized neutron scattering experiment using the HB-1 Polarized Triple-Axis Spectrometer at HFIR using the single crystal sample (#2). The sample was aligned in HHL plane. Figure 4.14 shows the temperature dependence of the (002) Bragg peak intensity of spin-flip scattering. The spin-flip scattering intensity under a vertical magnetic guide field is proportional to the magnetic scattering intensity from the spin components in the scattering plane. The magnetic structure factor of (002) Bragg peak for atoms in the magnetic unit cell can be written as,

$$F(002)_{mag} = f_V(002)(\vec{S}_{V1} - \vec{S}_{V2} - \vec{S}_{V3} + \vec{S}_{V4}) \\ + f_{Co}(002)\exp(-i\pi/2)(\vec{S}_{Co1} - \vec{S}_{Co2}) \quad (4.1)$$

where $f_V(002)$ and $f_{Co}(002)$ are magnetic form factors of V^{3+} and Co^{2+} respectively.

According to the magnetic structure factor of (002) Bragg peak, only the antiferromagnetic V spin components contribute to the magnetic intensity. Thus observed intensity in Fig. 4 (e) is a direct measurement of the square of the in-plane V spin moment. (002) Bragg peak intensity remains almost zero for temperatures below $T = 90$ K and shows a sudden increase at $T = 90$ K, which indicates that the spin structure changes from collinear ferrimagnetic to non-collinear ferrimagnetic structure as shown in Fig 3 (c). Upon cooling down further, (002) Bragg peak intensity becomes maximum at $T = T_p$. According to the temperature dependence of the magnetic Bragg peaks in Figures 4 (a) and (b) magnetic moments of Co and V are almost saturated at $T = 100$ K. This indicates that the spin moments gradually increase in the collinear ferrimagnetic phase for $100 \text{ K} < T < T_C$ and V spins start canting at $T = 90$ K and achieve maximum canting at $T = T_p$.

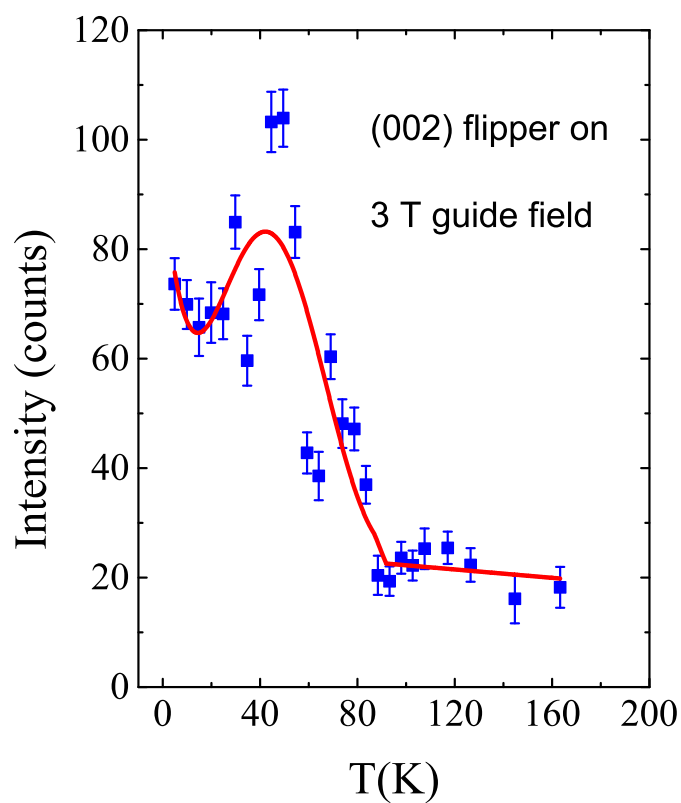


FIGURE 4.14: Temperature dependence of the spin-flip intensity of (002) magnetic Bragg peak of a single crystal (#2) of CoV_2O_4 measured using polarized neutron with a vertical guide field of 3 T. The sample was aligned in HHL plane and a vertical guide field of 3 T was applied along the $[1,-1,0]$ direction. Red line is a guide to the eye.

4.4.4 Orbital glass state

Strain measurements presented in Figure 4.10 and the results of unpolarized and polarized neutron scattering measurements give us important information about the possible orbital state of this system. As discussed in section 3.4.1, MnV₂O₄ undergoes a first order phase transition from cubic to tetragonal phase with $c < a$. This transition was driven by vanadium orbital order with one electron always occupying d_{xy} state and the other electron with alternate occupancy of d_{yz} and d_{zx} states caused by the Kugel-Khomskii type interaction. For FeV₂O₄ the system first orders in a collinear ferrimagnetic state at $T_C=105$ K and then changes to a non-collinear order below $T=70$ K at the first order tetragonal transition. The other vanadium spinels like ZnV₂O₄ and CdV₂O₄ follow the same trend where the V orbitals order with first order transition temperature which drives the system into a long range ordered state.

According to the strain measurements of CoV₂O₄, the system undergoes subtle distortions ($\Delta L_{\text{diff}}/L = c/a - 1$) in the order of 10^{-4} . Immediately below the transition temperature, under a weak field, $\Delta L_{\text{diff}}/L$ increases due to the ordering of Co and V spins and alignment of magnetic domains, representing an elongation along the applied field. The strain data show that distortion attains a maximum around 100 K for single crystal (#1) (~ 90 K for single crystal (#2)) and starts decreasing in a **second order** fashion and changes sign at $T = T_P$. From our polarized neutron scattering data it is found that the V spin structure changes from collinear to non-collinear at $T = 90$ K, that is immediately after the maximum of $\Delta L_{\text{diff}}/L$. The coincidence of temperature that V spins start canting and $\Delta L_{\text{diff}}/L$ becomes maximum indicates a change in orbital state of V ions. However, due to the system's close proximity to the itineracy, orbital degree of freedom incompletely suppress and thus an **orbital glass** state appears below $T \sim 100$ K, which drives the system to non-collinear ferrimagnetic order with relatively small canting angle.

4.5 Magnetic excitations

4.5.1 Inelastic neutron scattering data

To understand the magnetic excitations and exchange interactions of the system, a series of inelastic neutron scattering experiments were performed.

A cold neutron triple axis experiment is performed on CoV₂O₄ single crystal sample #2 to understand the low energy dispersions of the system. For MnV₂O₄, a gapped excitation of ~ 2 meV was observed and gap closing is reported at the non-collinear to

collinear transition[68, 89]. Figure 4.15 (a) shows a contour map of inelastic neutron scattering intensity measured at cold neutron triple axis spectrometer (CTAX) at HFIR, ORNL. The horizontal axis is momentum transfer \vec{Q} along [HH0] direction and the vertical axis is energy transfer $\hbar\omega$. A dispersive mode centered around the zone center $\vec{Q} = (220)$ was observed. Figure 4.15 (b) shows the energy scans measured at 5K, at $Q = (220)$. Our data clearly shows a gapped excitation centered around ~ 2 meV.

To understand the higher energy magnetic excitations and detailed spinwave dispersion of the system, a thermal neutron triple axis experiment at the HB1 thermal triple axis spectrometer at HFIR and a time of flight neutron scattering experiment at the Wide Angular-Range Chopper Spectrometer (ARCS) were also performed. As shown in Figure 4.16, along [HH0] direction a highly dispersive mode extending up to ~ 35 meV was observed. Energy scans at $\vec{Q} = (220)$ as shown in Figure 4.17 (b) show four possible spin wave branches with peaks at $\hbar\omega = 2$ meV, 6 meV, 15 meV and 22 meV.

Inelastic neutron scattering data obtained from the ARCS spectrometer also confirm the dispersion we observed using the HB1 triple axis spectrometer as shown in Figure 4.18. Figure 4.18 shows the full dispersion spectrum across several Brillouin zones along a few selected directions in the reciprocal space. Magnetic excitations are only observed up to 40 meV. We also collected data using incident energy with 150 meV to confirm this.

These magnetic excitations are similar to the case of MnV_2O_4 , however, it is more dispersive with a greater band width compared to MnV_2O_4 . A probable reason for that is the interaction between Co and V atoms in CoV_2O_4 is higher than the interaction between Mn and V in MnV_2O_4 , which will be discussed more in light of linear spinwave calculations we performed.

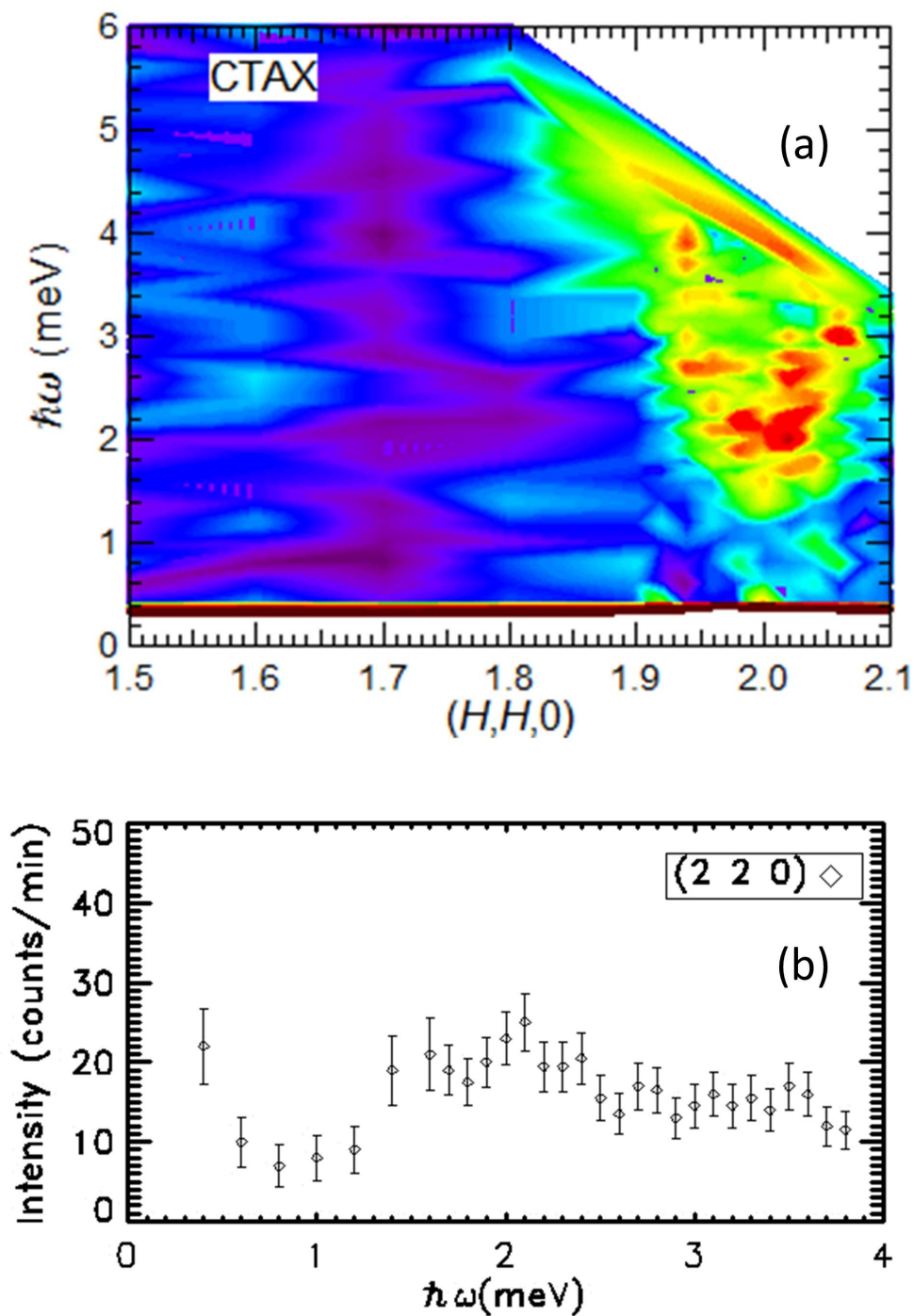


FIGURE 4.15: Inelastic neutron scattering data measured using cold triple axis spectrometer CTAX at HFIR, ORNL of CoV_2O_4 single crystal sample #2 (a) The contour map of inelastic neutron scattering intensity in $(HH0)$ direction-E space (b) Energy scan at (220) position

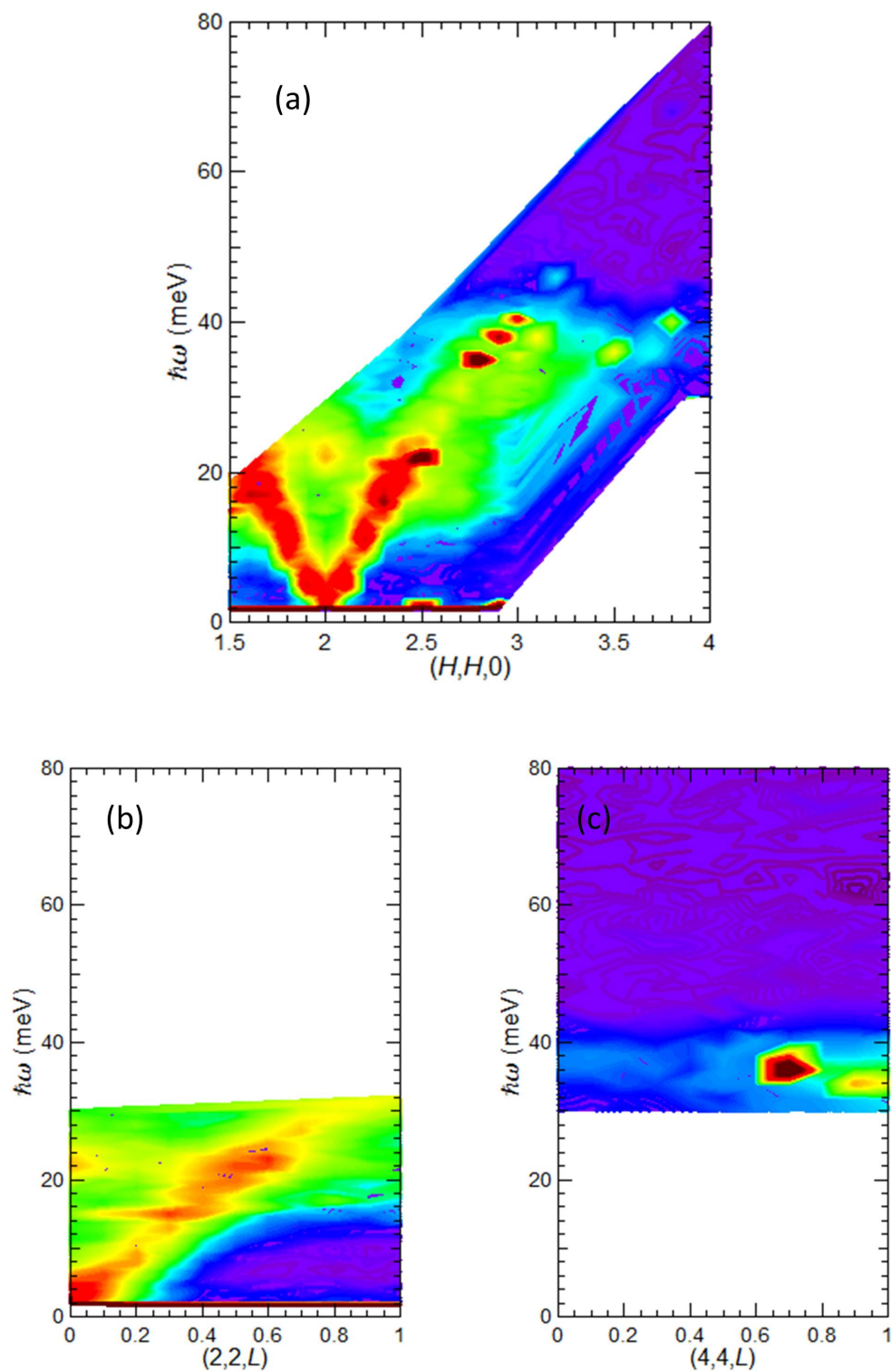


FIGURE 4.16: Inelastic neutron scattering data measured using polarized triple axis spectrometer HB1 at HFIR, ORNL of CoV_2O_4 single crystal sample #2. The contour map of inelastic neutron scattering intensity in (a) $(HH0)$ direction-E space (b) $(22L)$ direction-E space (c) $(44L)$ direction-E space

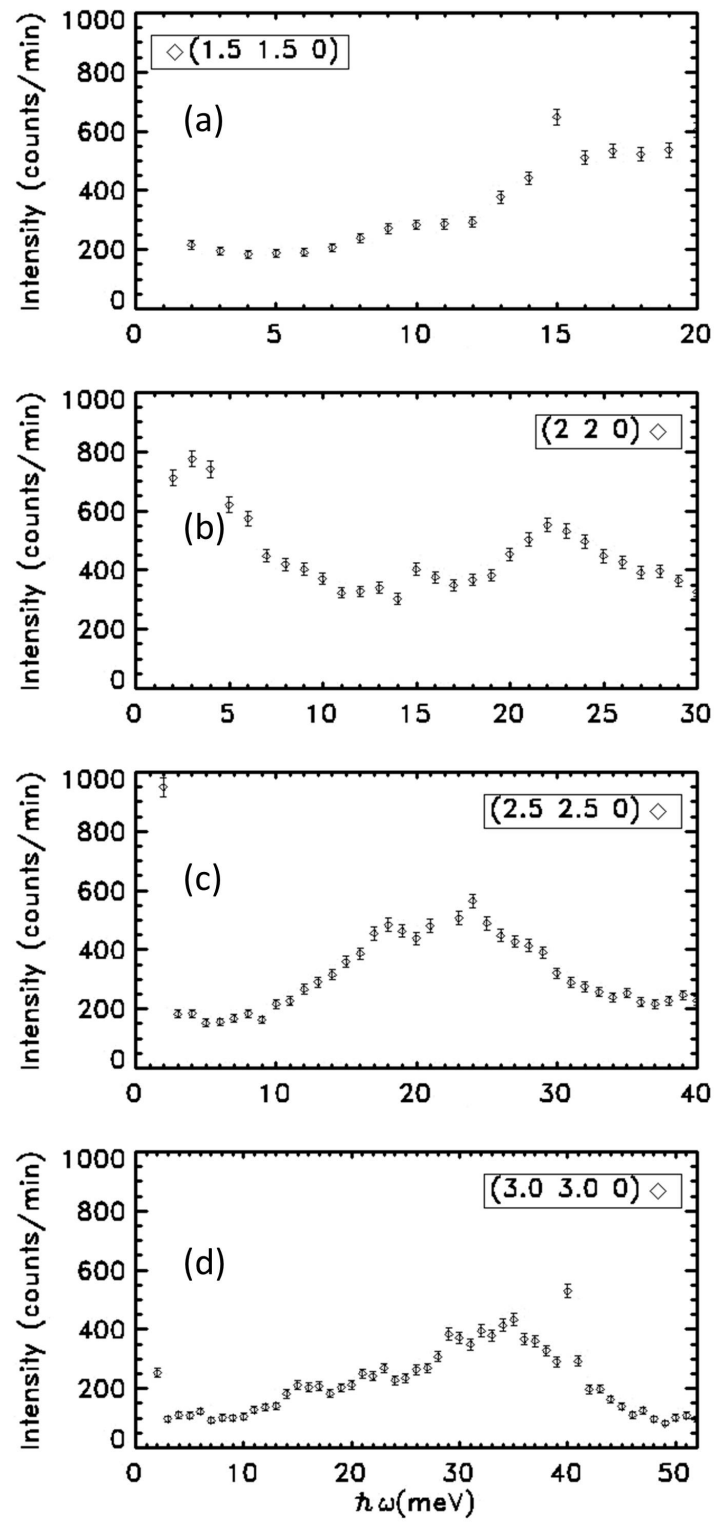


FIGURE 4.17: Inelastic neutron scattering data measured using polarized triple axis spectrometer HB1 at HFIR, ORNL of CoV₂O₄ single crystal sample #2. Constant Q scans along energy transfer, at (a) (1.5 1.5 0) (b) (2 2 0) (c) (2.5 2.5 0) (d) (3 3 0)

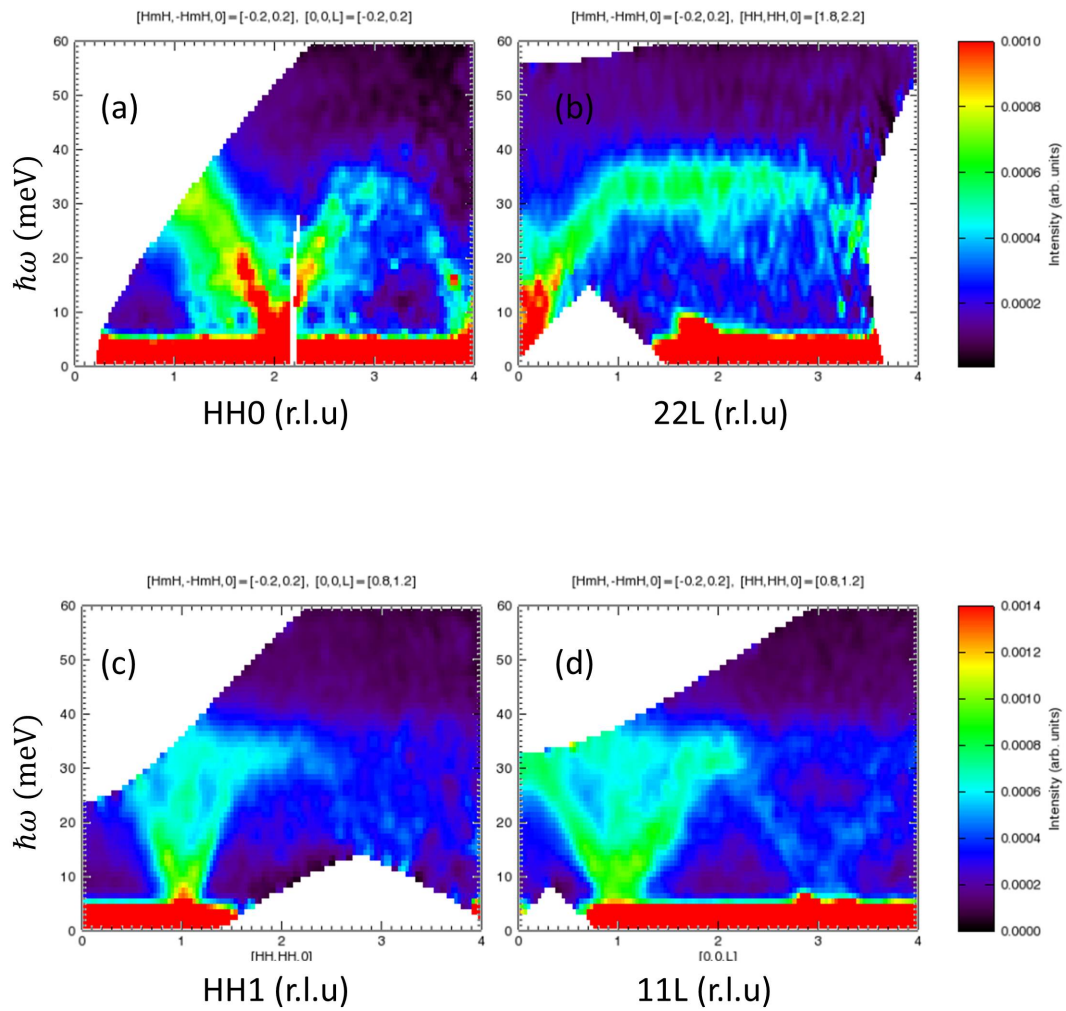


FIGURE 4.18: Time of flight inelastic neutron scattering data of CoV_2O_4 single crystal sample #2 measured using ARCS spectrometer. Q - E maps, (a) (HH0) (b) (22L) (c) (HH1) (d) (11L) directions

4.5.2 Linear spinwave calculation

In order to understand the nature of magnetic excitations and coupling between spin and orbital degree of freedom, linear spinwave calculations were performed.

Following spin Hamiltonian is used to calculate and model the spinwave dispersion and intensities,

$$\mathcal{H} = \sum_{\langle ij \rangle} J_{ij} S_i \cdot S_j + \sum_i D_i (\hat{d}_i \cdot S_i)^2 \quad (4.2)$$

J_{ij} is the nearest neighbor interaction between the magnetic ions and D_i is the single ion anisotropy of magnetic ions. \hat{d}_i is the direction of the single ion anisotropy. Three different nearest neighbor interaction in this system is defined. Spin interaction between V atoms in-plane (ab plane when ferrimagnetic moments are along c -direction) J_{VV} , out of plane interaction J'_{VV} are shown in Figure 4.19 (a). The non-collinear magnetic structure found by refining the diffraction data at 5 K is used in the calculations. As shown in Figure 4.19 (c), in one tetrahedron two spins point inward to the center while other two spins point outward, which is usually defined as 2-in-2-out structure. Although the canting angle is small compared to other spinel vanadates, a small antiferromagnetic component along [110] direction forms chains, with chain interaction J_{VV} and inter chain interaction J'_{VV} . Although the overall crystal structure remains cubic, we found from strain measurements that CoV₂O₄ undergoes a second order type distortion in the order of 10^{-4} , which can lead to an orbital glass state. Thus in our spinwave simulations we consider both cases where $J_{VV} \neq J'_{VV}$ and $J_{VV} = J'_{VV}$. In addition to interaction between V ions, the interaction between Co and V ions also plays a central role in this system, which we define as J_{CoV} as shown in Figure 4.19 (b). Single ion anisotropy direction \hat{d}_i is defined as the local [111] direction in the octahedral environment for V ions and along c direction for Co ions.

TABLE 4.4: Exchange constants and single ion anisotropy parameter used for each spinwave model in Figure 4.20 for the Hamiltonian in equation 4.2

Model	J_{CoV}	J_{VV}	J'_{VV}	D_{Co}^c	$D_V^{[111]}$
Model 1	3.2	1.0	1.0	-0.03	-0.55
Model 2	3.2	1.8	0.6	-0.03	-0.5
Model 3	3.2	3.0	-1.1	-0.03	-0.55

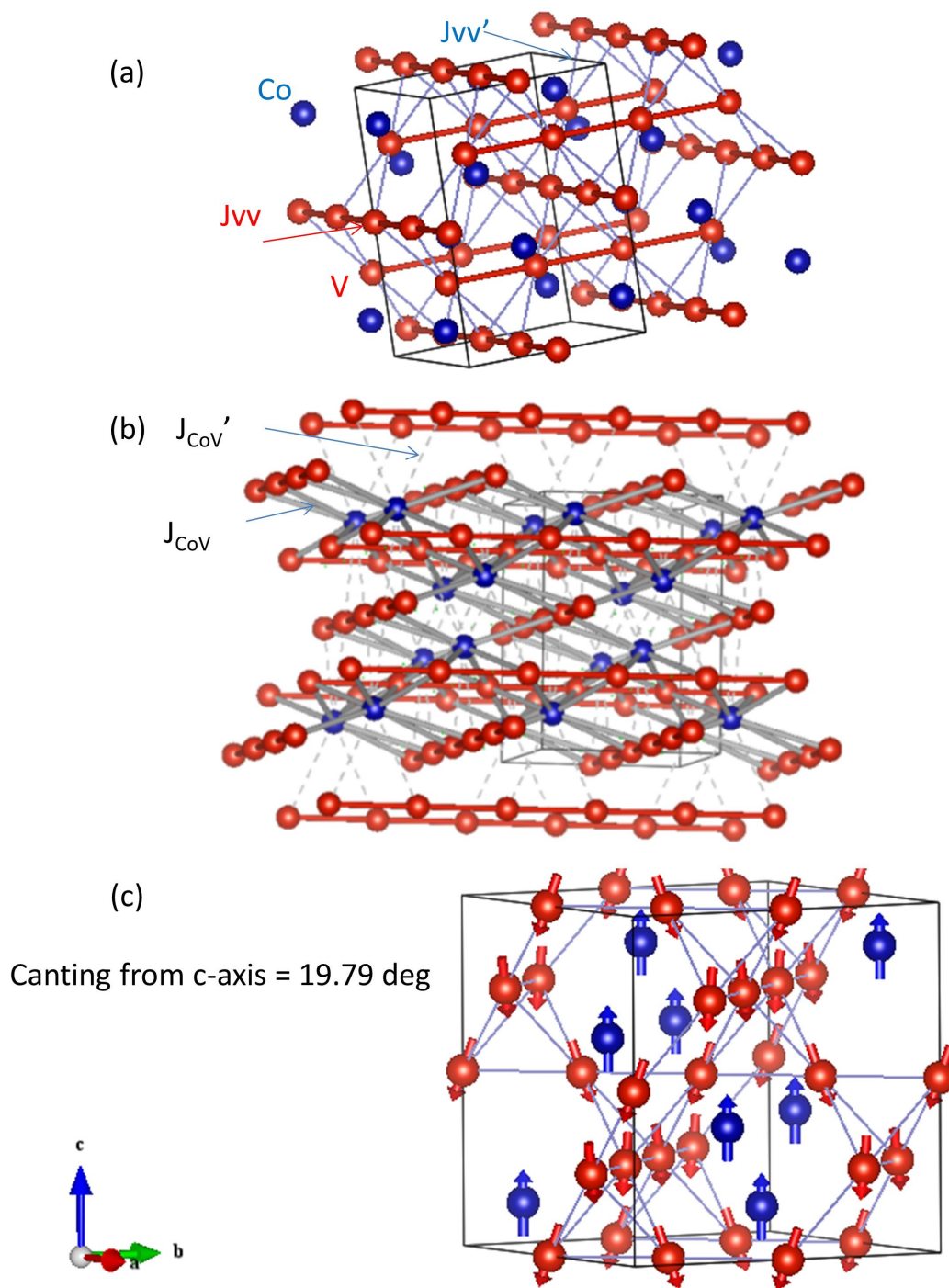


FIGURE 4.19: (a), (b) Spin interactions of CoV_2O_4 spinel (c) Magnetic structure used for the linear spinwave calculations. Co spins are along c -axis and V spins are pointed along $-c$ axis but canted from $-c$ axis by 19.79° towards $[110]$ direction in ab plane

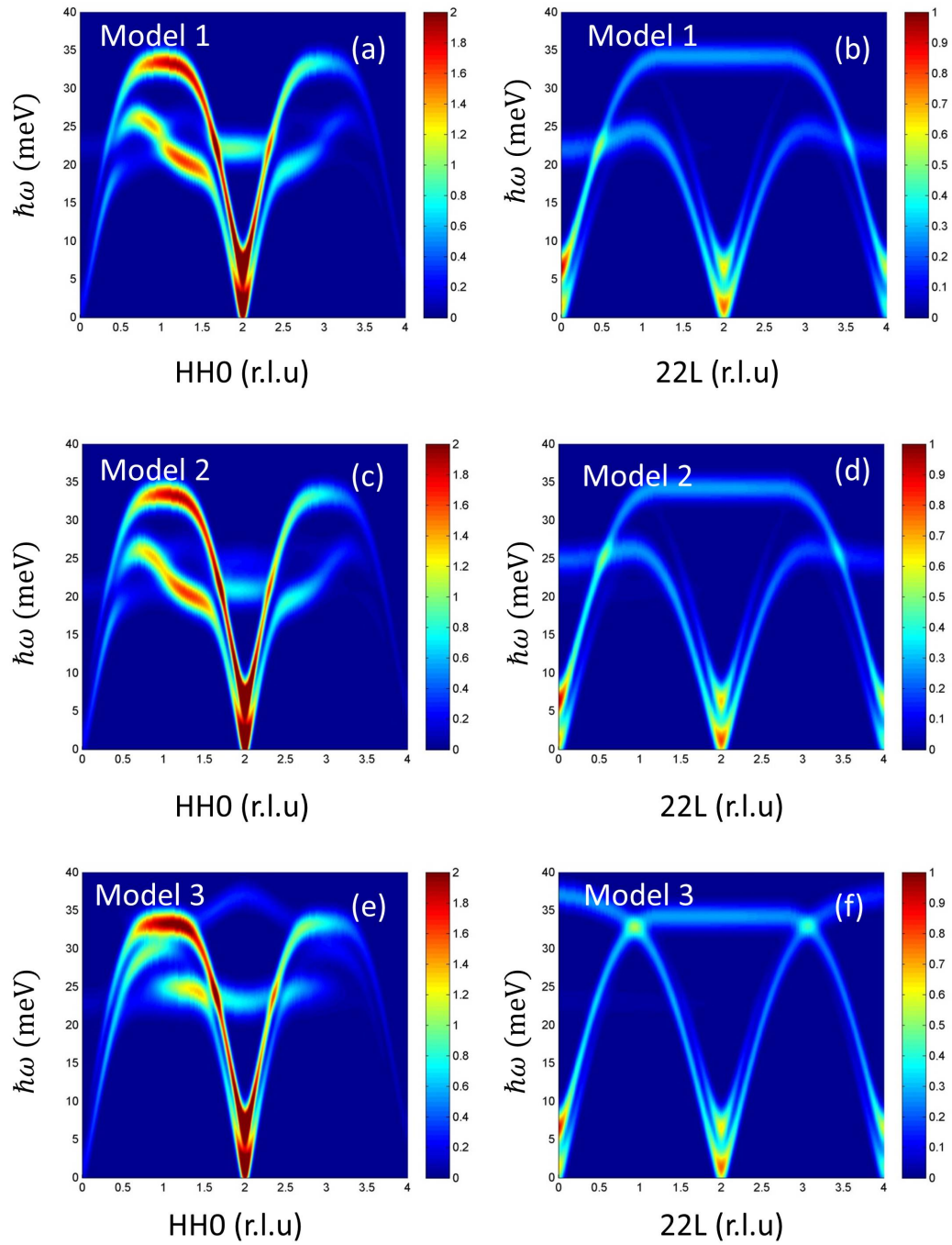


FIGURE 4.20: Linear spin wave calculation to simulate the observed spinwave excitations of CoV_2O_4 using the spin structure in Figure 4.19 (c) for three different models with parameters as in Table 4.4.

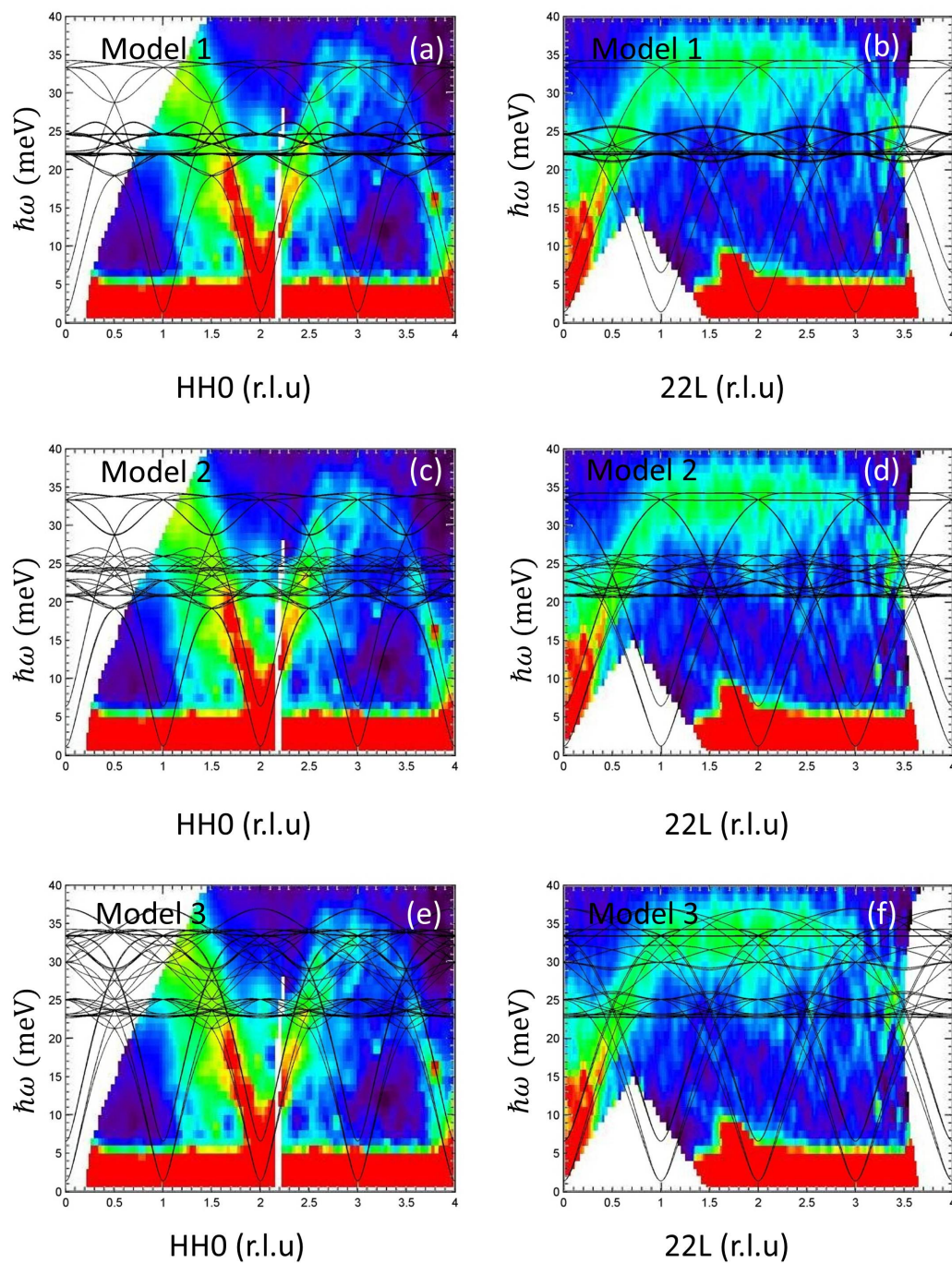


FIGURE 4.21: Calculated spinwave dispersions for each model superimposed on top of the inelastic neutron scattering data measured using single crystal #2 of CoV_2O_4 at ARCS time of flight spectrometer

In this discussion about the simulation of spinwave excitations three different models were considered. Exchange constants and single ion anisotropy values for each model are summarized in Table 4.4. According to these models Co-V interaction is more enhanced in CoV₂O₄ compared to Mn-V interaction in MnV₂O₄ which was ~ 1.2 meV [89]. In all the three models that can describe our inelastic data, interaction between Co and V is the strongest. As discussed by J. Ma et al. [89], enhancement of interaction between Co and V compared to other spinels may be due to the lowering of t_{2g} orbitals of Co, which reduces the energy gap between the corresponding t_{2g} orbitals of V and Co.

CoV₂O₄ has a cubic structure thus magnetic domains exist. In other words in the calculations to correctly calculate the observed intensity, for example along (HH0) direction, need to superimpose the dispersion and intensities along (HH0), (0HH) and (0H0) directions. However, the presence of domains does not affect the spin wave energies at high symmetry points, such as zone center and zone boundaries [67]. Figure 4.20 shows the calculated contour map of neutron scattering intensity for each model along (HH0) and (22L) directions considering the magnetic domains in cubic crystal structure. The spinwave dispersions are also calculated and over plotted on top of the experimental contour map of neutron scattering intensity measured at ARCS using single crystal #2 of CoV₂O₄ as shown in Figure 4.21.

The first model, referred as Model 1 describes the simulation when the in-plane J_{VV} and out-of plane J'_{VV} are equal. This is similar to the Model Hamiltonian proposed in reference [89], where they conclude that the orbital order is completely suppressed and thus structural isotropy with $a = b = c$ and magnetic isotropy with $J_{VV} = J'_{VV}$ is enhanced due to close proximity to the itineracy in this system. The calculated intensity and dispersion fairly agree with the measured data.

The Model 2 and Model 3 describe the situation where $J_{VV} \neq J'_{VV}$. In Model 2, the intensity is very similar to Model 1 except the intensity around $E \sim 22$ meV at (220) position in Q , where Model 2 has a broad spectrum extending from 20 meV to 25 meV while Model 1 has a sharp peak at 22 meV. In Model 3 J'_{VV} is ferromagnetic. Although the overall intensity matches well in this model, the additional modes observed above 33 meV along both (HH0) and (22L) were not visible in the experimental data.

It is difficult to distinguish Model 1 and Model 2 from the current experimental data. Considering the systems close proximity to itineracy, V-V interaction may be isotropic in the tetrahedra with $J_{VV} = J'_{VV}$ [89]. However, an energy cut at $Q = (220)$, excitation around ~ 22 meV is broader than the simulated intensity of Model 1.

4.6 Summary and Conclusions

In this chapter, the magnetic, structural and orbital properties of spinel CoV₂O₄ were studied. Having the smallest V-V separation for V spinels, CoV₂O₄ resides close to the itinerant electron limit. From our unpolarized and polarized elastic neutron scattering data we found that system changes from collinear to non-collinear ferrimagnetic phase at $T = 90$ K. Our collaboration study about magnetostriction measurements indicates that a subtle distortion of the crystal along the direction of magnetization, $\Delta L/L \sim 10^{-4}$, varies from elongation to contraction in a second order fashion upon cooling with a maximum elongation of the crystal at around 100 K. The collinear to noncollinear transition at $T \sim 90$ K, coincides with where the elongation of the crystal is maximized, indicating a possible orbital change of the system around $T \sim 100$ K. Probably due to the close proximity to the itineracy, the orbital order is incompletely suppressed and the crystal undergoes second order type structural phase transition to a phase with $c < a$ at low temperature with a subtle distortion in the order of $\sim 10^{-4}$. These results imply the existence of a glassy orbital state for the Vt_{2g} states in CoV₂O₄.

Inelastic neutron scattering measurements were performed and found a gapped (~ 2 meV) dispersive excitation which extends up to 35 meV. By performing linear spinwave calculations few different models for the spin Hamiltonian were proposed which can qualitatively represent the observed dispersions and intensity.

Appendix A

Linear Spin wave calculation of Kagome Antiferromagnet

As an example for Linear Spin Wave calculation, the calculation for the Kagome + Triangular Lattice is presented. The problem under study was the Compound $\text{Co}_2(\text{OD})_3\text{Cl}$ [38]. Refinement of Powder Diffraction data using FullProf shows a $q=0$ Umbrella like structure. Comprehensive step by step LSW calculation is provided here.

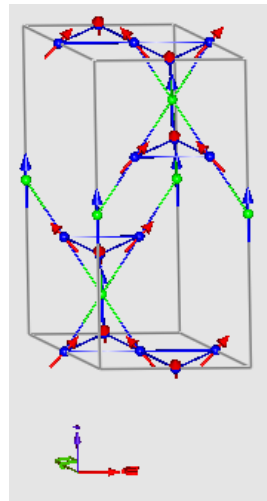


Figure A1: Crystal Structure

The nuclear unit cell of this structure has 12 Co Atoms, 3 in the Triangular Plane and 4 In the Kagome Plane.

The Primitive Unit cell of this contains 4 atoms, and it is rhombohedral with lattice vectors given by,

$$a_1 = \left(\frac{a}{2}, \frac{\sqrt{3}}{6}a, \frac{c}{3} \right)$$

$$a_2 = \left(-\frac{a}{2}, \frac{\sqrt{3}}{6}a, \frac{c}{3} \right)$$

$$a_3 = \left(0, -\frac{a}{\sqrt{3}}, \frac{c}{3} \right)$$

In each primitive unit cell, there are 4 spins of $3/2$, which are located at

$$\tau_A = \left(\frac{a}{4}, \frac{a\sqrt{3}}{4}, 0 \right)$$

$$\tau_B = (0,0,0)$$

$$\tau_C = (a/2,0,0)$$

$$\tau_D = \left(\frac{a}{4}, \frac{a\sqrt{3}}{12}, \frac{c}{6} \right)$$

A,B,C Spins are in the Kagome plane while D Spin is in the Triangular Plane.

As a start we consider a Model Hamiltonian in the Form,

$$H_{kagome} = \sum_{NN(i<j)} J_1 S_i \cdot S_j$$

$$H_{interplane} = \sum_{NN(i<j)} J_2 S_i \cdot S_j$$

$$H = H_{kagome} + H_{interplane}$$

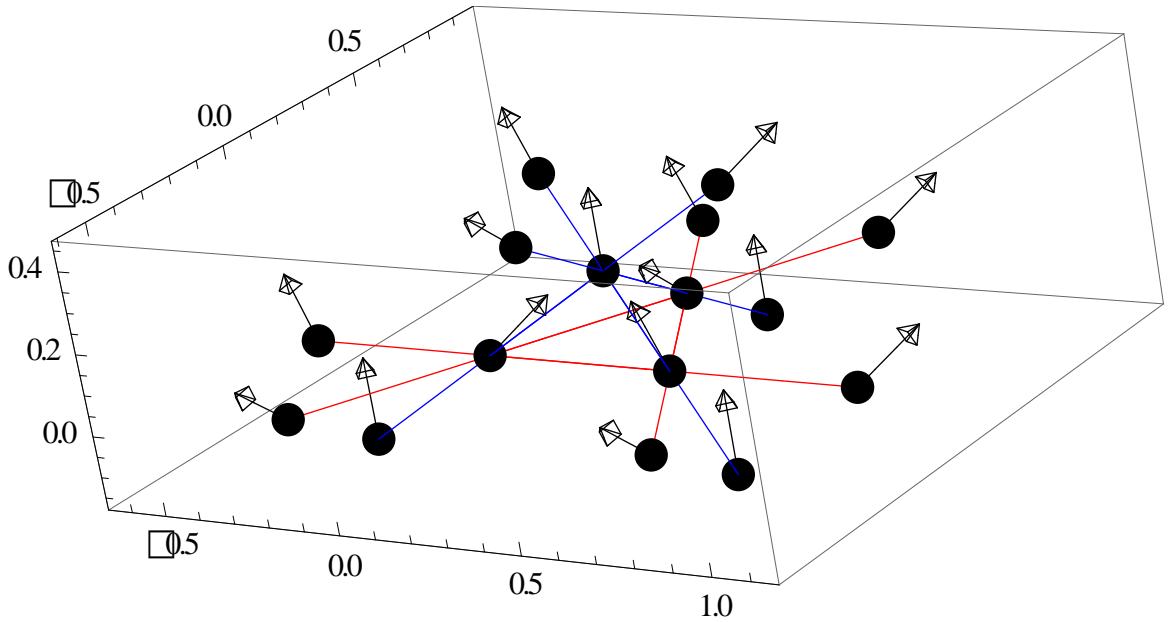


Figure A2 : Nearest neighbor interactions

All the nearest neighbor interactions within the primitive unit cell is shown as in Figure 2. Red lines are for $J_1 (>0)$ Antiferromagnetic Interactions in the kagome plane. $J_2 (<0)$ Interlayer interaction between kagome and triangular plane are shown in blue.

Note that for every kagome spin, there are four J_1 interactions and two J_2 interactions while for spin in Triangular plane there are six J_2 interactions.

We denote Spins in the Kagome plane as A,B,C Spins and Spins in the Triangular Plane as Spin D.

We use the method of Holstein – Primakoff to represent each spin as bosonic operators,

Starting with Spin D, since the spin is directing towards z axis,

$$S_D^z = S - d^\dagger d$$

$$S_D^x = \sqrt{\frac{S}{2}} (d + d^\dagger)$$

$$S_D^y = i\sqrt{\frac{S}{2}} (d^\dagger - d)$$

To find Holstein – Primakoff operators for Spins A,B,C in the kagome plane, we use simple rotations.

Rotate by θ around x axis

$$S_A^z = i\sqrt{\frac{S}{2}} (a^\dagger - a)\sin(\theta) + (S - a^\dagger a)\cos(\theta)$$

$$S_A^x = \sqrt{\frac{S}{2}} (a + a^\dagger)$$

$$S_A^y = i\sqrt{\frac{S}{2}} (a^\dagger - a)\cos(\theta) - (S - a^\dagger a)\sin(\theta)$$

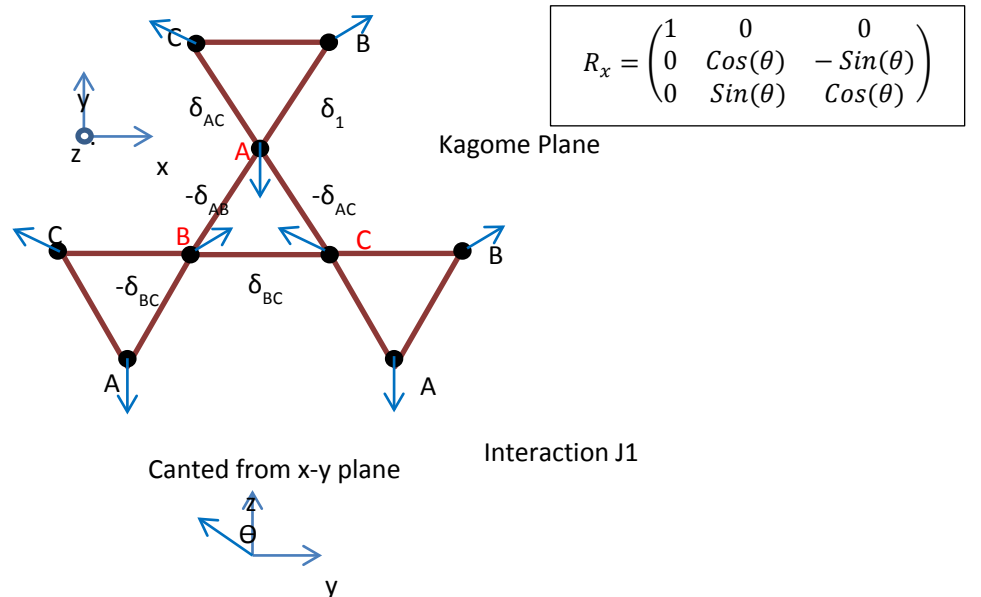


Figure A3 : Spin arrangement in Kagome plane

For Spin B – Rotate by θ around x axis + Rotate by $\frac{2\pi}{3}$ around z axis

$$R_z = \begin{pmatrix} \cos(-\frac{2\pi}{3}) & -\sin(\frac{2\pi}{3}) & 0 \\ \sin(\frac{2\pi}{3}) & \cos(-\frac{2\pi}{3}) & 0 \\ 0 & 0 & 1 \end{pmatrix} \quad R_x = \begin{pmatrix} 1 & 0 & 0 \\ 0 & \cos(\theta) & -\sin(\theta) \\ 0 & \sin(\theta) & \cos(\theta) \end{pmatrix}$$

$$S_B^z = (S - b^\dagger b) \cos(\theta) + \sqrt{\frac{S}{2}} i (b^\dagger - b) \sin(\theta)$$

$$S_B^x = -\sqrt{\frac{S}{2}} \left(\frac{1}{2} (b + b^\dagger) + \frac{\sqrt{3}}{2} i (b^\dagger - b) \cos(\theta) \right) + \frac{\sqrt{3}}{2} (S - b^\dagger b) \sin(\theta)$$

$$S_B^y = \sqrt{\frac{S}{2}} \left(\frac{\sqrt{3}}{2} (b + b^\dagger) - \frac{1}{2} i (b^\dagger - b) \cos(\theta) \right) + \frac{1}{2} (S - b^\dagger b) \sin(\theta)$$

For Atom C – Rotate by θ around x axis + Rotate by $-\frac{2\pi}{3}$ around z axis

$$S_C^z = (S - c^\dagger c) \cos(\theta) + \sqrt{\frac{S}{2}} i (c^\dagger - c) \sin(\theta)$$

$$S_C^x = \sqrt{\frac{S}{2}} \left(-\frac{1}{2} (c + c^\dagger) + \frac{\sqrt{3}}{2} i (c^\dagger - c) \cos(\theta) \right) - \frac{\sqrt{3}}{2} (S - c^\dagger c) \sin(\theta)$$

$$S_C^y = -\sqrt{\frac{S}{2}} \left(\frac{\sqrt{3}}{2} (c + c^\dagger) + \frac{1}{2} i (c^\dagger - c) \cos(\theta) \right) + \frac{1}{2} (S - c^\dagger c) \sin(\theta)$$

All spins are now relative to a Global coordinate system.

We take simple products to find the dot product between each operators and use commutation rules of bose operators to simplify.

Consider only quadratic terms + constant terms in bose operators.

i.e. - Linear term does not contribute to Spin waves and also higher order terms

$$\begin{aligned}
S_A^x S_B^x &= -\frac{s}{2} \frac{1}{2} (a + a^\dagger)(b + b^\dagger) - \frac{s\sqrt{3}}{2} \frac{1}{2} i(a + a^\dagger)(b^\dagger - b)\cos(\theta) \\
S_A^y S_B^y &= -\frac{1}{2} S^2 \sin^2(\theta) + \frac{s}{2} \frac{1}{2} (a^\dagger - a)(b^\dagger - b) \cos^2(\theta) \\
&\quad + \frac{s\sqrt{3}}{2} \frac{1}{2} i(a^\dagger - a)(b + b^\dagger) \cos(\theta) + \frac{1}{2} S (a^\dagger a + b^\dagger b) \sin^2(\theta) \\
S_A^z S_B^z &= S^2 \cos^2(\theta) - \frac{s}{2} (a^\dagger - a)(b^\dagger - b) \sin^2(\theta) - S (a^\dagger a + b^\dagger b) \cos^2(\theta)
\end{aligned}$$

Expanding terms and keeping only constant and second order terms,

$$\begin{aligned}
S_A \cdot S_B &= -\frac{1}{2} S^2 (3 \sin^2(\theta) - 2) + \frac{1}{2} S (a^\dagger a + b^\dagger b) (3 \sin^2(\theta) - 2) \\
&\quad - \frac{s}{4} (3(a^\dagger b^\dagger + ab) \sin^2(\theta) + (ab^\dagger + a^\dagger b)(2 - 3 \sin^2(\theta))) \\
&\quad + S \frac{\sqrt{3}}{2} i (a^\dagger b - ab^\dagger) \cos(\theta)
\end{aligned}$$

Similarly,

$$\begin{aligned}
S_A \cdot S_C &= -\frac{1}{2} S^2 (3 \sin^2(\theta) - 2) + \frac{1}{2} S (a^\dagger a + c^\dagger c) (3 \sin^2(\theta) - 2) \\
&\quad - \frac{s}{4} (3(a^\dagger c^\dagger + ac) \sin^2(\theta) + (ac^\dagger + a^\dagger c)(2 - 3 \sin^2(\theta))) \\
&\quad + S \frac{\sqrt{3}}{2} i (ac^\dagger - a^\dagger c) \cos(\theta) \\
S_B \cdot S_C &= -\frac{1}{2} S^2 (3 \sin^2(\theta) - 2) + \frac{1}{2} S (b^\dagger b + c^\dagger c) (3 \sin^2(\theta) - 2) \\
&\quad - \frac{s}{4} (3(b^\dagger c^\dagger + bc) \sin^2(\theta) + (bc^\dagger + b^\dagger c)(2 - 3 \sin^2(\theta))) \\
&\quad + S \frac{\sqrt{3}}{2} i (b^\dagger c - bc^\dagger) \cos(\theta)
\end{aligned}$$

Here I list out properties of Fourier Transform Operators,

Fourier Transform of Bose Operators are defined by,

- $a = N^{-\frac{1}{2}} \sum e^{-i k \cdot r_a} a_k$ $a^\dagger = N^{-\frac{1}{2}} \sum e^{i k \cdot r_a} a_k^\dagger$

- $a^\dagger a = N^{-\frac{1}{2}} \sum e^{i k' r_a} a_{k'}^\dagger, N^{-\frac{1}{2}} \sum e^{-i k r_a} a_k = \sum_k a_k^\dagger a_k$
- $ab^\dagger = N^{-\frac{1}{2}} \sum e^{-i k r_a} a_k \cdot N^{-\frac{1}{2}} \sum e^{i k' r_b} b_{k'}^\dagger = \sum_k a_k b_k^\dagger e^{i k \cdot \delta_l}$
- $a^\dagger b = N^{-\frac{1}{2}} \sum e^{i k r_a} a_k \cdot N^{-\frac{1}{2}} \sum e^{-i k' r_b} b_{k'}^\dagger = \sum_k a_k b_k^\dagger e^{-i k \cdot \delta_l}$
- $ab = N^{-\frac{1}{2}} \sum e^{-i k r_a} a_k \cdot N^{-\frac{1}{2}} \sum e^{-i k' r_b} b_{k'}^\dagger = \sum_k a_k b_{-k}^\dagger e^{i k \cdot \delta_l}$
- $a^\dagger b^\dagger = N^{-\frac{1}{2}} \sum e^{i k r_a} a_k \cdot N^{-\frac{1}{2}} \sum e^{i k' r_b} b_{k'}^\dagger = \sum_k a_k b_{-k}^\dagger e^{-i k \cdot \delta_l}$

Now we first consider all the interaction in the kagome plane. Note that since we are counting twice, finally we have to divide by two to get the correct terms.

Consider A atoms within the primitive unit cell as in figure 3. (Atoms within the unit cell are in Red)

Spin A will have NN interaction J_1 with two B spins and two C spins as in the figure. Therefore, we consider each interaction, Fourier Transform it, and then simplify using the properties outlined above.

$$\begin{aligned}
S_A \cdot S_{B1} + S_A \cdot S_{B2} &= -S^2(3 \sin^2(\theta) - 2) + S \sum_k (a_k^\dagger a_k + b_k^\dagger b_k)(3 \sin^2(\theta) - 2) \\
&\quad - \frac{3S}{2} \sin^2(\theta) \sum_k (a_k^\dagger b_{-k}^\dagger + a_k b_{-k}) \cos k \cdot \delta_2 \\
&\quad - \frac{S}{2} (2 - 3 \sin^2(\theta)) \sum_k (a_k b_k^\dagger + a_k^\dagger b_k) \cos k \cdot \delta_2 \\
&\quad + S\sqrt{3}i \cos(\theta) \sum_k (a_k^\dagger b_k - a_k b_k^\dagger) \cos k \cdot \delta_2
\end{aligned}$$

$$\begin{aligned}
S_A \cdot S_{C1} + S_A \cdot S_{C2} &= -S^2(3 \sin^2(\theta) - 2) + S \sum_k (a_k^\dagger a_k + c_k^\dagger c_k)(3 \sin^2(\theta) - 2) \\
&\quad - \frac{3S}{2} \sin^2(\theta) \sum_k (a_k^\dagger c_{-k}^\dagger + a_k c_{-k}) \cos k \cdot \delta_1 \\
&\quad - \frac{S}{2} (2 - 3 \sin^2(\theta)) \sum_k (a_k c_k^\dagger + a_k^\dagger c_k) \cos k \cdot \delta_1 \\
&\quad + S\sqrt{3}i \cos(\theta) \sum_k (c_k^\dagger a_k - c_k a_k^\dagger) \cos k \cdot \delta_1
\end{aligned}$$

$$\begin{aligned}
\sum_{j \in B, C} S_A \cdot S_j &= -2S^2(3 \sin^2(\theta) - 2) + S \sum_k (2a_k^\dagger a_k + b_k^\dagger b_k + c_k^\dagger c_k)(3 \sin^2(\theta) - 2) \\
&\quad - \frac{3S}{2} \sin^2(\theta) \sum_k (a_k^\dagger b_{-k}^\dagger + a_k b_{-k}) \cos k \cdot \delta_2 + (a_k^\dagger c_{-k}^\dagger + a_k c_{-k}) \cos k \cdot \delta_1 \\
&\quad - \frac{S}{2} (2 - 3 \sin^2(\theta)) \sum_k (a_k b_k^\dagger + a_k^\dagger b_k) \cos k \cdot \delta_2 + (a_k c_k^\dagger + a_k^\dagger c_k) \cos k \cdot \delta_1 \\
&\quad + S\sqrt{3}i \cos(\theta) \sum_k (a_k^\dagger b_k - a_k b_k^\dagger) \cos k \cdot \delta_2 + (c_k^\dagger a_k - c_k a_k^\dagger) \cos k \cdot \delta_1
\end{aligned}$$

Similarly then we pick Spin B and Spin C within the primitive unit cell and consider all the interactions as we did for Spin A. Then we find,

$$\begin{aligned}
\sum_{j \in A, C} S_B \cdot S_j &= -2S^2(3 \sin^2(\theta) - 2) + S \sum_k (2b_k^\dagger b_k + c_k^\dagger c_k)(+a_k^\dagger a_k)(3 \sin^2(\theta) - 2) \\
&\quad - \frac{3S}{2} \sin^2(\theta) \sum_k (a_k^\dagger b_{-k}^\dagger + a_k b_{-k}) \cos k \cdot \delta_2 + (b_k^\dagger c_{-k}^\dagger + b_k c_{-k}) \cos k \cdot \delta_3 \\
&\quad - \frac{S}{2} (2 - 3 \sin^2(\theta)) \sum_k (a_k b_k^\dagger + a_k^\dagger b_k) \cos k \cdot \delta_2 + (b_k c_k^\dagger + b_k^\dagger c_k) \cos k \cdot \delta_3 \\
&\quad + S\sqrt{3}i \cos(\theta) \sum_k (a_k^\dagger b_k - a_k b_k^\dagger) \cos k \cdot \delta_2 + (b_k^\dagger c_k - b_k c_k^\dagger) \cos k \cdot \delta_1
\end{aligned}$$

$$\begin{aligned}
\sum_{j \in A, B} S_C \cdot S_j &= -2S^2(3 \sin^2(\theta) - 2) + S \sum_k (2c_k^\dagger c_k + a_k^\dagger a_k + b_k^\dagger b_k)(3 \sin^2(\theta) - 2) \\
&\quad - \frac{3S}{2} \sin^2(\theta) \sum_k (a_k^\dagger b_{-k}^\dagger + a_k b_{-k}) \cos k \cdot \delta_2 + (a_k^\dagger c_{-k}^\dagger + a_k c_{-k}) \cos k \cdot \delta_1 \\
&\quad - \frac{S}{2} (2 - 3 \sin^2(\theta)) \sum_k (a_k b_k^\dagger + a_k^\dagger b_k) \cos k \cdot \delta_2 + (a_k c_k^\dagger + a_k^\dagger c_k) \cos k \cdot \delta_1 \\
&\quad + S\sqrt{3}i \cos(\theta) \sum_k (b_k^\dagger c_k - b_k c_k^\dagger) \cos k \cdot \delta_2 + (c_k^\dagger a_k - c_k a_k^\dagger) \cos k \cdot \delta_1
\end{aligned}$$

Now we can add up all three equations above and divide by two for double counting and find H_{kagome} as below

$$H_{kagome} = \sum_{NN(i<j)} J_1 S_i \cdot S_j$$

$$\begin{aligned} \mathcal{H}_{kag} = & -3J_1 S^2 (3 \sin^2(\theta) - 2) + J_1 \frac{S}{2} \sum_k (4(3 \sin^2(\theta) - 2) \delta_{\alpha\beta} + \Lambda_{\alpha\beta}) u_k^{\alpha\dagger} u_k^{\beta} \\ & - \frac{3}{2} \sin^2(\theta) \Lambda'_{\alpha\beta} (u_k^{\alpha\dagger} u_{-k}^{\beta\dagger} + u_k^{\alpha} u_{-k}^{\beta}) \end{aligned}$$

$$\Lambda = \begin{bmatrix} 0 & v \cos q_2 & v^* \cos q_1 \\ v^* \cos q_2 & 0 & v \cos q_3 \\ v \cos q_1 & v^* \cos q_3 & 0 \end{bmatrix} \quad \Lambda' = \begin{bmatrix} 0 & \cos q_2 & \cos q_1 \\ \cos q_2 & 0 & \cos q_3 \\ \cos q_1 & \cos q_3 & 0 \end{bmatrix}$$

$$v = (3 \sin^2(\theta) - 2) + 2\sqrt{3}i \cos(\theta)$$

$$\delta_1 = \left(\frac{1}{4}, \frac{\sqrt{3}}{4}, 0 \right) \quad \delta_2 = \left(\frac{1}{4}, -\frac{\sqrt{3}}{4}, 0 \right) \quad \delta_3 = \left(\frac{1}{2}, 0, 0 \right)$$

$$q_i = k \cdot \delta_i$$

Hamiltonian Perfectly match with the result of Appendix of S.H. Lee's Thesis, with zero canting angle $\theta = 90^\circ$.

We can apply the same procedure for Atom D, with kagome Triangular Interaction J2

Here first we consider the interaction for Atom D. Atoms D interact with two A atoms, two B Atoms and two C atoms.

$$S_D^x S_A^x = \frac{S}{2} (d + d^\dagger)(a + a^\dagger)$$

$$S_D^y S_A^y = -\frac{S}{2} (d^\dagger - d)(a^\dagger - a) \cos \theta$$

$$S_D^z S_A^z = S^2 \cos \theta - S(d^\dagger d + a^\dagger a) \cos \theta$$

$$S_D \cdot S_A = S^2 \cos \theta - S(d^\dagger d + a^\dagger a) \cos \theta + \frac{S}{2} \begin{pmatrix} (da + d^\dagger a^\dagger)(1 - \cos \theta) + \\ (d^\dagger a + da^\dagger)(1 + \cos \theta) \end{pmatrix}$$

Similarly,

$$S_D \cdot S_B = S^2 \cos \theta - S(d^\dagger d + b^\dagger b) \cos \theta - \frac{S}{4} \left(\frac{(db + d^\dagger b^\dagger)(1 - \cos \theta) + (d^\dagger b + db^\dagger)(1 + \cos \theta)}{(d^\dagger b + db^\dagger)(1 + \cos \theta)} \right) \\ + \frac{S\sqrt{3}}{2} i \left((d^\dagger b^\dagger - db)(1 - \cos \theta) + (d^\dagger b - db^\dagger)(1 + \cos \theta) \right)$$

$$S_D \cdot S_C = S^2 \cos \theta - S(d^\dagger d + c^\dagger c) \cos \theta - \frac{S}{4} \left(\frac{(dc + d^\dagger c^\dagger)(1 - \cos \theta) + (d^\dagger c + dc^\dagger)(1 + \cos \theta)}{(d^\dagger c + dc^\dagger)(1 + \cos \theta)} \right) \\ - \frac{S\sqrt{3}}{2} i \left((d^\dagger c^\dagger - dc)(1 - \cos \theta) + (d^\dagger c - dc^\dagger)(1 + \cos \theta) \right)$$

As previous we consider,

$$S_D \cdot S_{A1} + S_D \cdot S_{A2} = 2S^2 \cos \theta - 2S \sum_k (d_k^\dagger d_k + a_k^\dagger a_k) \cos \theta \\ + \frac{S}{2} \sum_k (d_k a_{-k} + d_k^\dagger a_{-k}^\dagger) (1 - \cos \theta) \cos k \cdot \delta_4 \\ + \frac{S}{2} \sum_k (d_k^\dagger a_k + d_k a_k^\dagger) (1 + \cos \theta) \cos k \cdot \delta_4 \\ S_D \cdot S_{B1} + S_D \cdot S_{B2} = 2S^2 \cos \theta - 2S \sum_k (d_k^\dagger d_k + b_k^\dagger b_k) \cos \theta \\ + \frac{S}{4} \sum_k (-1 + \sqrt{3}i) (d_k^\dagger b_{-k}^\dagger) (1 - \cos \theta) \cos k \cdot \delta_5 \\ + \sum_k (-1 - \sqrt{3}i) (d_k b_{-k}) (1 - \cos \theta) \cos k \cdot \delta_5 \\ + \frac{S}{4} \sum_k (-1 + \sqrt{3}i) (d_k^\dagger b_k) (1 + \cos \theta) \cos k \cdot \delta_5 \\ + \sum_k (-1 - \sqrt{3}i) (d_k b_k^\dagger) (1 + \cos \theta) \cos k \cdot \delta_5 \\ S_D \cdot S_{C1} + S_D \cdot S_{C2} = 2S^2 \cos \theta - 2S \sum_k (d_k^\dagger d_k + c_k^\dagger c_k) \cos \theta \\ + \frac{S}{4} \sum_k (-1 + \sqrt{3}i) (d_k^\dagger c_{-k}^\dagger) (1 - \cos \theta) \cos k \cdot \delta_6 \\ + \sum_k (-1 - \sqrt{3}i) (d_k c_{-k}) (1 - \cos \theta) \cos k \cdot \delta_6$$

$$\begin{aligned}
& + \frac{S}{4} \sum_k (-1 + \sqrt{3}i)(d_k^\dagger c_k)(1 + \cos\theta) \cos k \cdot \delta_6 \\
& + \sum_k (-1 - \sqrt{3}i)(d_k c_k^\dagger)(1 + \cos\theta) \cos k \cdot \delta_6
\end{aligned}$$

We need to add up all these three equations and finally we come up with,

$$\begin{aligned}
\mathcal{H}_{\text{Interplane}} = & 6J_2 S^2 \cos\theta + J_2 S \sum_k \left(-2 \cos\theta \Lambda_{1\alpha\beta} + \frac{(1 + \cos\theta)}{4} \Lambda_{2\alpha\beta} \right) u_k^{\alpha\dagger} u_k^\beta \\
& + \frac{1 - \cos\theta}{4} (\Lambda_{3\alpha\beta} u_k^{\alpha\dagger} u_{-k}^\beta + \Lambda_{3\alpha\beta}^* u_k^\alpha u_{-k}^\beta)
\end{aligned}$$

$$\Lambda_1 = \begin{bmatrix} 1 & 0 & 0 & 0 \\ 0 & 1 & 0 & 0 \\ 0 & 0 & 1 & 0 \\ 0 & 0 & 0 & 3 \end{bmatrix} \quad \Lambda_2 = \begin{bmatrix} 0 & 0 & 0 & 2 \cos q_4 \\ 0 & 0 & 0 & u^* \cos q_5 \\ 0 & 0 & 0 & u \cos q_6 \\ 2 \cos q_4 & u \cos q_5 & u^* \cos q_6 & 0 \end{bmatrix}$$

$$\Lambda_3 = \begin{bmatrix} 0 & 0 & 0 & 2 \cos q_4 \\ 0 & 0 & 0 & u \cos q_5 \\ 0 & 0 & 0 & u^* \cos q_6 \\ 2 \cos q_4 & u \cos q_5 & u^* \cos q_6 & 0 \end{bmatrix}$$

$$u = -1 + \sqrt{3}i$$

$$\delta_4 = \left(0, \frac{1}{2\sqrt{3}}, -\frac{1}{6} \right) \quad \delta_5 = \left(-\frac{1}{4}, -\frac{1}{4\sqrt{3}}, -\frac{1}{6} \right) \quad \delta_6 = \left(\frac{1}{4}, -\frac{1}{4\sqrt{3}}, -\frac{1}{6} \right)$$

$$q_i = k \cdot \delta_i$$

After combining $\mathcal{H}_{\text{kagome}} + \mathcal{H}_{\text{Interplane}}$ we have

$$\mathcal{H} = \mathcal{H}_{\text{kagome}} + \mathcal{H}_{\text{Interplane}}$$

$$\mathcal{H} = -3J_1 S^2 (3 \sin^2(\theta) - 2) + 6J_2 S^2 \cos \theta + S \sum_k (\Lambda_{A\alpha\beta} + \Lambda_{B\alpha\beta}) u_k^{\alpha\dagger} u_k^\beta + \frac{1}{2} \Lambda_{C\alpha\beta} u_k^{\alpha\dagger} u_{-k}^{\beta\dagger} + \frac{1}{2} \Lambda_{C\alpha\beta}^* u_k^\alpha u_{-k}^\beta$$

$$\Lambda_A = \frac{1}{2} \begin{bmatrix} (4C1 - C2) & 0 & 0 & 0 \\ 0 & (4C1 - C2) & 0 & 0 \\ 0 & 0 & (4C1 - C2) & 0 \\ 0 & 0 & 0 & -3C2 \end{bmatrix}$$

$$\Lambda_B = \frac{1}{2} \begin{bmatrix} 0 & v \cos(q_2) & v^* \cos(q_1) & 2C3 \cos(q_4) \\ v^* \cos(q_2) & 0 & v \cos(q_3) & C3 u^* \cos(q_5) \\ v \cos(q_1) & v^* \cos(q_3) & 0 & C3 u \cos(q_6) \\ 2C3 \cos(q_4) & C3 u \cos(q_5) & C3 u^* \cos(q_6) & 0 \end{bmatrix}$$

$$\Lambda_C = \begin{bmatrix} 0 & C4 \cos(q_2) & C4 \cos(q_1) & 2C5 \cos(q_4) \\ C4 \cos(q_2) & 0 & C4 \cos(q_3) & C5 u \cos(q_5) \\ C4 \cos(q_1) & C4 \cos(q_3) & 0 & C5 u^* \cos(q_6) \\ 2C5 \cos(q_4) & C5 u \cos(q_5) & C5 u^* \cos(q_6) & 0 \end{bmatrix}$$

$$C1 = J_1(3 \sin^2(\theta) - 2) \quad , \quad C2 = 4J_2 \cos(\theta) \quad , \quad v = J_1((3 \sin^2(\theta) - 2) + 2\sqrt{3}i \cos(\theta))$$

$$C3 = J_2(1 + \cos(\theta)), \quad C4 = -\frac{3}{2}J_1 \sin^2(\theta), \quad C5 = J_2 \frac{1 - \cos(\theta)}{2}, \quad u = -1 + \sqrt{3}i$$

Spin wave Dynamical Matrix

$$H_q(k) = \begin{bmatrix} \Lambda_A + \Lambda_B & -\Lambda_C \\ \Lambda_C^* & -(\Lambda_A + \Lambda_B)^* \end{bmatrix} \quad 8 \times 8 \text{ Matrix}$$

We can diagonalize this Matrix using a computer program and plot the dispersion

Bibliography

- [1] R.Moessner and A. P.Ramirez. *Phys. Today*, 59:24, 2006.
- [2] B. G.Levi. *Phys. Today*, 60:16, 2007.
- [3] P. W.Anderson. *Mater. Res. Bull.*, 8:153, 1973.
- [4] RobertJ. Cava, KatharineL. Holman, Tyrel McQueen, EricJ. Welsh, D.Vincent West, and AnthonyJ. Williams. The geometries of triangular magnetic lattices. In Claudine Lacroix, Philippe Mendels, and Frédéric Mila, editors, *Introduction to Frustrated Magnetism*, volume 164 of *Springer Series in Solid-State Sciences*, pages 131–154. Springer Berlin Heidelberg, 2011. ISBN 978-3-642-10588-3. doi: 10.1007/978-3-642-10589-0_6. URL http://dx.doi.org/10.1007/978-3-642-10589-0_6.
- [5] J. S. Helton et al. *Phys. Rev. Lett.*, 98:107204, 2007.
- [6] P. Mendels et al. *Phys. Rev. Lett.*, 98:077204, 2007.
- [7] Y. Qiu B. Lake Q. Huang K. Habicht S.-H. Lee, H. Kikuchi and K. Kiefer. *Nature Mater.*, 6:853, 2007.
- [8] A.P. Ramirez. *Annu. Rev. Mater. Sci.*, 24:453, 1994.
- [9] C. Tassel, J. Kang, C. Lee, O. Hernandez, Y. Qiu, W. Paulus, E. Collet, B. Lake, T. Guidi, M.-H. Whangbo, C. Ritter, H. Kageyama, and S.-H. Lee. *Phys. Rev. Lett.*, 105:167205, 2010.
- [10] W. Tian et al. *Physica B*, 385386:5052, 2006.
- [11] The susceptibility as a function of temperature. URL <http://en.wikipedia.org/wiki/File:Susceptibility.png>.
- [12] D.N.H. Nam P. Nordblad R. Mathieu, P. Jönsson. *arXiv:cond-mat/0007070*, 2000.
- [13] Shapes of atomic orbitals. URL http://en.wikibooks.org/wiki/High_School_Chemistry/Shapes_of_Atomic_Orbitals.

- [14] Crystal field theory (cft), an introduction. URL <http://wwwchem.uwimona.edu.jm/courses/CFT.html>.
- [15] H.A. Jahn and E. Teller. *Proc. R. Soc. London A*, 161:220–235, 1937.
- [16] T. Suzuki, M. Katsumura, K. Taniguchi, T. Arima, and T. Katsufuji. *Phys. Rev. Lett.*, 98:127203, 2007.
- [17] The jahn-teller theorem. URL <http://wwwchem.uwimona.edu.jm/courses/JahnTeller.html>.
- [18] J. N. Lalena and D. A. Cleary. *Principles of Inorganic Materials Design*, 2nd ed. John Wiley & Sons, New York.
- [19] Clarence Zener. *Phys. Rev.*, 82:403–405, 1951.
- [20] N. P. Raju, J. E. Greedan, and M. A. Subramanian. *Phys. Rev. B*, 49:1086–1091, 1994.
- [21] Double-exchange mechanism. URL http://en.wikipedia.org/wiki/Double-exchange_mechanism.
- [22] Gen Shirane, Stephen M. Shapiro, and John M. Tranquada. *Neutron Scattering with a Triple-Axis Spectrometer*. Cambridge University Press, 2002. ISBN 9780511534881. URL <http://dx.doi.org/10.1017/CB09780511534881>. Cambridge Books Online.
- [23] High resolution powder diffractometer - bt1. URL <http://www.ncnr.nist.gov/instruments/bt1/>.
- [24] Polarized triple-axis spectrometer. URL <https://neutrons.ornl.gov/ptax>.
- [25] The ncnr disk chopper spectrometer (dcs). URL <http://www.ncnr.nist.gov/instruments/dcs/>.
- [26] Scattering cross-section. URL http://en.wikipedia.org/wiki/Scattering_cross-section.
- [27] G. L. Squires. *Introduction to the theory of thermal neutron scattering*. Dover publications, 1996.
- [28] E. F. Bertaut. *J. Appl. Phys.*, 33:1138, 1962.
- [29] E. F. Bertaut. *Acta. Cryst. A*, 24:217, 1968.
- [30] E. F. Bertaut. *J. de Physique Colloque*, C1:462, 1971.
- [31] E. F. Bertaut. *J. Magn. Magn. Mat.*, 24:267, 1981.

- [32] V. E. Naish Yu. A. Izyumov and R. P. Ozerov. *Neutron Diffraction of Magnetic Materials*. Consultants Bureau, New York, 1991.
- [33] C.J. Bradley and A.P. Cracknell. *The Mathematical Theory of Symmetry in Solids*.
- [34] A.P. Cracknell. *Magnetism in Crystalline Materials*. Pergamon Press, Oxford), 1975.
- [35] A.S Wills. A new protocol for the determination of magnetic structures using simulated annealing and representational analysis (sarah). *Physica B: Condensed Matter*, 276278(0):680 – 681, 2000.
- [36] O. V. Kovalev. *Representations of the Crystallographic Space Groups, Edition 2*. Gordon and Breach Science Publishers, Switzerland, 1993.
- [37] Charles Kittel. *Quantum Theory of Solids*. Wiley; 2nd Revised Edition edition, 1987.
- [38] S. E. Dissanayake, C. Chan, S. Ji, J. Lee, Y. Qiu, K. C. Rule, B. Lake, M. Green, M. Hagihala, X. G. Zheng, T. K. Ng, and S.-H. Lee. *Phys. Rev. B*, 85:174435, May 2012.
- [39] B. Lake S. Toth. *arXiv:1402.6069*, 2014.
- [40] H Fukuyama H Seo. *J. Phys. Soc. Japan*, 67:2602, 1998.
- [41] M Isobe Y Ueda T Ohama, H Yasuoka. *Phys. Rev. B*, 59:3299, 1999.
- [42] D.I Khomskii M.V Mostovoy. *Solid State Commun.*, 113:159, 1999.
- [43] D.B McWhan S Kachi M Marezio, P.D Dernier. *J. Solid State Chem.*, 11:301, 1974.
- [44] M Marezio J.-L Hodeau. *J. Solid State Chem.*, 23:253, 1978.
- [45] Y Morii E Akiba S Funahashi K Kato M Isobe E Takayama-Muromachi Y Uchida Y Kanke, F Izumi. *J. Solid State Chem.*, 112:429, 1994.
- [46] R Matsuo Y Kanke T Haeiwa E Kita A Akiba, H Yamada. *J. Phys. Soc. Japan*, 67:1303, 1998.
- [47] E Takayama-Muromachi K Kato Y Uchida, Y Kanke. *J. Phys. Soc. Japan*, 60:2530, 1991.
- [48] J.E Greedan C.A Bridges. *Journal of Solid State Chemistry*, 177(45):10981110, 2004.
- [49] Craig A. Bridges, T. Hansen, A. S. Wills, G. M. Luke, and J. E. Greedan. *Phys. Rev. B*, 74:024426, 2006.

- [50] T. Kajita, T. Kanzaki, T. Suzuki, J. E. Kim, K. Kato, M. Takata, and T. Katsufuji. *Phys. Rev. B*, 81:060405, 2010.
- [51] T. Kanzaki, R. Kubota, and T. Katsufuji. *Phys. Rev. B*, 85:144410, 2012.
- [52] Yasuhiro Shimizu, Keniichiro Matsudaira, Masayuki Itoh, Tomomasa Kajita, and Takuro Katsufuji. *Phys. Rev. B*, 84:064421, 2011.
- [53] K. Takubo, T. Kanzaki, Y. Yamasaki, H. Nakao, Y. Murakami, T. Oguchi, and T. Katsufuji. *Phys. Rev. B*, 86:085141, 2012.
- [54] D. B. McWhan, T. M. Rice, and J. P. Remeika. *Phys. Rev. Lett.*, 23:1384–1387, 1969.
- [55] D. B. McWhan and J. P. Remeika. *Phys. Rev. B*, 2:3734–3750, 1970.
- [56] D. B. McWhan, A. Menth, J. P. Remeika, W. F. Brinkman, and T. M. Rice. *Phys. Rev. B*, 7:1920–1931, 1973.
- [57] Guo Liu and J.E. Greedan. *Journal of Solid State Chemistry*, 122(2):416 – 427, 1996.
- [58] Juan Rodríguez-Carvajal. Recent advances in magnetic structure determination by neutron powder diffraction. *Physica B: Condensed Matter*, 192(12):55 – 69, 1993.
- [59] S. W. Lovesey. *Theory of Thermal Neutron Scattering from Condensed Matter*.
- [60] Y. Qiu, C. Broholm, S. Ishiwata, M. Azuma, M. Takano, R. Bewley, and W. J. L. Buyers. *Phys. Rev. B*, 71:214439, 2005.
- [61] John B. Goodenough. *Phys. Rev.* 117, 1442, 1960.
- [62] Seung-Hun Lee, Hidenori Takagi, Despina Louca, Masaaki Matsuda, Sungdae Ji, Hiroaki Ueda, Yutaka Ueda, Takuro Katsufuji, Jae-Ho Chung, Sungil Park, Sang-Wook Cheong, and Collin Broholm. *J. Phys. Soc. Jpn., Vol. 79, No. 1*, 2010.
- [63] Yutaka Ueda, Naoki Fujiwara, and Hiroshi Yasuoka. *J. Phys. Soc. Jpn.*, 66:778–783, 1997.
- [64] S.-H. Lee et al. *Phys. Rev. Lett.*, 93:156407, 2004.
- [65] Z. Zhang et al. *Phys. Rev. B*, 74:014108, 2006.
- [66] H. D. Zhou, J. Lu, and C. R. Wiebe. *Phys. Rev. B*, 76:174403, 2007.
- [67] J. H. Chung, J. H. Kim, S. H. Lee, T. J. Sato, T. Suzuki, M. Katsumura, and T. Katsufuji. *Phys. Rev. B*, 77:054412, 2008.

- [68] V. O. Garlea, R. Jin, D. Mandrus, B. Roessli, Q. Huang, M. Miller, A. J. Schultz, and S. E. Nagler. *Phys. Rev. Lett.*, 100:066404, 2008.
- [69] Vincent Hardy, Yohann Bréard, and Christine Martin. *Phys. Rev. B*, 78:024406, 2008.
- [70] S.-H. Baek, N. J. Curro, K.-Y. Choi, A. P. Reyes, P. L. Kuhns, H. D. Zhou, and C. R. Wiebe. *Phys. Rev. B*, 80:140406, 2009.
- [71] S. Sarkar, T. Maitra, R. Valentí, and T. Saha-Dasgupta. *Phys. Rev. Lett.*, 102:216405, 2009.
- [72] G-W. Chern, N. Perkins, and Z. Hao. *Phys. Rev. B*, 81:125127, 2010.
- [73] Y. Nii, N. Abe, and T. Arima. *Phys. Rev. B*, 87:085111, 2013.
- [74] S. L. Gleason, T. Byrum, Y. Gim, A. Thaler, P. Abbamonte, G. J. MacDougall, L. W. Martin, H. D. Zhou, and S. L. Cooper. *Phys. Rev. B*, 89:134402, 2014.
- [75] T. Katsufuji, T. Suzuki, H. Takei, M. Shingu, K. Kato, K. Osaka, M. Takata, H. Sagayama, and T. Arima. *J. Phys. Soc. Jpn.*, 77:053708, 2008.
- [76] Soumyajit Sarkar and T. Saha-Dasgupta. *Phys. Rev. B*, 84:235112, 2011.
- [77] G. J. MacDougall, V. O. Garlea, A. A. Aczel, H. D. Zhou, and S. E. Nagler. *Phys. Rev. B*, 86:060414, 2012.
- [78] Q. Zhang, K. Singh, F. Guillou, C. Simon, Y. Breard, V. Caignaert, and V. Hardy. *Phys. Rev. B*, 85:054405, 2012.
- [79] Y. Nii, H. Sagayama, T. Arima, S. Aoyagi, R. Sakai, S. Maki, E. Nishibori, H. Sawa, K. Sugimoto, H. Ohsumi, and M. Takata. *Phys. Rev. B*, 86:125142, 2012.
- [80] J.-S. Kang, Jihoon Hwang, D. H. Kim, Eunsook Lee, W. C. Kim, C. S. Kim, Sangil Kwon, Soonchil Lee, J.-Y. Kim, T. Ueno, M. Sawada, Bongjae Kim, Beom Hyun Kim, and B. I. Min. *Phys. Rev. B*, 85:165136, 2012.
- [81] S. Kawaguchi, H. Ishibashi, S. Nishihara, M. Miyagawa, K. Inoue, S. Mori, and Y. Kubota. *J. Phys.: Condens. Matter*, 25:416005, 2013.
- [82] Z. H. Huang, X. Luo, L. Hu, S. G. Tan, Y. Liu, B. Yuan, J. Chen, W. H. Song, and Y. P. Sun. *J. Appl. Phys.*, 115:034903, 2014.
- [83] D. Choudhury, T. Suzuki, D. Okuyama, D. Morikawa, K. Kato, M. Takata, K. Kobayashi, R. Kumai, H. Nakao, Y. Murakami, M. Bremholm, B. B. Iversen, T. Arima, Y. Tokura, and Y. Taguchi. *Phys. Rev. B*, 89:104427, 2014.

- [84] A. Kismarahardja, J. S. Brooks, A. Kiswandhi, K. Matsubayashi, R. Yamanaka, Y. Uwatoko, J. Whalen, T. Siegrist, and H. D. Zhou. *Phys. Rev. Lett.*, 106:056602, 2011.
- [85] A. Kiswandhi, J. S. Brooks, J. Lu, J. Whalen, T. Siegrist, and H. D. Zhou. *Phys. Rev. B*, 84:205138, 2011.
- [86] Y. Huang, Z. Yang, and Y. Zhang. *J. Phys., Condens. Matter*, 24:056003, 2012.
- [87] Ramandeep Kaur, Tulika Maitra, and Tashi Nautiyal. *J. Phys.: Condens. Matter*, 26:045505, 2014.
- [88] A. Kismarahardja, J. S. Brooks, H. D. Zhou, E. S. Choi, K. Matsubayashi, , and Y. Uwatoko. *Phys. Rev. B*, 87:054432, 2013.
- [89] J. Ma, J. H. Lee, S. E. Hahn, Tao Hong, H. B. Cao, A. A. Aczel, Z. L. Dun, M. B. Stone, W. Tian, Y. Qiu, J. R. D. Copley, H. D. Zhou, R. S. Fishman, and M. Matsuda. *Phys. Rev. B*, 91:020407, 2015.
- [90] Rogers D B, Arnott R J, Wold A, and Goodenough J B. *J. Phys. Chem. Solids* 24 347, 1963.
- [91] Menyuk N, Wold A, Rogers D, and Dwight K. *J. Appl. Phys.* 33 1144, 1962.
- [92] Dwight K, Menyuk N, Rogers D B, and Wold A. *Proc. Int. Conf. on Magnetism 1964 (Nottingham,)* p 538, 1965.
- [93] J.B. Goodenough edited by H. Reiss. *Progress in Solid State Chemistry*, chapter Metallic Oxides. Pergamon, New York, 1972.
- [94] R. Koborinai, S.E. Dissanayake, M. Reehuis, M. Matsuda, S. H. Lee, and T. Katsufuji. (*Submitted*), 2015.
- [95] In neutron scattering of a real crystal, which can be regarded as a bunch of many crystal blocks with *nearly* the same orientation, an incident neutron beam is reflected from many crystal blocks if there is small misorientation between the blocks. However, if the orientation of the crystal blocks are perfect, an upstream crystal block depletes the beam before it reaches a downstream crystal block that has exactly the same orientation and is supposed to reflect the same beam as the upstream crystal. This effect (extinction effect) reduces the scattering intensity of the beam.